Double Nanohole Aperture Optical Tweezers: Towards Single Molecule Studies

by

Ahmed Al Balushi
B.Eng., University of Bath, 2005
M.Sc., University of Bath, 2007

A Dissertation Submitted in Partial Fulfillment of the
Requirements for the Degree of

DOCTOR OF PHILOSOPHY

in the Department of Electrical and Computer Engineering

Double Nanohole Aperture Optical Tweezers:

Towards Single Molecule Studies

by

Ahmed Al Balushi

B.Eng., University of Bath, 2005

M.Sc., University of Bath, 2007

Supervisory Committee

Dr. Reuven Gordon, Supervisor

(Department of Electrical and Computer Engineering)

Dr. Poman So, Departmental Member

(Department of Electrical and Computer Engineering)

Dr. Stephanie Willerth, Outside Member

(Department of Mechanical Engineering)

Supervisory Committee

Dr. Reuven Gordon, Supervisor

(Department of Electrical and Computer Engineering)

Dr. Poman So, Departmental Member

(Department of Electrical and Computer Engineering)

Dr. Stephanie Willerth, Outside Member

(Department of Mechanical Engineering)

ABSTRACT

Nanoaperture optical tweezers are emerging as useful tools for the detection and identification of biological molecules and their interactions at the single molecule level. Nanoaperture optical tweezers provide a low-cost, scalable, straight-forward, high-speed platform for single molecule studies without the need to use tethers or labeling. This thesis gives a general description of conventional optical tweezers and how they are limited in terms of their capability to trapping biological molecules. It also looks at nanoaperture-based optical tweezers which have been suggested to overcome the limitations of conventional optical tweezers. The thesis then focuses on the double nanohole optical tweezer as a tool for trapping biological molecules and studying their behaviour and interactions with other molecules. The double

nanohole aperture trap integrated with microfluidic channels has been used to detect single protein binding. In that experiment a double-syringe pump was used to deliver biotin-coated polystyrene particles to the double nanohole trapping site. Once stable trapping of biotin-coated polystyrene particle was achieved, the double-syringe pump was used to flow in streptavidin solution to the trapping site and binding was detected by measuring the transmission through the double nanohole aperture. In addition, the double nanohole optical tweezer has been used to observe the real-time dynamic variations in protein-small molecule interaction (PSMI) with the primary focus on the effect of single and multiple binding events on the dynamics of the protein in the trap. Time traces of the bare form of the streptavidin showed slower timescale dynamics as compared to the biotinylated forms of the protein. Furthermore, the double nanohole aperture tweezer has been used to study the real-time binding kinetics of PSMIs and to determine their disassociation constants. The interaction of blood protein human serum albumin (HSA) with tolbutamide and phenytoin was considered in that study. The dissociation constants of the interaction of HSA with tolbutamide and phenytoin obtained using our technique were in good agreement with the values reported in the literature. These results would open up new windows for studying real-time binding kinetics of protein-small molecule interactions in a label-free, free-solution environment, which will be of interest to future studies including drug discovery.

Contents

List of Tables

List of Figures

ACKNOWLEDGEMENTS

First and foremost, I am deeply grateful to my supervisor Prof. Reuven Gordon for his endless support, valuable guidance and critical advice. I also would like to thank my dissertation committee members Dr. Poman So and Dr. Stephanie Willerth as well as the external examinar Dr. Jer-Shing Huang for providing valuable comments and advice for improving my thesis.

In addition, I thank Prof. A Alexandre G. Brolo, Dr. Rustom Bhiladvala and Dr. Stephanie Willerth and their respective students for giving me access to their labs and for helping me in their areas of expertise. My thanks also go to Dr. Elaine Humphrey and Adam Schuetze for all their help and guidance in the area of nanofabrication and imagine. I also express my deep gratitude to my colleagues in the Nanoplasmonics Research Lab for all their support and for the insightful scientific discussions.

Last but not least, I am very fortunate to have a wonderful family whose endless support was my main driving force throughout my PhD journey. No words can express how much I am indebted to them.

DEDICATION

To my family

Chapter 1

Introduction

1.1 Optical Tweezers: at a Glance

Optical tweezers provide a gentle way of controlling and manipulating small particles using light. Since the first demonstration of single beam optical trap [1], optical tweezers have been used to isolate and manipulate dielectric particles [2, 3], carbon nanotubes [4–8], graphene flakes [9, 10], nanodiamonds [11], semiconductor nanowires [12–19] and metal nanoparticles [20–30] . This has opened up new possibilities for studying nanometer-size biological particles and their interactions; for example, studying interactions including those of protein protein, protein small molecule, protein DNA and protein antibody.

In order to achieve stable trapping of a single nanometer-sized molecule using conventional optical tweezers, two challenges have to be overcome. First, for trapping particles much smaller than the wavelength of light, the optical power required typically scales with the inverse third power of the particle size. Second, as the particle size decreases the viscous drag is decreased, making escape from the trap faster. Therefore, for trapping smaller particles high laser powers are needed - an option

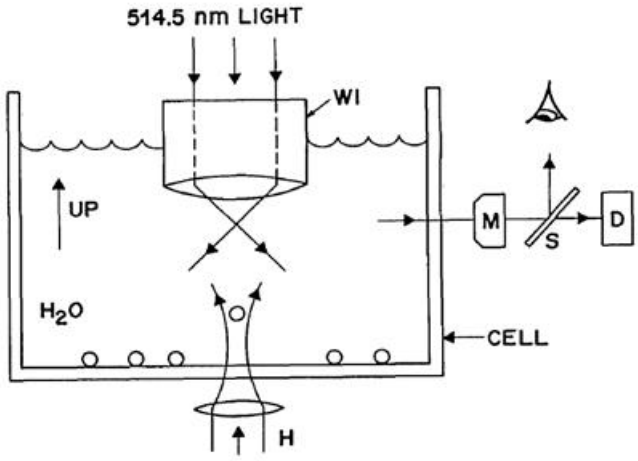

Figure 1.1: Sketch of the first basic apparatus used for the optical trapping of dielectric particles in water by means of a single beam gradient force trap. Abbreviations used: M = microscope; S = beam splitter; D = detector; WI = water immersion microscope objective; H = holding beam. Reprinted from Ref. [1], Copyright 1986, OSA.

which is not always available, especially when working with temperature-sensitive biological molecules.

One approach for trapping small biological particles with moderate laser powers is to use nanoapertures in metal films. A number of nanoaperture geometries have been suggested, for example, rectangular, bowtie and circular. One interesting geometry is the double nanohole aperture where the narrow gap between the two cusps of the aperture leads to a high local field enhancement which results in a strong trapping point.

The double nanohole tweezer system has been used to trap single nanoparticles, including proteins [31] and DNAs [32]. In addition, it has been demonstrated that the double nanohole aperture is capable of sensing the size, concentration and the refractive index of trapped particles [33]. Furthermore, the double nanohole aperture has been used to probe the vibrational modes of nanoparticles [34].

This thesis looks at different ways that the double nanohole tweezer system can be used for, not only to trap single molecules but also to gain information about

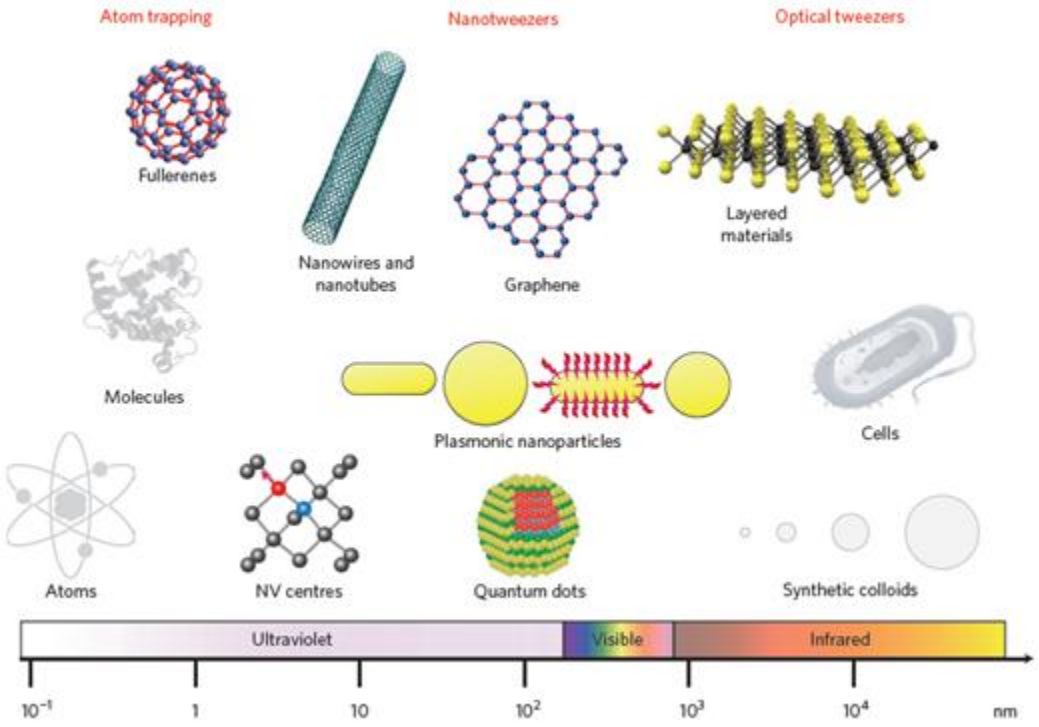

Figure 1.2: Different objects of different sizes can be trapped. The horizontal scale bar shows the average object size and the corresponding light wavelength. NV, nitrogen vacancy. Reprinted from Ref. [35], Copyright 2013, Nature Publishing Group.

their behavior and study their interactions with other molecules. Towards achieving this goal, the thesis shows how the double nanohole optical trap, integrated with microfluidic channels, has been used to detect protein binding at the single molecule level. Thesis also will show how the double nanohole optical tweezer was also used to distinguish between the bare and bound forms of proteins. In addition, it will be shown how the double nanohole tweezer might be used for finding the binding constants of proteins in a label-free, free-solution environment.

1.2 Thesis Outline

This thesis aims at developing techniques that can be used with the double nanohole aperture optical trapping system to gain information about trapped molecules and

possibly study their interactions with other molecules. In terms of structure, this thesis follows the manuscript style where each chapter is based on one or more peer-reviewed papers published in scientific journals. Generally, chapters 2 and 3 focus on the optical trapping aspects of the thesis while chapter 4 details the statistical and analysis methods that have been applied to study trapped molecules. Below is a brief summary of each chapters content.

The remaining part of Chapter 1 gives a list of the papers that have been published during the course of the PhD period.

Chapter 2 gives a general introduction to single beam gradient force optical tweezers and discusses the limitations of this type of conventional tweezers and how they can be overcome by using nanoapertures. It also introduces the self-induced back-action principle and explains how it was used to stably trap nanoparticles with relatively low powers.

Chapter 3 presents the working principle of the double nanohole optical tweezer system. It also shows how the double nanohole optical trap can be used to identify single nanoparticles once trapped.

Chapter 4 is the main part of the thesis as it contains a summary of the published scientific papers. The first section of the chapter shows how microfluidic channels can be integrated with the double nanohole optical trap to detect single protein binding. The second section describes how the double nanohole optical trap can be used to observe the real-time dynamics of PSMIs. The third section describes how the double nanohole optical tweezer can be used to study the real-time binding kinetics of PSMIs and determine their disassociation constants.

Chapter 5 concludes the thesis and suggests some future work.

In the Appendix, peer-review papers that have been published in scientific journals during the PhD period are reproduced.

1.3 Author's Contributions

This thesis follows the publication based article-style format; each chapter is based on one or more peer-reviewed published scientific journal papers. The contribution of the authors is given below:

1. **A. A. Al Balushi** , A. Zehtabi-Oskuie, R. Gordon, Observing single protein binding by optical transmission through a double nanohole aperture in a metal film, Biomed. Opt. Exp. 4(9), 15041511 (2013).

   A. A. Al Balushi performed the microfluidic integration and carried out the experiment. The double nanohole structure was fabricated by A. Zehtabi-Oskuie. The experiments were conceived and designed by A. A. Al Balushi and R. Gordon. A. A. Al Balushi and R. Gordon co-wrote the manuscript.

2. **A. A. Al Balushi**, and Reuven Gordon, Label-free free solution single-molecule protein-small molecule interaction observed by double nanohole plasmonic trapping, ACS Photonics 1(5), 389 393 (2014).

   A. A. Al Balushi fabricated the double nanohole aperture and performed the experiments. The experiments were conceived and designed by A. A. Al Balushi and R. Gordon. A. A. Al Balushi and R. Gordon co-wrote the manuscript.

3. **A. A. Al Balushi**, and Reuven Gordon, A label-free untethered approach to single-molecule protein binding kinetics, Nanoletters 14(10), 5787 5791 (2014).

   A. A. Al Balushi fabricated the double nanohole aperture and performed the experiment. The experiments were conceived and designed by A. A. Al Balushi and R. Gordon. A. A. Al Balushi and R. Gordon co-wrote the manuscript.

4. S. Jones, **A. A. Al Balushi**, R. Gordon, Raman spectroscopy of single nanoparticles in a double nanohole optical tweezer system, Journal of Optics 17(10),

102001 (2015).

A. A. Al Balushi fabricated the double nanohole aperture and obtained the Raman spectra for bulk polystyrene and titania solution. S. Jones performed the rest of the experiments. The experiments were conceived and designed by S. Jones and R. Gordon.

5. R. Rejmi, **A. A. Al Balushi**, H. Rigneault, R. Gordon and J. Wenger, Nanoscale volume confinement and flurescence enhancement with double nanohole aperture, Scientific Reports (5),15852 (2015).

   A. A. Al Balushi obtained the finite-difference time-domain (FDTD) simulation results for the transmission spectra through the double nanohole aperture. In addition, A. A. Al Balushi preformed the double nanohole LDOS enhancement simulation. The experiments were conceived by R. Rejmi, H. Rigneault, R. Gordon and J. Wenger. R. Rejmi performed the experiments.

6. A. Zehtabi-Oskuie, H. Jiang, B. R. Cyr, D. W. Rennehan, **A. A. Al Balushi**, R. Gordon, Double nanohole optical trapping: dynamics and protein-antibody co-trapping, Lab Chip 13, 2563-2568 (2013).

   A. A. Al Balushi, B. Cyr and D. Rennehan preformed the data analysis for Kramers hopping and skewness distribution. H. Jiang preformed the FDTD simulation of the double nanohole trap. The experiments were conceived and designed by A. Zehtabi-Oskuie and R. Gordon.

In addition, results obtained during the course of the PhD period has led to the publication of the following conference papers:

7. **A. A. Al Balushi**, and Reuven Gordon, Label-Free Free Solution Single Protein-Small Molecule Binding Kinetics: An Optical Tweezer Approach, In

Optical Trapping Applications, pp. OtT2E-3. Optical Society of America, 2015.

8. **A. A. Al Balushi**, and Reuven Gordon, Real-Time Dynamics of Single Protein-Small Molecule Interactions with Label-Free, Free-Solution Double-Nanohole Optical Trapping, In Frontiers in Optics, pp. FTh1E-7. Optical Society of America, 2014.

9. R. Gordon, S. Wheaton, R. F. Gelfand, T. S. DeWolf, **A. A. Al Balushi**, and A. Kotnala, Probing the Vibrations of Individual Non-Resonant Nanoparticles by Nanoaperture Optical Tweezers, In European Quantum Electronics Conference, p. EG-7-1. Optical Society of America, 2015.

10. A. Kotnala, **A. A. Al Balushi**, R. Gordon, Optical tweezers for free-solution label-free single bio-molecule studies, Proc. SPIE 9164, Optical Trapping and Optical Micromanipulation XI, 916418 (September 16, 2014); doi:10.1117/12.2062051.

11. R. Gordon, **A. A. Al Balushi**, A. Kotnala, R.F. Gelfand, S. Wheaton, S. Chen, S. Jin, New physics and applications of apertures in thin metal films, Proc. SPIE 9172, Nanostructured Thin Films VII, 91720A (August 27, 2014); doi:10.1117/12.2062919.

12. S. Wheaton, A. Kotnala, **A. A. Al Balushi**, R.M. Gelfand, A. Zehtabi-Oskuie, Y. Rajashekara, R. Gordon, Trapping, unfolding, identifying, and binding single proteins using the double-nanohole optical trap, Proc. SPIE 9126, Nanophotonics V, 91260O (May 2, 2014); doi:10.1117/12.2049045.

Furthermore, during the PhD period an invited review paper on using nanoapertures for sensing applications was published:

13. **A. A. Al Balushi**, A. Kotnala, S. Wheaton, R. M. Gelfand, Y. Rajashekara, R. Gordon, Label-free free-solution nanoaperture optical tweezers for single molecule protein studies, Analyst 140, 4760 - 4778 (2015).

Chapter 2

Nanoapertures and Optical Trapping[1]

This chapter gives a general description of the single beam gradient force optical tweezers and discusses their limitation. The chapter also looks at aperture based optical traps as an alternative trapping system to overcome the limitations of conventional gradient force optical tweezers. Then self-induced back-action trapping system is introduced showing how the target particles plays an active dynamic rode in this type of trapping mechanism. Towards the end of the chapter, a number of nanoaperture trapping geometries are introduced.

[1]The following chapter is adapted from: A. A. Al Balushi, A. Kotnala, S. Wheaton, R. M. Gelfand, Y. Rajashekara, R. Gordon, Label-free free-solution nanoaperture optical tweezers for single molecule protein studies, Analyst 140, 4760 - 4778 (2015) (Invited Review Paper).

2.1 Single Beam Optical Tweezers and their Limitations

Conventional single beam optical tweezers are mathematically described using the gradient force formulation when trapping particles in the Rayleigh regime (diameter d $\ll \lambda$ wavelength) [1]. In this regime, a particle can be considered as a point dipole that interacts with the incoming light and the dipole moment of the particle is given by

$$\vec{p_e} = \left(\frac{n_p^2 - n_m^2}{n_p^2 + 2n_m^2}\right) n_m^2 \left(\frac{d}{2}\right)^3 \vec{E_0} = \alpha \vec{E_0} \tag{2.1}$$

where, $\vec{E_0}$ is the electric field amplitude of the light shining on a sphere of diameter d and refractive index n_p in a medium of refractive index of n_m, and α is the polarizability of the particle. Therefore, the optical power P_{scat} scattered by the particle can be approximated by the radiation of an electric dipole as [36]

$$P_{scat} = \frac{4}{3} \frac{c^2 Z_0 \pi^3}{\lambda} |\vec{p_e}|^2 \tag{2.2}$$

where Z_0 is the free space impedance, λ is the the wavelength of the laser and c is the speed of light in free-space.

In terms of the optical forces acting on a particle in the Rayleigh regime, two types of forces can be considered: the scattering force and the gradient force. The scattering force is the force exerted on an object in the propagation direction of the laser beam and can be expressed as [1]

$$F_{scat} = \frac{I_0}{c} \frac{128\pi^2 (\frac{d}{2})^6}{3\lambda^4} \left(\frac{n_p^2 - n_m^2}{n_p^2 + 2n_m^2}\right)^2 n_m \tag{2.3}$$

where, I_0 is the light intensity at the particle. The scattering force originates from

the momentum transferred from the photons of the incident light to the particle and is directly related to the power scattered by the particle, Eq. 2.2. The second type of optical force is the gradient force, which is the force due to the gradient of the electric field intensity $|\mathrm{E}|^2$ and is given by [37, 38]

$$F_{grad} = n_m \alpha \nabla \left(\vec{E}.\vec{E}\right) = \frac{1}{2} n_m \alpha \nabla |E|^2 = \frac{n_m^3 \left(\frac{d}{2}\right)^3}{2} \left(\frac{n_p^2 - n_m^2}{n_p^2 + 2n_m^2}\right)^2 \nabla |E|^2. \tag{2.4}$$

This gradient force is derived from the differential force acting on an electric dipole in an electric field gradient. It is clear that as the particle gets smaller, the ratio between the gradient force and the scattering force is proportional to the inverse third power of the particle size, which means that the scattering force can be neglected for particles well into the Rayleigh regime. Furthermore, Eq. 2.4 shows that the gradient force scales with the third power of the particle size. Therefore, to trap smaller particles with this force requires an increase in the field intensity or working with highly polarizable objects. Indeed, 10 nm Au spheres were trapped with high power (400 mW) using a single laser beam [39]. In addition, stable trapping of the tobacco mosaic virus was demonstrated using a single beam optical trap due the high polarizability of that particular virus [40]. However, conditions like high power and/or high polarizability are not available for general dielectric particles, like biological molecules (biomolecules), which are also very temperature sensitive. Therefore, new strategies need to be developed for trapping biological molecules.

The limitation of conventional optical tweezers can also be viewed by looking at the potential of the optical trap U. The trap potential U can be formulated based on the perturbative approximation, where the particle is treated as a point dipole, Eq. 2.1. Hence, the overall trapping potential can be written as [41]

$$U = -\frac{2\pi n_m \left(\frac{d}{2}\right)^3}{c}\left(\frac{n_p^2 - n_m^2}{n_p^2 + 2n_m^2}\right) I \tag{2.5}$$

where the intensity I at the trapping point is given by $I = 0.5\varepsilon_0 c E^2$. It is clear from Eq. 2.5 that the trapping potential is proportional to the third power of the particle diameter, d^3, and to the laser intensity at the trapping point I. It should be mentioned here that the particle in the trap experiences a force due to its Brownian motion. The average thermal kinetic energy of the particle in the trap is $k_B T$, where k_B is the Boltzmanns constant and T is the temperature. However, the instantaneous velocity of the particle follows a Maxwell–Boltzmann distribution [42] in which the energy of the particle can exceed the average kinetic energy. Therefore, in order to account for these high energy events and achieve stable trapping of a Rayleigh particle, the potential well of the optical trap has to overcome the high energy events of the particle. Typical potential depths of around 10 $k_B T$ are required to achieve stable trapping of a Rayleigh particle [1]. For a 20 nm polystyrene particle in water with a laser intensity of about 1.7 MW/m^2 the trapping potential U is found to be about 0.005 $k_B T$. This clearly demonstrates the inherit limitation of conventional gradient–force optical tweezers.

2.2 Nanoaperture-based Optical Tweezers

In order to overcome the limitations of conventional optical tweezers, a number of nanophotonic and plasmonic optical trapping techniques have been suggested [43–51], but these are usually perturbative and require high field intensities or highly polarizable particles to achieve stable trapping of particles less than 100 nm in size. Trapping using nanoapertures in metal films can be used to overcome the problem of required high beam intensities for <100 nm particles and they also allow for easy detection

of trapping events by noting the abrupt increase in the transmission. Bethe's theory approximates the light transmission through a circular aperture (r $\ll \lambda$) in an infinite perfect electric conductor (PEC) by the emission of a magnetic dipole, which can be expressed as

$$T = \frac{1}{2}\frac{4Z_0\pi^3}{3\lambda_0^4}(\frac{8r^3}{3})^2 \propto \frac{r^6}{\lambda^4} \tag{2.6}$$

where Z_0 is the free space impedance, λ_0 is the wavelength in free space, r is the aperture radius and H_0 is the magnetic field of the incident plane wave, as shown in Fig. 2.1(a). It can be shown after normalizing to the area of the circular aperture that the optical transmission through a subwavelength circular aperture is inversely proportional to the fourth power of the incident beam wavelength, i.e. $T \propto (r/\lambda)^4$. Simplistically, if a dielectric object with a refractive index n_p surrounds the aperture then the wavelength in the medium is scaled as $\lambda \propto (\frac{\lambda_0}{n_p})$, hence an increase in the transmission by a factor of n_p^4 is obtained for the same aperture [52, 53], as shown in Fig. 2.1(b).

In addition to the scattering and gradient forces acting upon particles in the Raleigh regime, a number of studies have reported on the effect of thermally induced forces, on the trapped particle [54–59]. Temperature increases of hundreds of Kelvin were reported when trapping gold nanoparticles near lipid vesicles exhibiting temperature-sensitive permeability [60]. Such high increases in local heat intensities are generally undesirable especially when trapping dielectric particles as this might have some damaging effects [1]. In addition, recent works on protein studies, like resonant-based plasmonic trapping [61–63] and photonic crystal trapping systems [64, 65] are prone to heating issues and it might be needed to address them by applying a number of thermal management strategies; for example, by using adjacent metal films as a natural heat sink in nanopillar plasmonic trapping [66, 67].

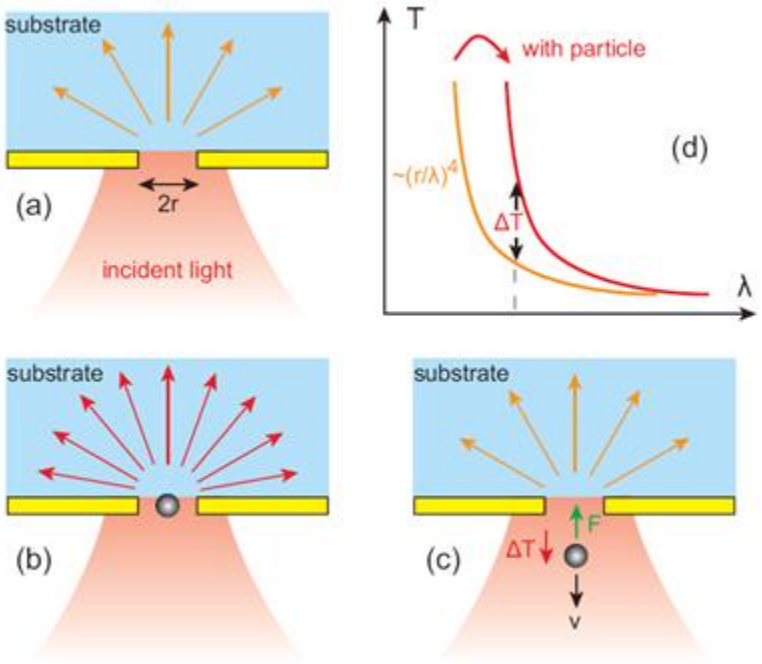

Figure 2.1: Optical transmission through a single subwavelength circular aperture: (a) without dielectric particle. (b) Transmission is enhanced with a dielectric particle in the circular aperture. (c) Transmission is decreased by T as the particle tries to escape from the aperture and as a result the total photon momentum traveling through the aperture decreases. This induces a force F in the opposite direction pulling the particle back to the hole. (d) The presence of the dielectric particle makes the aperture optically larger, red-shifting the transmission hence giving an increase in the transmission by ΔT. Reprinted from Ref. [53], Copyright 2012, Y. Pang.

Nanoaperture-based trapping, on the other hand, has the advantage of good thermal conductivity of the metal film which reduces significantly the heating effect. The temperature rise at the trapping site is expected to be on the order of 0.1 Kelvin [67]. Indeed, nanoapertures in metal films have shown three orders of magnitude lower heating than in resonant nanorod antennas [68].

2.3 Self-Induced Back-Action Optical Trapping

2.3.1 Motivation for Self-Induced Back-Action Trapping

Extending optical trapping towards the nanometer regime with moderate optical powers requires a situation where the trapped particle plays an active role in the trapping mechanism. It was shown in the previous section that a small change in the electromagnetic environment surrounding a subwavelength aperture in a metal film, such as by the presence of a dielectric object with a refractive index higher than that of the surrounding medium, causes an increase in the transmission through it, Fig. 2.1. Therefore, if the trapped particle tries to escape from the aperture transmission decreases with a corresponding drop in the total photon momentum traveling through the aperture. Therefore, a restoring force in the opposite direction, according to Newton's Third Law, will act upon the particle to balance the momentum rate change; hence pulling it back to the equilibrium position towards the opening of the aperture, as shown in Fig. 2.1(c). This so-called self-induced back-action (SIBA) trapping approach offers superior trapping ability at lower powers for Rayleigh particles and provides an automatic feedback control without the need for any external monitoring mechanisms [69–71].

In order to illustrate the SIBA effect, we consider the particle at the equilibrium position at the opening of circular aperture, the forces associated with the photon transmission rate and Newton's third law. There is a decrease in the rate of photon momentum traveling through the aperture associated with the drop in transmission as the particle moves away from the aperture. Therefore, by Newton's third law, a force in the opposite direction will act on the particle to balance this momentum rate change. This force pulls the particle towards the opening of the aperture to the equilibrium position. In addition, there is a lateral force due to symmetry breaking

of an offset particle in the aperture. As the particle moves towards the edge of the aperture, an increased enhancement of the field is obtained thereby enhancing trapping efficiency [72].

Although the optical force formulation (Eq. 2.4) gives a good approximation of the forces acting upon a particle in a homogeneous electromagnetic environment [3, 73], it does not account for the strong change to the ambient electromagnetic environment caused by the trapped dielectric particle - as in the case for SIBA trapping. Therefore, working beyond the perturbative gradient force approximation necessitates the use of the comprehensive Maxwell stress tensor (MST) analysis. The force acting on a dielectric particle in this case is given by [74]

$$F = -\frac{1}{4}\varepsilon_0 \left(\int_V E^* E \nabla \varepsilon_r dV \right) \tag{2.7}$$

where the superscript $*$ denotes the complex conjugate, ε_0 is the free-space permittivity and ε_r is the relative permittivity of the dielectric particle. It should be noted here that in Eq. 2.7 the direction of E is defined by the polarization of the incident laser beam, and F is directed towards the stable trapping point which is at the aperture side.

Finite-difference time-domain (FDTD) simulations were performed for a nanohole circular aperture comparing two physical formulations for computing the optical force acting upon a trapped dielectric particle: the perturbative gradient force formulation and the rigorous MST analysis [72]. Usually, in the perturbative approach the electromagnetic fields are calculated without the object and then the forces are computed using the point–dipole approximation [75]. As for the MST, the particle is included in the electromagnetic simulations a priori in order to calculate the trapping forces on the particle [76]. Recent works on nanostructured optical traps have shown good agreement between the perturbative dipole approximation and the MST methods [73].

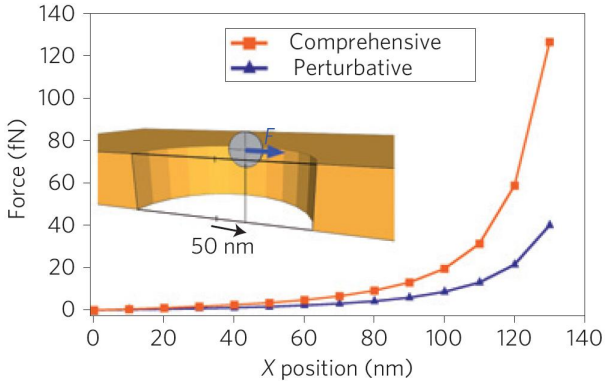

Figure 2.2: Numerical evaluation of the lateral trapping force acting upon a 50 nm polystyrene particle as a function of the distance to the aperture centre in a subwavelength nanohole optical trap using the rigorous MST analysis and the gradient force method. The calculations were made for an injected power in the aperture of 1 mW. Reprinted from Ref. [72], Copyright 2009, Nature Publishing Group.

However, simulation results for the SIBA–based circular aperture trapping revealed that MST analysis predicts much larger optical forces as compared with the gradient force method, Fig. 2.2. This is due to the fact that SIBA–based trapping is not perturbative and that the trapped particle has an active role in trapping mechanism.

SIBA trapping relaxes the requirement for high laser intensities to values associated with a potential depth of the order of k_BT. In addition, the restoring force of SIBA enables the the depth of the trapping potential to be automatically increased during high energy events and thereby maintaining the object within the trap, as illustrated in Fig. 2.3 [77]. Trapping using the SIBA effect with a simple circular aperture was used to achieve stable trapping of 50 nm polystyrene with only 1 mW of laser power [72] opening the doors to trap < 100 nm particles with low powers.

2.3.2 SIBA Trapping Regimes

SIBA trapping can be categorized into three detuning regimes depending on the aperture resonance with respect to the trapping laser wavelength [78]. These regimes are referred to as: blue–shifted regime, resonant and red–shifted regime as shown in

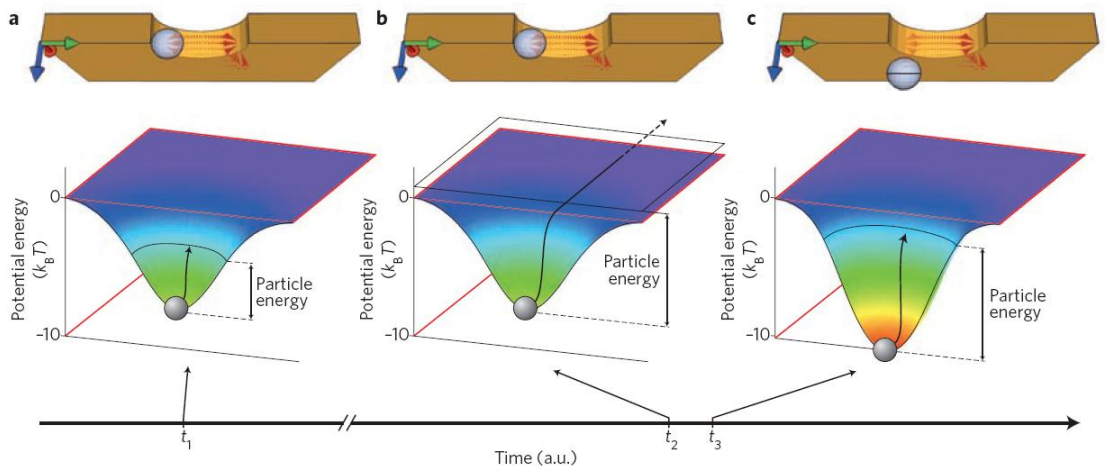

Figure 2.3: Schematic of a SIBA trapping setup for a 310 nm aperture in 100 nm gold film and 100 nm polystyrene particles in water. (a) The particle is localised in the aperture at time t_1 while having moderate kinetic energy. (b) During high energy event at time t_2 the object can escape from the aperture. (c) The depth of the trapping potential becomes deeper and pulls back the particle as it is about to escape from the aperture at time t_3. Reprinted from Ref. [77], Copyright 2013, Nature Publishing Group.

Fig. 2.4(a). The blue–shifted regime is the most reported in the literature. In this regime, once the particle is trapped the resonance red–shifts towards the laser line causing an increase in the local field and the transmission through the aperture. On the other hand, working in the red–shifted regime leads to a transmission decrease upon trapping of the particle in the aperture. Finally, when trapping occurs in the resonant regime, the system symmetrically red–shifts through the resonance. In this situation, the transmission levels of the trapped and untrapped states are comparable. Fig. 2.4(b) shows the experimental transmission time traces of the three detuning regimes for bowtie nanoapertures.

2.3.3 Advantages of SIBA Trapping

SIBA trapping relies on the active dynamic role the target particle plays in the trapping mechanism creating larger change in the ambient electromagnetic field than that

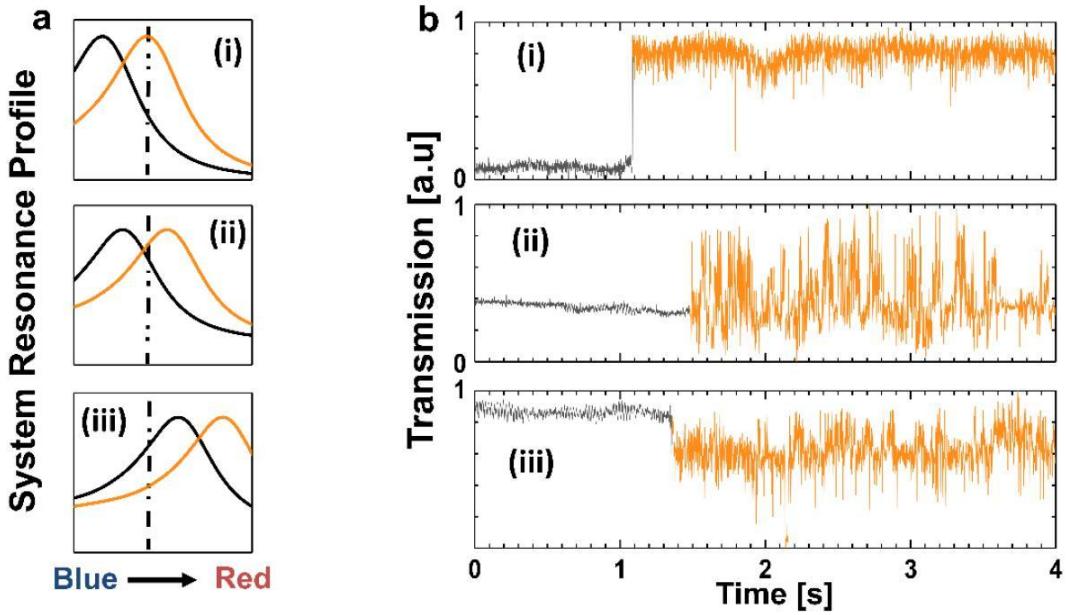

Figure 2.4: (a) Aperture resonance shift for the three possible detuning regimes: (i) blue–shifted, (ii) resonant and (iii) red–shifted. The black trace corresponds to an empty trap and the orange one to a particle being trapped. The dashed line represents the excitation laser wavelength. (b) Experimental transmission time traces for the three detuning regimes. Reprinted from Ref. [78].

predicted by Rayleigh scattering and hence opening up the doors to work beyond the perturbative regime. Unlike other trapping schemes that require advanced scattering schemes [39, 79, 80] or fluorescence monitoring [48], the high sensitivity of the SIBA trapping approach allows for trapping detection by simply measuring the transmission through the aperture. Although the SIBA approach was first demonstrated with subwavelength circular apertures in metal films, the concept has been applied to a number of other aperture geometries as will be discussed in detail below. In addition, the generality of the SIBA approach can be optimized to accelerate efforts in the fields of nano-optics and metamaterials towards sensing applications [74, 81–85].

It should be noted here that nanoaperture SIBA-based optical tweezers do not require resonance from the trapped object, which makes them fundamentally different from trapping using resonances of atoms [86, 87] or quantum dots [88]. In addition,

while plasmonic based optical tweezers utilize localized surface plasmons to enhance the radiation force [89–93], SIBA-based optical tweezers rely on the strong influence the trapped particle has on the electric field to achieve a stable robust trapping.

Furthermore, unlike microresonator trapping systems [94–100], which rely on high quality resonance, aperture-based SIBA tweezers are not as sensitive to wavelength and a straight forward measurement of the transmission of the same trapping laser beam through the aperture can be used to detect trapping events. This is due to the fact that nanoapertures are naturally background signal free. Therefore, nanoaperture tweezers can also be thought of as sensors, with reported signal-to-noise ratios (SNR) of up to 33 [31]. This has made them useful tools, not only for detecting single molecules, but also for observing their molecular interactions, as will be discussed in Chapter 4.

2.3.4 Nanoaperture Trapping Geometries

Although circular apertures in metallic films, Fig. 2.5(a), were used to stably trap 50 nm polystyrene particles with low powers [72], extending optical trapping towards even smaller particles requires looking for new nanoaperture designs. A number of nanoaperture shapes have been suggested for increased transmission [101–104], enhanced second harmonic generation [105, 106], surface enhanced Raman scattering (SERS) [107] and for local field enhancement [108–110]. In addition, the cutoff wavelength of a certain aperture shape might be different than other apertures of the same area [111]. Trapping 22 nm polystyrene particles was achieved using a rectangular plasmonic nanopore [112], as shown in Fig. 2.5(b). Such a rectangular aperture has the advantage that the propagating gap plasmons can be tuned by adjusting its geometrical aspect ratio. In addition, it has a stronger resonant transmission than a circular aperture of the same area, yet both circular and rectangular apertures

have the disadvantage of not having a sharply defined trapping site in the aperture. Double nanohole apertures, as shown in Fig. 2.5(c), were used for trapping a single protein [31], a 12 nm silica sphere [113] and a single DNA molecule [32]. Experimental results show that the double nanohole aperture trap can trap smaller particles more easily than larger particles, which is the opposite for other optical traps [113]. This is due to the sensitivity to the gap size between the two nanoholes - it should be commensurate with the particle size. The bowtie nano-aperture geometry, Fig. 2.5(d), combines high collection cross section and transmission with strong mode confinement, which also makes it a good candidate for SIBA trapping. Three-dimensional optical manipulation of 50 nm polystyrene particles was achieved using the bowtie nanoaperture on a tapered optical fiber [114].

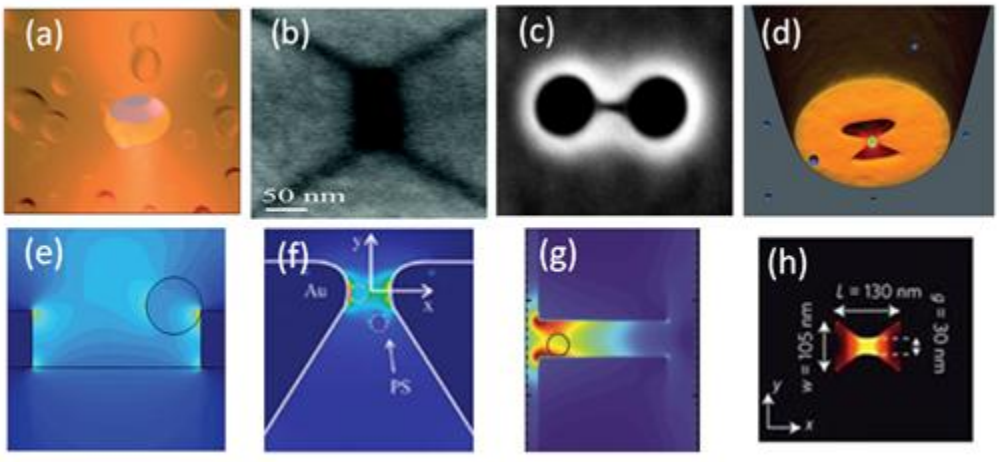

Figure 2.5: Nanoaperture trapping geometries with corresponding near-field intensity maps: (a),(e) circular aperture, reprinted from Ref. [72], Copyright 2009, Nature Publishing Group. (b),(f) rectangular aperture, reprinted from Ref. [112], Copyright 2011, American Chemical Society. (c),(g) double nanohole aperture, reprinted from Ref. [113], Copyright 2011, American Chemical Society, (d),(h) bowtie nanoaperture. Reprinted from Ref. [114], Copyright 2013, Nature Publishing Group.

Numerical simulation results of various aperture trapping geometries, Fig. 2.5(e), (f), (g), (h), show that an enhancement in the local electric field intensity is obtained in the vicinity of the nanoapertures. This enhanced local field intensity is altered

by the presence of the trapped particle. Therefore, as the particle tends to escape from the trap a SIBA force acts upon it pushing it back to the aperture, providing self-feedback on the particles dynamics in the trap.

2.4 Summary

In summary, this chapter introduced the basic concepts of single beam gradient force optical tweezers highlighting their limitations for trapping biomolecules. Aperture based optical trapping systems were introduced as an alternative for conventional gradient force tweezers. Motivation for SIBA-based trapping system was then presented highlighting its unique features which has enabled trapped single molecules with low optical powers.

Chapter 3

Double Nanohole Optical Tweezer System

This chapter takes a closer look at the double nanohole aperture in terms of its features and its fabrication procedure. The chapter then describes the double nanohole tweezer experimental setup and how the double nanohole chip is assembled. Then the chapter highlights the mechanism by which trapping events are detected in the double nanohole tweezer system. Towards the end of the chapter, it is shown how the double nanohole tweezer system can be used to identify the trapped particle and probe its vibrational modes.

3.1 Motivation for Double Nanohole Apertures

It was mentioned in the previous chapter that a number of nanohole apertures have been implemented for trapping applications. However, in this thesis we mainly focus on using the double nanohole aperture. Double nanohole apertures have been used for enhanced second harmonic generation [105, 106] and surface enhanced Raman Scattering (SERS) [107] and for fluorescence enhancement [115]. In fact, the narrow

gap between the two cusps of the double nanohole aperture leads to a high local field enhancement which results in a strong trapping point, Fig. 3.1. The sharp corner edges of the bowtie apertures makes them prone to having more than one trapping point due to the enhancement of the field at those corner regions. However, the double nanohole aperture has one strong trapping point located in the narrow gap of the aperture.

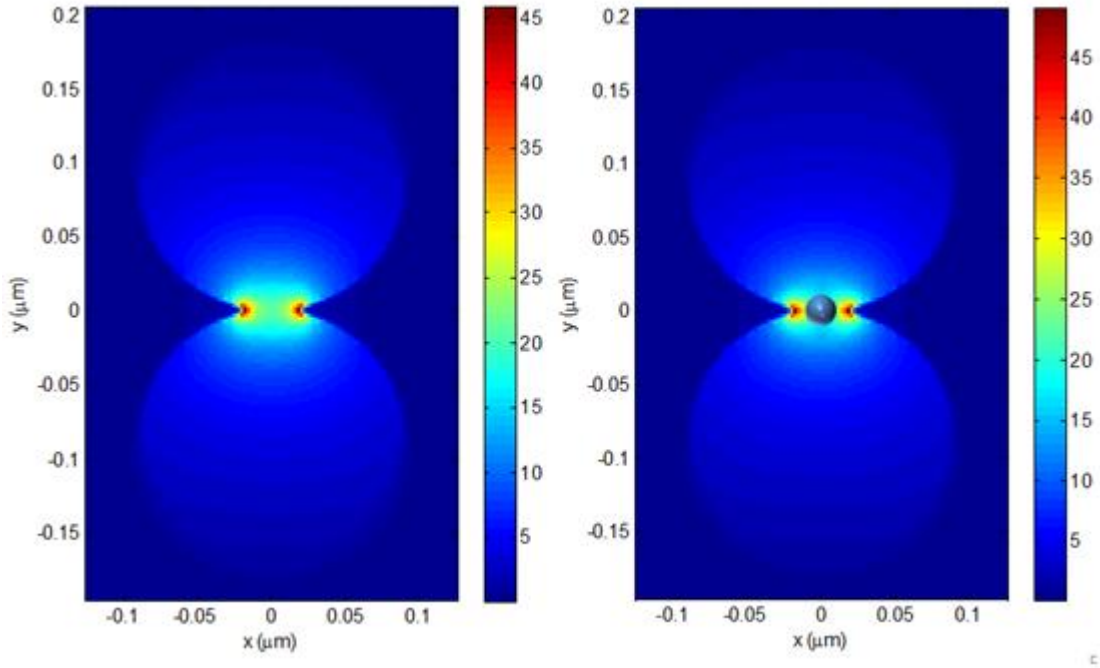

Figure 3.1: Field intensity map of a double nanohole aperture (a) without and (b) with a 20 nm polystyrene particle in the vicinity of the two cusps of the aperture.

In addition, the good thermal conductivity of the Au film plays a role in reducing the heating affects associated with incident laser beam and hence making it suitable for trapping dielectric objects including biological molecules. Furthermore, double nanohole apertures are relatively easier to fabricate as compared to bowtie apertures [114].

3.2 Resonances of the Double Nanohole Aperture

It was mentioned previously in Section 2.3.2 that SIBA trapping can be categorized into three detuning regimes depending on the aperture resonance with respect to the trapping laser wavelength. Therefore, it is important to study the resonances of the aperture in order to quantify their effect on optical trapping . For the double nanohole aperture, three types of resonances have been identified: a plasmonic resonance, a Fabry-Pérot (FP) like resonance and a wedge resonance [116]. In order to study these resonances, FDTD simulation was preformed. In these simulations, a total-field scattered-field (TFSF) source was used and the 3D simulation region containing the double nanohole aperture was enclosed with perfectly-matched-layer (PML) boundaries. The double nanohole aperture geometry is defined by the thickness of the Au layer, T, the diameter of the circular aperture, D, the centre-to-centre distance between the two circular apertures, L, the curvature of the cusps, C, and width, W, of the gap as shown in Fig. 3.2(a). The system was excited by normally incident plane wave with linear polarization along the x direction.

It is clear from Fig. 3.2(b) that the double nanohole aperture has three resonances. For the zeroth order FP mode (FP_0) at 1323 nm there is a uniform electric field intensity distribution along the metal thickness (top of Fig. 3.2(c)). Also, there is one node that appears at the middle of the cavity for the FP_1 resonance at 798 (bottom of Fig. 3.2(c)). These two FP resonances are referred to as gap mode FP resonances due to the fact that the field intensity is largest and confined in the gap. Similar resonances have been reported in the literature for the bowtie nanoaperture [117,118]. In addition to the previously studied gap mode FP resonances, the double nanohole aperture supports a resonance at the wavelength of 1182 nm. Whereas the gap mode FP resonances have their largest field intensity in the gap, the field intensity distribution of this recently reported mode shows enhancement around the edge of

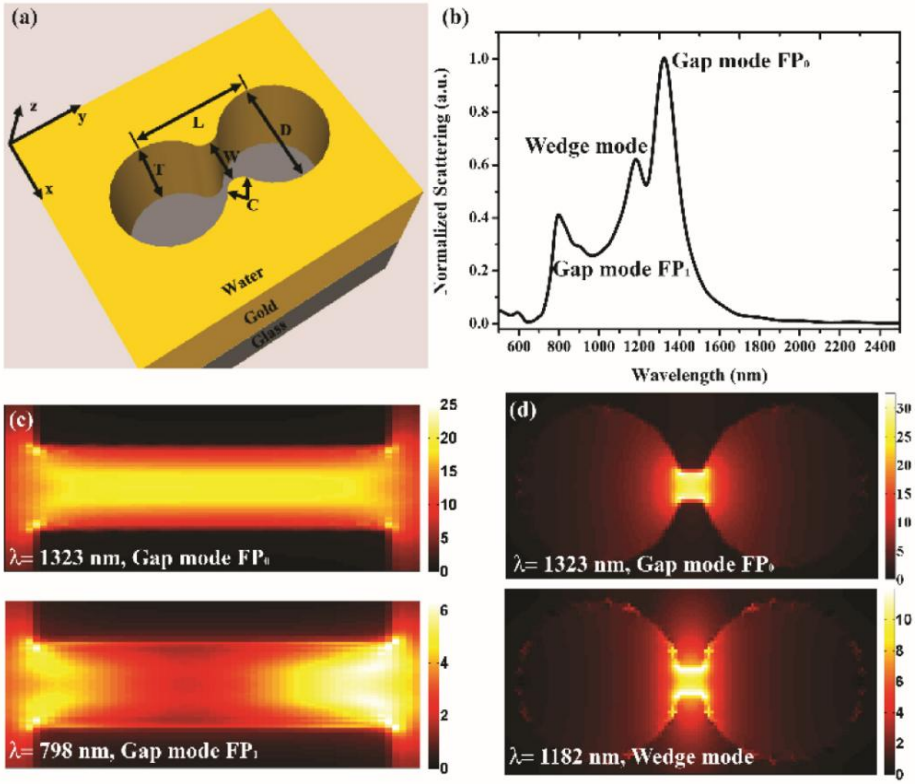

Figure 3.2: (a) Schematic view of a double nanohole aperture in metal film. The geometry of the aperture is defined by the thickness of the metal, T, the diameter of the circular aperture, D, the distance between the two circular apertures, L (the center-to-center separation), the curvature, C and width, W of the gap. (b) The transmission spectra of the double nanohole aperture with T = 150 nm, D = 120 nm, L = 130 nm, W = 30 nm and C = 0.035. The index of the substrate and the water is 1.51 and 1.33. (c) Electric field intensity distributions in the x-z plane for λ = 1323 nm, λ = 798 nm. (d) Electric field intensity distributions in the x-y plane for λ = 1323 nm, λ = 1182 nm. Reprinted from Ref. [116], Copyright 2015, OSA.

the gap of the double nanohole aperture and inside the metal, as shown in Fig. 3.2(d). Since the field intensity distribution of this resonance is similar to the wedge plasmon waveguide [119], it has been referred to as the wedge resonance [116]. It should be mentioned here that both the gap mode FP_0 resonance as well as the wedge mode resonance occur close to their cut-off values implying their dependance on the geometry of the aperture not the film thickness. In contrast, a resonance shift from 732 nm to 913 was observed for the FP_1 gap mode when the Au film thickness was

varied from 100 nm to 200 nm. Therefore, it is expected that trapping performance to be affected by varying the Au film thickness when working close to the FP_1 gap mode, as discussed in Section 2.3.2.

3.3 Double Nanohole Aperture for Optical Trapping

3.3.1 Experimental Setup

The double nanohole optical tweezer system is based on an inverted microscope setup, Fig. 3.3. The trapping laser beam is focused into the gold sample which contains the double nanohole trap using a 100× oil immersion microscope objective with a 1.25 numerical aperture. A half-wave plate (HWP) is used to rotate the polarization of the incident laser beam so that the electric field of the beam is aligned along the two cusps of the double nanohole aperture, giving a large local field enhancement and hence creating a strong trapping point. Transmitted light through the aperture is collected using a 10× condenser microscope objective with 0.25 numerical aperture, and measured by a silicon-based avalanche photodetector (APD) (Thorlabs APD110A). A data acquisition board is used to record the voltage values generated by the APD at a sampling frequency of 1 MHz. This technique produces copious signal for only 3 mW of laser power (1.68 MWm^{-2}), such that an optical density filter is used to avoid saturation of the APD.

3.3.2 Trapping Detection

Fig. 3.4(a) shows a typical time evolution of the optical power transmitted through the double nanohole aperture. A trapping event is detected by monitoring light

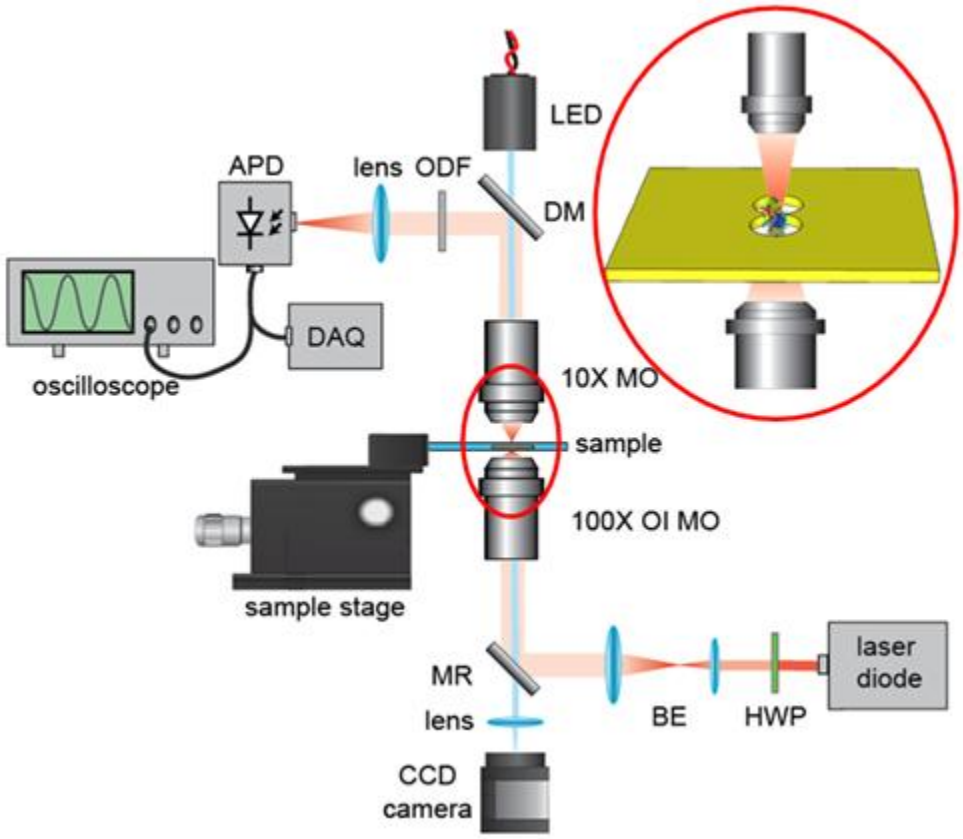

Figure 3.3: Schematic of the double nanohole aperture optical trapping setup. Abbreviations used: HWP = half-wave plate; BE = beam expander; MR = mirror; MO = microscope objective; OI MO = oil immersion objective; DM = dichroic mirror; ODF = optical density filter; APD = avalanche photodiode; DAQ = data acquisition card. Inset: zoomed-in representation of the double nanohole aperture trapping site (Complete representation of the chip is given in Fig. 3.8).

transmission through the double nanohole aperture as measured by the APD which is seen as a discrete increase in the transmission due to dielectric loading; and hence an increase in the APD voltage level (denoted by the arrow in Fig. 3.4(a)). It is expected that the particle is trapped inside the aperture close to the glass substrate where the local field intensity is highest which would result in higher increase in transmission levels. It is clear from Fig. 3.4(a) that the monitored APD signal does not only abruptly increase when a trapping event occurs but also associated with it is a substantial increase in the signal fluctuation, which manifests itself clearly by

plotting the autocorrelation of the APD signal in the untrapped and trapped states, Fig. 3.4(b). This increase in the signal fluctuation is attributed to the Brownian motion and the conformal changes of the molecule in the double nanohole aperture trap; and hence contains information specific about the trapped molecule as will be shown in the subsequent chapters.

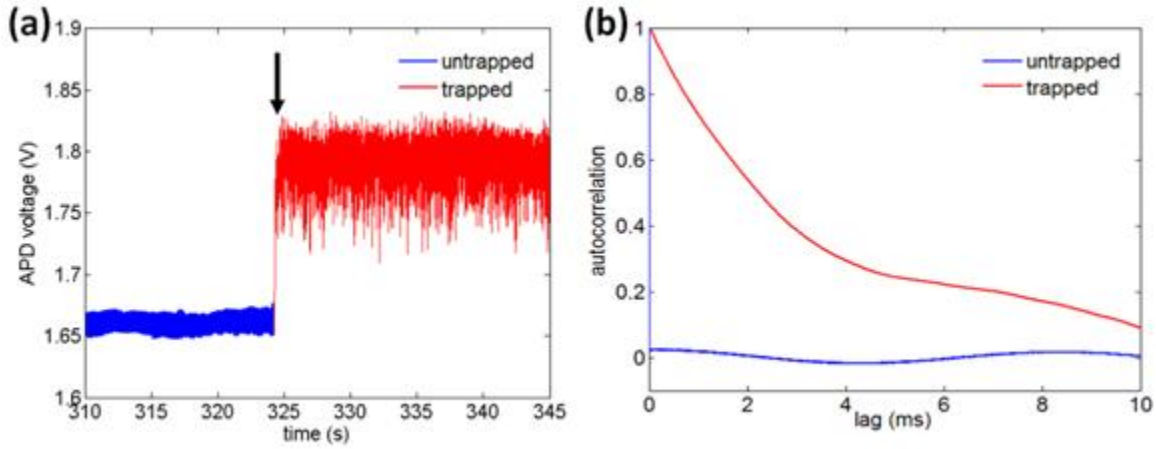

Figure 3.4: Typical trapping event of a biotinaylated streptavidin molecule in the DNH aperture. (b) Autocorrelation of the APD signal for the untrapped and trapped states as shown in (a).

3.3.3 Fabrication of the Double Nanohole Aperture

The double nanohole apertures used in all the experiments were milled using a Hitachi FB-2100 in 100 nm thick Au on a glass substrate with a 5 nm titanium adhesion layer. At 80,000 magnification, focused gallium ion beam (FIB) is used to fabricate the double nanohole structure. The accelerating voltage and current of the gallium ion beam is 40 kV and 0.001 nA. The magnification at which the structure is fabricated and accelerating voltage of the beam as well as the number of passes and the dwell time are the parameters that can be varied to obtain the desired structure with the desired specifications, i.e. hole size, hole separation and gap size. The FIB takes the bitmap file that contains the drawing of the structure and fabricates it based on the

input parameters. For example, Fig. 3.5 shows the bitmap file for a double nanohole structure with a radius of 60 nm and hole separation of 15 nm.

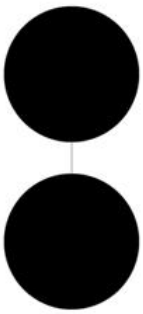

Figure 3.5: Bitmap file of a double nanohole structure with a radius of 60 nm and hole separation of 15 nm.

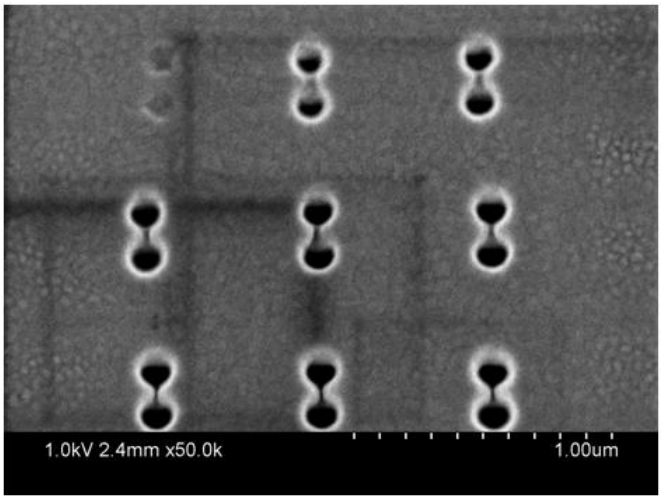

Figure 3.6: Fabricated double nanohole structures using the bitmap file in Fig. 3.5.

Fig. 3.6 shows a 3 x 3 double nanohole array obtained by fabricating the bitmap in Fig. 3.5. Here the double nanohole apertures were fabricated using the same beam and at the same magnification but with varying number of passes. It is clear that varying fabrication parameters results in slightly different output and these parameters can be used to obtain the desired output specification. It is possible that milling

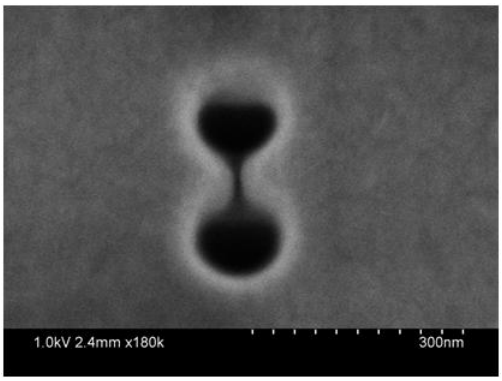

Figure 3.7: A zoomed-in image of a single double nanohole from Fig. 3.6

is extended into the glass substrate – up to 100 nm depending on the parameters used in the fabrication process. In some cases, imperfect double nanohole apertures are obtained and this affects the performance of the aperture as the geometry (and consequently the resonance and the local field enhancement) is changed. This might also affect the detection of trapping events as discussed in Section 2.3.2. Fig. 3.7 shows a zoomed-in image of one of the double nanoholes milled in Fig. 3.6.

3.3.4 Double Nanohole Aperture Chip Assembly

Fig. 3.8 schematically shows the steps for the double nanohole aperture chip assembly, which is summarized as follows:

- The double nanohole aperture is fabricated on gold film sample as describe in the previous section.
- A microchamber is formed by placing an imaging spacer (Secure Seal imaging spacer, Grace Bio-labs) with a hole diameter of 9 mm and thickness of 90 - 100 μm on an 80 - 130 μm thick number 0 cover glass (GoldSeal, Ted Pella, inc).
- 10 μL of the protein solution is then pipetted into the chamber.

- The gold sample (with the gold side facing down) is placed on the imaging spacer to seal the well. The whole sample assembly is then mounted in the inverted microscope optical trapping setup as shown in Fig. 3.3.

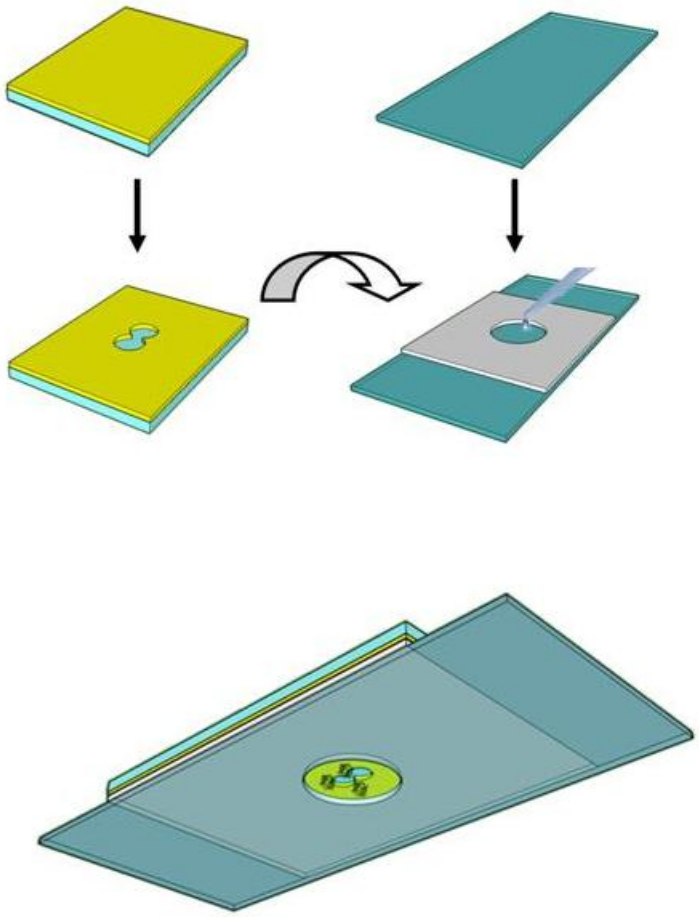

Figure 3.8: Double nanohole aperture chip assembly procedure.

3.4 Single Particle Spectroscopy of Trapped Particles

3.4.1 Raman Spectroscopy

The double nanohole optical tweezer system has been used to simultaneously trap an object and record its Raman signal. This was achieved by integrating a Raman spectroscopy setup with the double nanohole tweezer system [120]. In that work single nanoparticle sensitivity was achieved by obtaining the characteristic Raman peaks for 20 nm polystyrene and titania nanoparticles while trapped in the double nanohole aperture, Fig. 3.9. Although the Raman Signal was obtained in the reflection mode, it is possible to obtain the Raman spectra in the transmission mode but with longer integration times. It is worth noting here that luminescence from the gold surface was observed but the Raman signal for the polystyrene and titania spheres were strong enough to be detected without the need to eliminate the luminescence from the gold surface. This method combines the surface enhanced Raman spectroscopy with the double nanohole optical tweezer system for isolation and identification of nanoparticles.

3.4.2 Acoustic Raman

The double nanohole optical tweezer system has also been used to excite acoustic Raman modes of single polystyrene particles as well as single proteins and DNA molecules [34, 121]. This was achieved by trapping the particle with two tunable trapping lasers as opposed to a single fixed laser source. In that work, once the particle is trapped in the double nanohole aperture, the two lasers are detuned from each other creating a beat frequency. When the beat frequency matches one of the

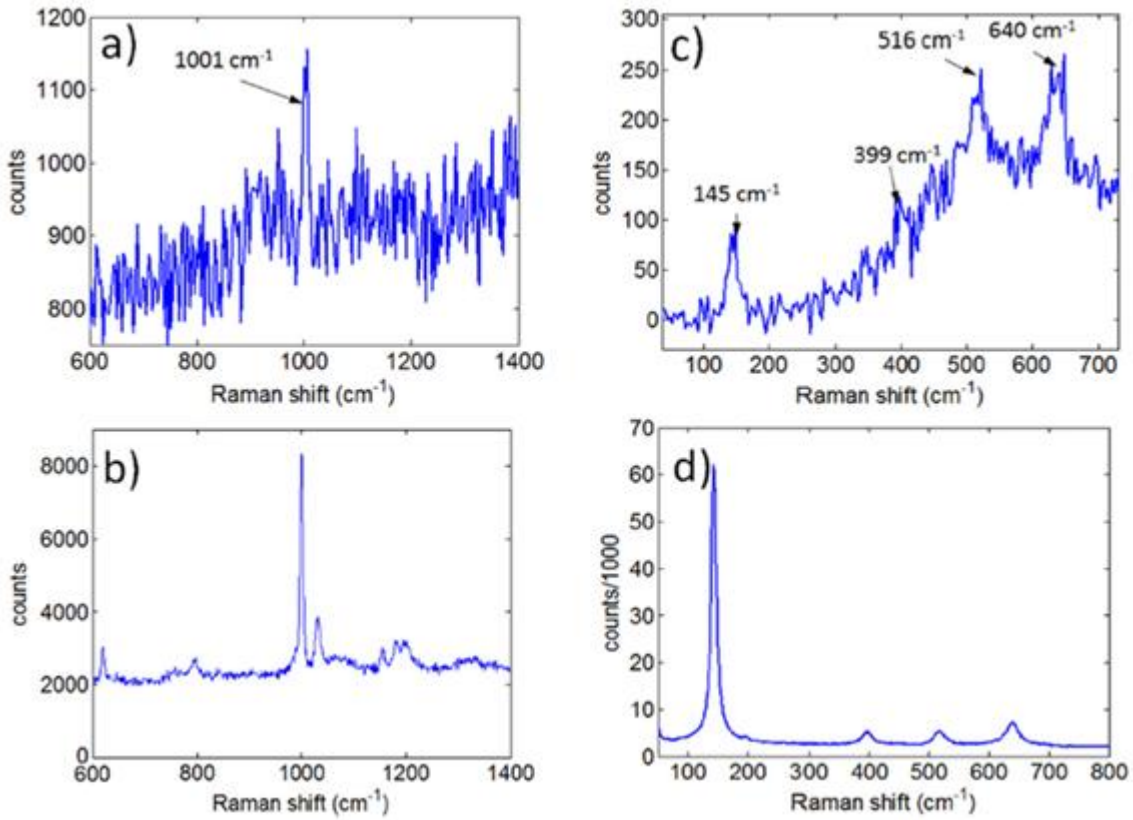

Figure 3.9: (a),(c) Raman spectra of trapped 20 nm polystyrene and titania particles. (b),(d) Raman spectra for bulk polystyrene and titania solution as a reference. Reprinted from Ref. [120], Copyright 2015, IOP Publishing.

acoustic modes of the trapped particle it causes an increase in the motion of the particle and hence the resonance is detected by noting the increase in the fluctuation of the signal transmitted through the double nanohole aperture. As opposed to IR active modes which result from a change in the permanent dipole moment of the molecular bond, Raman active modes result from a change in the polarizability of the molecule. The beat frequency stretches the molecule which changes its polarizability and thus only excites Raman active modes of the molecule. Fig. 3.10 shows the acoustic Raman spectra obtained for carbonic anhydrase and conalbumin molecules while trapped in the double nanohole aperture.

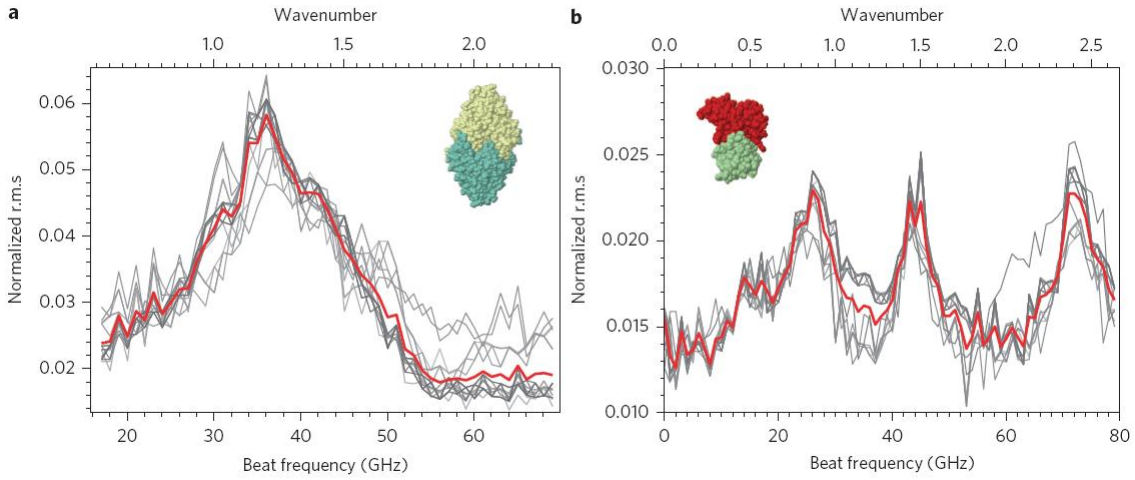

Figure 3.10: Raman spectra of two globular proteins. (a) 22 different sweeps across 11 trapping events of carbonic anhydrase showing a singular broad peak centered around 38 GHz. (b) 20 different sweeps across 10 trapping events of conalbumin showing 2 distinct peaks and a single finely split peak. Red curves show the average of all sweeps. Reprinted from Ref. [34], Copyright 2014, Nature Publishing Group.

3.5 Summary

In summary, this chapter looked the double nanohole aperture highlighting its features and fabrication procedure. In addition, the experimental setup for the double nanohole tweezer was described. Furthermore, the mechanism by which trapping events are detected was explained. Also, the fabrication and chip assembly procedures of the double nanohole aperture was highlighted. Towards the end of the chapter, results on single particle spectroscopy of trapped particles in the double nanohole aperture using the conventional Raman as well as acoustic Raman were presented.

Chapter 4

Double Nanohole Optical Tweezers for Single Protein Studies

4.1 Introduction

Protein-small molecule interaction (PSMI) studies typically use surface immobilization techniques combined with labeling [122, 123], Fig. 4.1. Surface immobilization uses some of the molecules binding sites and restricts its free motion; hence preventing it from being in its native state [124, 125]. Besides heating issues, labeling techniques suffer from photobleaching, blinking and low signal for single molecule applications [126, 127]. In addition, as is the case with surface immobilization, labeling disrupts the natural state of the molecule; hence affecting the accuracy of the data [128, 129]. However, in an attempt to overcome the problems associated with surface immobilization and labeling, a number of label-free, free-solution methods like calorimetery [130–132], enthalpic arrays [133] and interferometery [134] have been suggested. However, these alternative ensemble methods have disadvantages, like long preparation times, low sensitivity and poor detection limits.

This chapter introduces the double nanohole aperture optical tweezer system as an alternative method for observing and studying molecular interactions at the single molecule level in a label-free free solution environment. The chapter starts by describing some of the advantages of using the double nanohole tweezer system for studying PSMIs. Then, it summaries the work that has been carried out during the PhD period in relation to using the double nanohole aperture for single protein studies. First, it describes how the double nanohole aperture has been used to detect protein binding at the single molecule level. Then it looks at how the double nanohole aperture can distinguish between proteins with and without a ligand attached to them. It also presents a label-free free solution an optical tweezer approach to finding the binding kinetics of PSMIs.

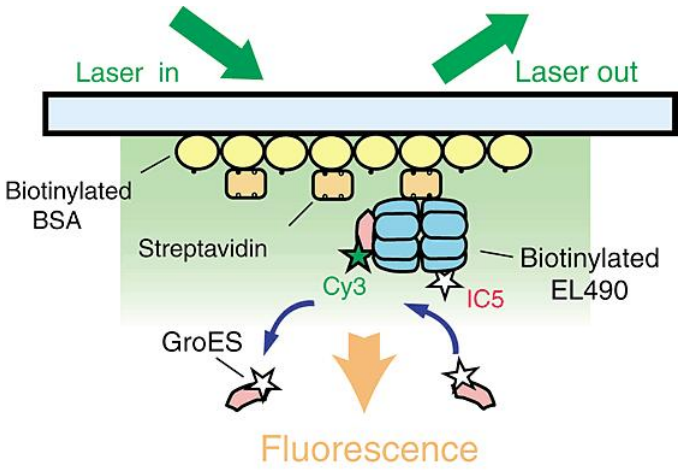

Figure 4.1: Schematic drawing of an experiment to find the binding kinetics at the single molecule level using total internal reflection fluorescence microscopy. Fluorescently labeled protein, EL490, was immobilized on a glass surface through a biotinylated bovine serum albuminstreptavidin linker. The flow cell containing the immobilized EL490 was filled with Cy3-labeled GroES (Cy3-ES). Reprinted from Ref. [122], Copyright 2001, Nature Publishing Group.

4.2 Advantages of Using the Double Nanohole Tweezer System for Protein Studies

The double nanohole tweezer system intrinsically inherits the advantages of SIBA based optical trapping systems outlined in Section 2.3.3. In addition to that, the double nanohole tweezer system offers unique features which makes it an attractive method for protein studies for a number of reasons.

First, the double nanohole tweezer system allows for working at the single molecule level without the need for tethers or labels and hence can provide information about single molecule interactions which are not accessible by ensemble methods [135, 136].

Second, protein-protein interactions are very temperature-sensitive and nanoaperture optical tweezers have been successfully used to trap 12 nm dielectric particles using around 3 mW of laser power [113]. The good thermal conductivity of the metallic film of the nanoaperture plays an important role in dissipating any heat generated at the trapping site. It is worth noting here that some challenges might arise when using pulsed lasers as the high peak power of the pulsed laser might result in damaging the aperture or the trapped particle or both.

Third, the high sensitivity of the transmitted light in nanoaperture tweezers to the shape, size and refractive index of the trapped particle [33] makes them excellent candidates for detecting molecular interactions. Light transmitted through the double nanohole aperture was used to observe the real time dynamics and to distinguish between the bound and unbound forms of a protein [137].

Forth, unlike fluorescent-based methods, which due to blinking and bleaching are limited in terms of observation times [138], nanoaperture tweezers can extend observation times to hours and maybe days.

Fifth, cost and labour associated with tethering (for surface immobilization) and

labeling and photon counting in fluorescent measurements makes them expensive as compared with current nanoaperture optical tweezers setups. It has been shown that it is possible to integrate nanoapertures at the end of optical fibers [114, 139], hence bringing the cost even lower.

Sixth, although calorimetric methods such as isothermal titration calorimetry have been used widely for studying molecular interactions [130–132], they are restricted to systems with an appreciable reaction enthalpy and require large sample volumes (milliliters). In contrast, the double nanohole aperture system does not require the systems to be exothermic and sample volumes can be less 15 μL – depending on the the size of the microchamber used (Section 3.3.4). In addition, the double nanohole aperture system works at the single molecule level and can be intergrated with microfulidics in order to enable sequential delivery of the desired solutions to the trapping site (Section 4.3) which is not possible with isothermal titration calorimetry.

4.3 Observing Single Protein Binding by Optical Transmission Through a Double Nanohole Aperture in a Metal Film[1]

Single protein binding studies typically bind a protein to a surface and then look at protein interactions through additional binding events [140–142]. A number of studies have shown single protein binding sensitivity using plasmonic nanoparticle by monitoring resonance shifts [143–145] and by photo-thermal transduction to achieve increased sensitivity [146]. Those works, however, have the disadvantage of using some of the binding sites of the molecule for surface immobilization and hence ob-

[1]The following section is adapted from: A. A. Al Balushi, A. Zehtabi-Oskuie, R. Gordon, Observing single protein binding by optical transmission through a double nanohole aperture in a metal film, Biomed. Opt. Exp. 4(9), 1504-1511 (2013).

scuring/blocking a specific side of the protein by the surface. They also restrict the motion of the protein, and so the binding event is not in its native state.

4.3.1 Experiment and Results

The double nanohole aperture trap integrated with microfluidic channels, have been used to trap a single bovine serum albumin (BSA) molecule and then co-trap it with anti-BSA in a label-free free-solution microfluidic environment [147]. When a single BSA molecule gets trapped between the cusps of the double nanohole aperture it dielectrically loads the region and causes an increased in the transmission. Once a stable trapping of a single BSA molecule was achieved, anti-BSA was flowed into the channel where it got bound to the already trapped BSA molecule, causing further dielectric loading to the double nanohole aperture region and consequently a higher optical transmission was obtained.

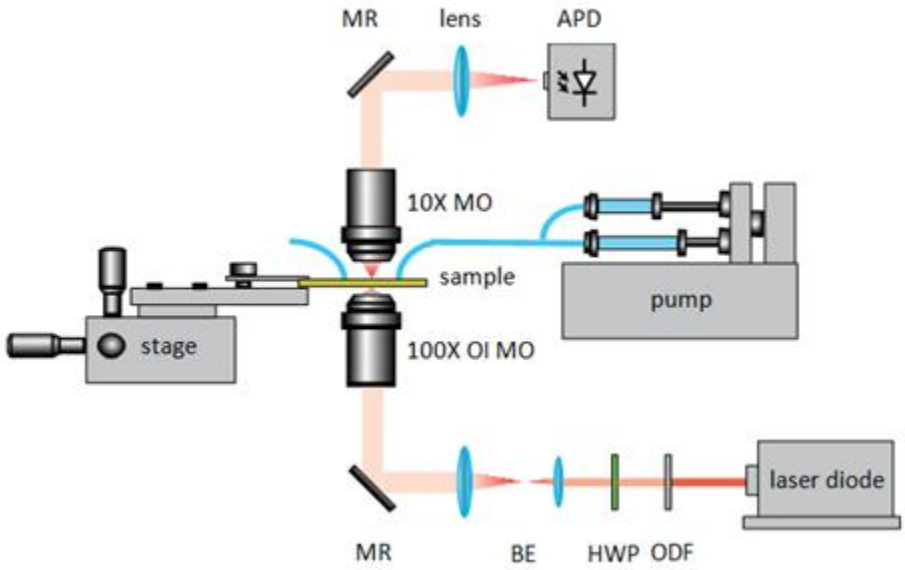

Figure 4.2: A schematic of the double nanohole optical trap with dual microfluidic input. Reprinted from Ref. [148], Copyright 2013, OSA.

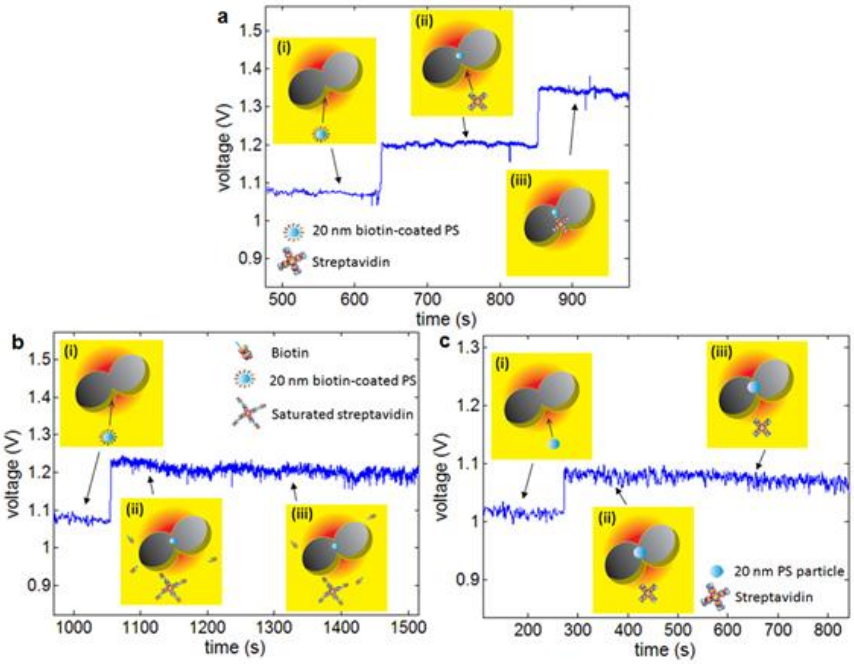

Figure 4.3: (a) Demonstration of single protein binding using the double nanohole aperture: (i) flowing 20 nm biotin-coated polystyrene particles, (ii) trapping event of 20 nm biotin-coated polystyrene particle in the double nanohole aperture and subsequently flowing streptavidin, (iii) binding of streptavidin with the trapped biotin-coated polystyrene particle. (b) First control experiment: (i) flowing 20 nm biotin-coated polystyrene, (ii) trapping event of 20 nm biotin-coated polystyrene particle and subsequently flowing saturated streptavidin, (iii) saturated streptavidin does not bind to the trapped 20 nm biotin-coated polystyrene particle. (c) Second control experiment: (i) flowing 20 nm non-functionalized polystyrene particles, (ii) trapping event of 20 nm polystyrene particle and then flowing streptavidin, (iii) streptavidin does not bind to the trapped 20 nm polystyrene particle. Reprinted from Ref. [148], Copyright 2013, OSA.

Single protein binding detection was further demonstrated using the streptavidin-biotin model with the same double nanohole aperture trap configuration [148]. In that work, as shown in Fig. 4.2, a double-syringe pump was used to deliver biotin-coated polystyrene particles to the double nanohole trapping site. When a biotin-coated polystyrene particle gets trapped between the cusps of the double nanohole aperture it dielectrically loads the region and causes an enhancement of the local optical field intensity and increased transmission. Once stable trapped of biotin coated

polystyrene particle was achieved, the double-syringe pump was used to flow in streptavidin solution to the trapping site, causing further dielectric loading to the double nanohole aperture region and consequently a higher optical transmission is obtained, Fig. 4.3(a). We used a moderate flow rate of 5 μL/min which enables fast enough delivery of streptavidin to the trapping site and at the same time does not wash away the trapped particle. The setup is designed such that delivery of streptavidin to the trapping site takes about 150 seconds from the time a successful trapping of biotin-coated PS particle is achieved. The delivery time of streptavidin to the trapping site of 150 seconds was related to the time for it to flow from the syringe to the trapping site at a flow rate of 5 μL/min. This indicates that a binding event occurs within a few seconds after the introduction of streptavidin to the trapping site, which is expected due to the high binding affinity of the streptavidin-biotin pair.

4.3.2 Control Experiments

To show clearly that we were actually observing specific streptavidin-biotin binding, we performed two separate control experiments using: 1) biotin-coated polystyrene particles were trapped and then streptavidin with the binding sites being blocked off by mixing it with excess biotin was flowed in, and 2) non-functionalized polystyrene particle trapping was achieved and then streptavidin was flowed in. As for the first control experiment (Fig. 4.3(b)), there is an increase in the optical transmission through the double nanohole aperture observed after flowing the 20 nm biotin-coated polystyrene particles indicating a successful trapping event of biotin-coated polystyrene particle. However, we have not observed any further increase in the optical transmission for the subsequent 25 minutes after flowing saturated streptavidin. And for the second control experiment (Fig. 4.3 (c)), we flowed in streptavidin (with the same concentration used in the main binding experiments) after successfully

achieving a trapping event of a 20 nm non-functionalized PS particle. Introduction of streptavidin to the trapping site did not cause any change in the optical transmission through the double nanohole aperture for the subsequent 25 minutes of achieving a stable trapping event of a non-functionalized polystyrene particle.

4.4 Label-free Free solution Single-Molecule Protein-Small Molecule Interaction Observed by Double Nanohole Trapping[2]

Protein-small molecule interactions (PSMIs) play an important role in biological functions. PSMIs are also of primary interest for the development of drugs, for example through inhibition of protein interactions. While many works have studied PSMIs, only few approaches exist that do not require tethering to a surface or labeling. Tethering to a surface has the disadvantages of using a binding site, restricting the protein motion with an anchor and introducing steric hindrance from the surface proximity. Labeling, such as fluorescent tags, present similar challenges, including using up a binding site and altering the natural state of the molecules of interest, but also add the complexity of using a label. Ideally, we would like to introduce new label-free, free-solution methods that work at the single molecule level, where it is possible to observe real time dynamics that are not obscured by an ensemble.

[2]The following section is adapted from: A. A. Al Balushi, and Reuven Gordon, Label-free free solution single-molecule protein-small molecule interaction observed by double nanohole plasmonic trapping, ACS Photonics 1(5), 389 - 393 (2014).

4.4.1 Experiment and Results

The double nanohole optical tweezer has been used to observe the real-time dynamic variation in PSMI interactions with the primary focus on the effect of single and multiple binding events on the dynamics of the protein in the trap [137, 149]. In those studies, four forms of streptavidin were considered: bare streptavidin, bare monovalent streptavidin, biotinylated streptavidin and biotinylated monovalent streptavidin. Time traces of the trapping events of each one of the four forms were compared, with the bare form of the streptavidin showing slower timescale dynamics as compared to the biotinylated forms of the protein. Fig. 4.4 shows the trapping dynamics of the streptavidin solution with and without the biotin in the double nanohole aperture.

4.4.2 Discussion

The change in the light transmitted through the double nanohole aperture can arise from differences in the size of the particle trapped, but also from changes in the particle shape or orientation, for example due to unfolding of proteins or conformal changes. These marked differences are not expected to arise from mass-loading since biotin has a mass $< 0.5\%$ the mass of streptavidin.

The difference between the bare and bound form of the protein manifests itself clearly when plotting the autocorrelation functions of the trapping events for the four different forms, Fig. 4.5. The bare form of streptavidin and monovalent streptavidin show fluctuations on the time scale of 600 ms and 200 ms, while the biotinylated form of streptavidin and monovalent streptavidin molecules show faster timescale dynamics with respective fluctuations on the time scale of about 20 ms and 8 ms; which imply that the bound form of the protein is subject to less conformal changes in the double nanohole trap. This is consistent with numerical studies on streptavidin which suggest that the four binding loops are highly mobile in the absent of biotin [150]; and is also

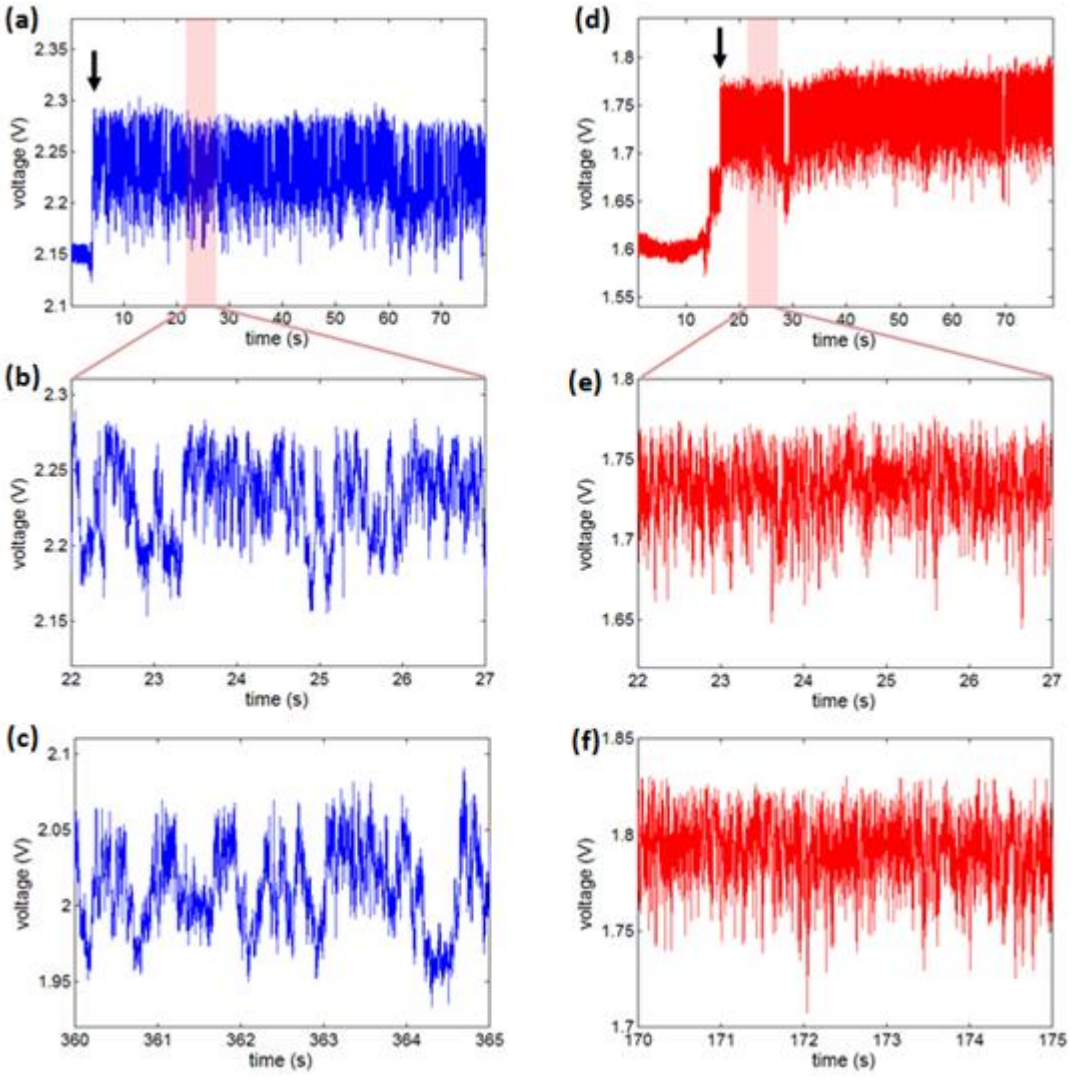

Figure 4.4: Trapping dynamics of streptavidin without and with biotin as measured from the APD voltage. (a) A time trace of a trapping event of a bare streptavidin molecule seen as an abrupt jump in the voltage level as denoted by the arrow. (b) Zoom-in of (a). (c) Repeat of (a) taken from a different sample on different day. (d) A time trace of a trapping event of a biotinylated streptavidin molecule seen as a discrete jump in the voltage level as indicated by the arrow. (e) Zoom-in of (d). (f) Repeat of (e) taken from a different sample on different day. Reprinted from ref. [137], Copyright 2014, American Chemical Society.

consistent with other reports in the literature which suggest that a small molecule binding can substantially alter the molecular dynamics of the protein [151].

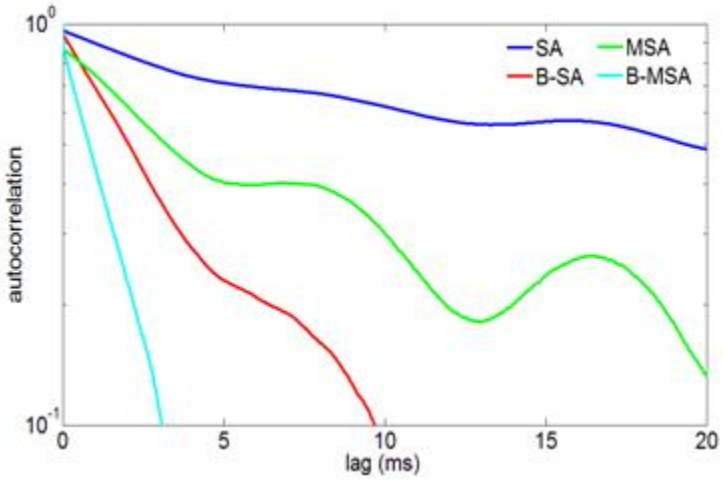

Figure 4.5: Autocorrelation of time traces of trapped streptavidin (SA), biotinylated streptavidin (B-SA), monovalent streptavidin (MSA) and biotinylated monovalent streptavidin (B-MSA). Reprinted from Ref. [149], Copyright 2014, OSA.

To further establish the applicability of our approach to distinguish between the bound and unbound forms of a protein, we used the cyclooxegenase 2-acetylsalicylic acid model. Fig. 4.6 shows the autocorrelation of the time traces of a trapped cyclooxegenase proteins with and without the small molecule binding. It is clear from figure that a bare form of the protein in the trap has a slower time variation as when compared with the bound protein which can be easily inferred by looking at the autocorrelation of the signals in Fig. 4.6. These results demonstrate that the double nanohole optical trap is not only able to differentiate between the bound and unbound forms of the protein, but also distinguish multiple binding events from a single binding event. The reader is referred to Appendix B for the full study.

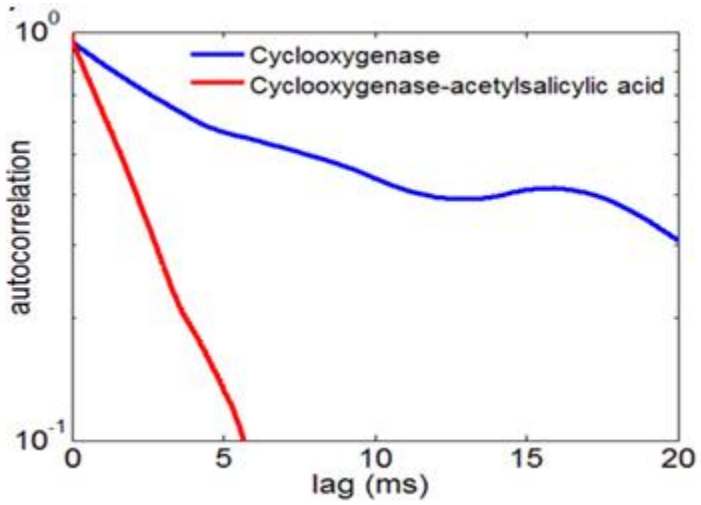

Figure 4.6: Autocorrelation of time traces of trapped cyclooxegenase 2 with and without small molecule binding. Reprinted from ref. [137], Copyright 2014, American Chemical Society.

4.5 A Label-Free Untethered Approach to Single-Molecule Protein Binding Kinetics[3]

Single molecule approaches provide rich real-time dynamics of molecular interactions that are not accessible to ensemble measurements. Previous single molecules studies have relied on labelling and tethering, which alters the natural state of the protein. Here we use the double nanohole optical tweezer approach to measure protein binding kinetics at the single molecule level in a label-free, free-solution (untethered) way [152]. Optical trapping using nanoapertures in metal films is an attractive method for detecting real-time interactions at the single-molecule level in a label-free, free-solution environment. For example, in the previous section have shown that the double nanohole tweezer system can detect the change in dynamics of a protein due to binding and thus presents the possibility of distinguishing between its bound and

[3]The following section is adapted from: A. A. Al Balushi, and Reuven Gordon, A label-free untethered approach to single-molecule protein binding kinetics, Nanoletters 14(10), 5787 - 5791 (2014).

unbound forms. A limiting factor that prevented us from studying the binding kinetics in our previous study was the high binding affinity of the complexes involved, requiring excessive observation times for single molecule studies. For example, the streptavidin-biotin complex has a dissociation constant, K_D, on the order of 10 fM. Our previous study focused on reporting on the ability of our double nanohole aperture trap to distinguish between the bound and unbound forms of proteins. We were not able to show binding dynamics in that work, which is of critical importance when assessing the interactions between proteins and small molecules. In addition, our previous approach was to use multiple steps to analyse the bound and unbound configurations separately, instead of looking at on-off binding rates in situ.

4.5.1 Experiment and Results

Here, we extend our study of PSMIs using the double nanohole optical trap by considering affinity pairs that have larger dissociation constants than those considered in our pervious study. We have chosen HSA protein in our current study because it is a well established protein for studying protein-ligand interactions and because it has dissociation constants in the M range. In addition, the binding kinetics of HSA have been characterized using a number of methods including nuclear magnetic resonance (NMR) [153], surface plasmon resonance [154] and fluorescence spectroscopy [155].

The interaction of HSA with a ligand can be described by

$$P + L \underset{k_d}{\overset{k_a}{\rightleftharpoons}} PL \tag{4.1}$$

where k_a and k_d are the association and dissociation rate constants, with the dissociation constant $K_D = k_d/k_a$. Fig. 4.7 (a) shows typical time evolutions of a trapped HSA-tolbutamide pair in the double nanohole aperture, with the data normalized to the mean value which is shown as a red dotted line in the figure. The mean value of

the time traces is used to define the threshold level between the bound and unbound states of the HSA molecule. The change in the light transmission through the double nanohole aperture for the HSA molecule with tolbutamide is due to conformal changes of the trapped protein with the protein in the bound state having higher polarizability and hence higher transmission through the aperture as compared with the protein in the unbound state.

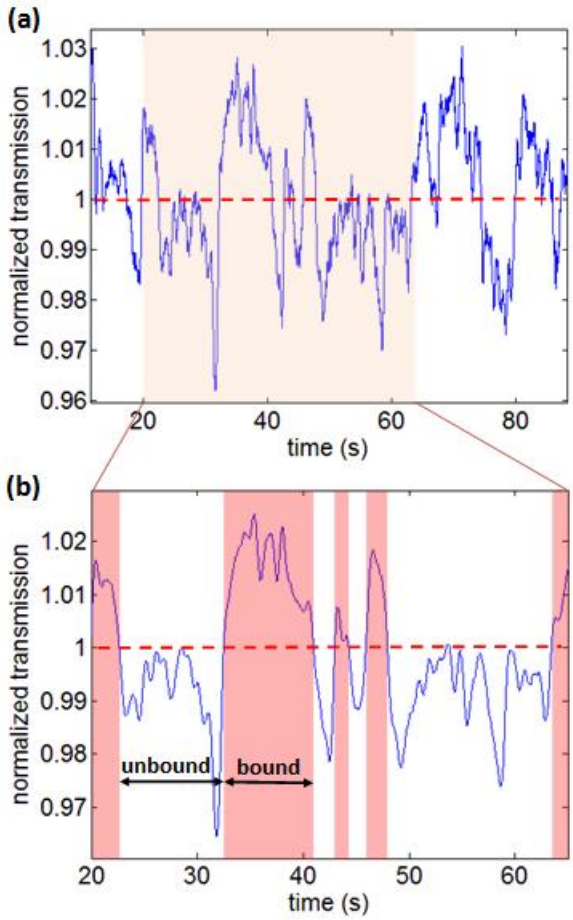

Figure 4.7: (a) Time trace of the interaction of HSA with tolbutamide in the DNH aperture. (b) Zoom-in of (a) showing the bound and unbound states of the HSA molecule with the high transmission regions denoted by pink corresponding to the bound state. Reprinted from ref. [152], Copyright 2014, American Chemical Society.

4.5.2 Discussion

From the time traces of the trapped HSA-tolbutamide pair in the double nanohole aperture histograms of the residence times of the HSA molecule were obtained by calculating the time it spends in the bound and unbound states as shown in Fig. 4.8.

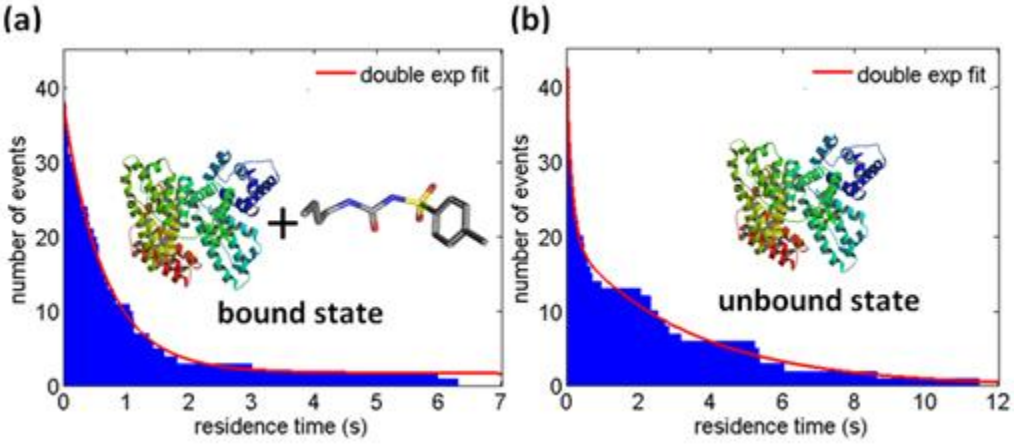

Figure 4.8: (a),(b) Histograms of residence times of HSA molecule in the bound and unbound states respectively as obtained from the signal of a trapped HSA molecule with tolbutamide in Fig. 4.7 (a). Reprinted from ref. [152], Copyright 2014, American Chemical Society.

The residence time of the HSA molecule in the bound state has a double exponential behavior with decay rate constants η_1 and η_2 of 1.317 s^{-1} and 0.1251 s^{-1}. The residence time of HSA molecule in the unbound state was also best fit by a double exponential equation having decay rate constants $\lambda_1 = 3.052$ s^{-1} and $\lambda_2 = 0.1018$ s^{-1}. The association and dissociation rate constants of the reaction as described in Eq. 4.1 are given by $k_a = \lambda_1/[L]$ and $k_d = \eta_1$; hence the dissociation constant, K_D, of the interaction is 13 μM, which falls within the 4.5 μM - 31.25 μM range reported in the literature [156–159].

We also considered the interaction of HSA with phenytoin and performed similar analysis to that used for tolbutamide. Fig. 4.9 (a) and (b) show the histograms of the residence times of the HSA molecule in the bound and unbound states with

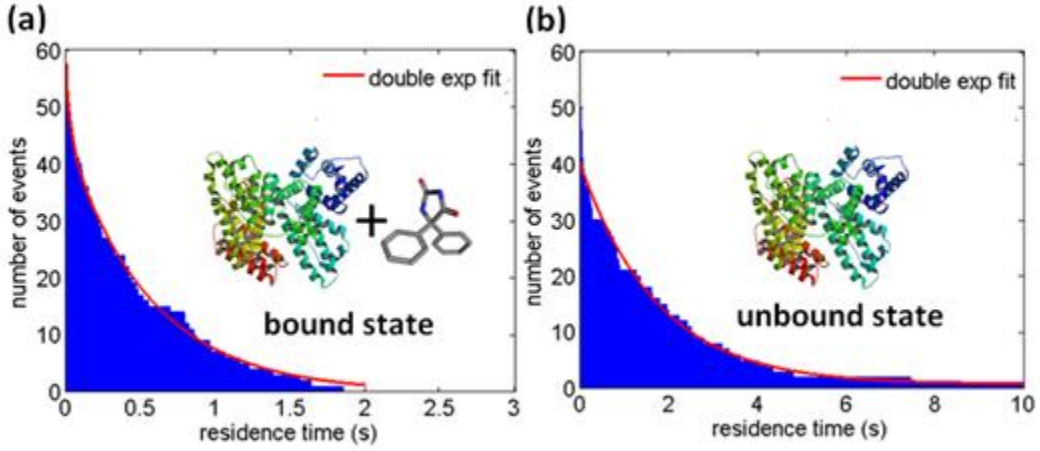

Figure 4.9: (a),(b) Histograms of residence times of HSA molecule in the bound and unbound states respectively as obtained from the signal of a trapped HSA molecule with phenytoin. Reprinted from ref. [152], Copyright 2014, American Chemical Society.

respective decay rate constants of $\eta_1 = 1.795\ \mathrm{s}^{-1}$ and $\lambda_1 = 0.5686\ \mathrm{s}^{-1}$; hence giving a dissociation constant $K_D = 94.7\ \mu$M. This dissociation constant falls within the 71.43 μM - 111 μM range reported in the literature [156–159].

One of the critical components in our analysis of binding kinetics is the determination of the threshold level between the bound and unbound states. In our current study the threshold level is determined by the mean value of the time traces of the HSA-ligand complex, i.e. the red dotted line, as seen in Fig. 4.7. We investigated the effect of varying the threshold level on the dissociation constant of the interaction of HSA protein with the ligand. Our results show that there is a range of threshold level values below and above the mean level in which K_D values remain within 20% of our reported values. However, the percentage variation in K_D increases dramatically as the threshold level is extended outside the tolerance window, Fig 4.10.

The high sensitivity of our system makes it possible to detect intermolecular interactions and characterize them by studying the effect they have on the transmitted light through the double nanohole aperture. Similar effects were not present when

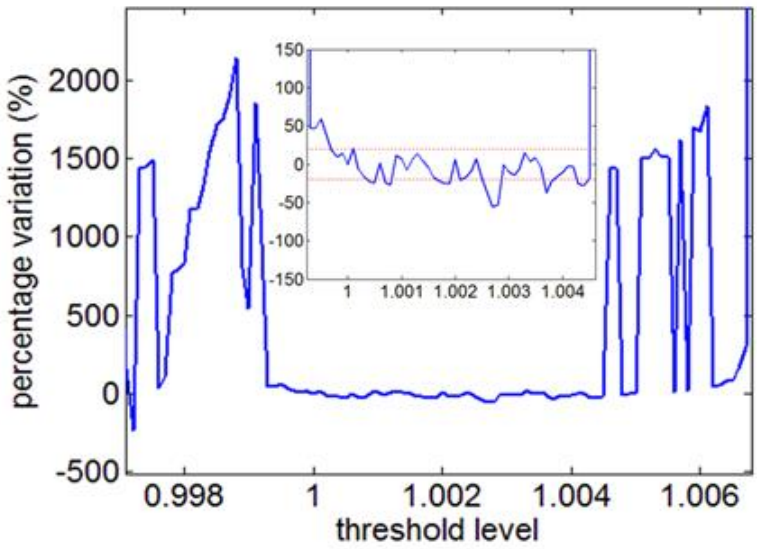

Figure 4.10: Dissociation constant percentage variation with varying threshold level for the interaction of HSA with tolbutamide, with the horizontal red dotted lines corresponding to ±20% percentage variation levels. Reprinted from ref. [152], Copyright 2014, American Chemical Society.

trapping a bare HSA molecule (Figure C1 (b)), which shows that the fluctuations present in the signal for the protein-ligand complexes were because of changes to the protein due to binding and unbinding events with the ligand. In addition, this variation in light transmission is not expected to be due to trapping of two HSA molecules in the double nanohole aperture because such events would induce a two-step increase in the transmission through the aperture, as we reported in an earlier study (Section 4.3) and as reported by other groups [112], and we have not observed such behavior in our current study. The reader is referred to Appendix C for the full study.

4.6 Summary

In summary, this chapter highlighted the work that has been carried out during the PhD period. It presented a way for detecting protein binding at the single molecule level by means of measuring the transmission through the double nanohole aperture.

In addition, it showed how the double nanohole aperture has been used to distinguish between the bound and unbound of proteins. Furthermore, it described a method for finding the binding kinetics of PSMIs using the double nanohole aperture tweezer system.

Chapter 5

Conclusions and Future Work

5.1 Thesis Conclusions

The aim of this thesis is to explore the applicability of the double nanohole optical trapping system to gain information about trapped molecules and study their interactions with other molecules. This thesis summarizes the work that has been carried out during my PhD period to achieving this goal.

First, the double nanohole aperture trap was integrated with microfluidic channels to allow for sequential delivery of solutions to the trapping site. In that experiment a double-syringe pump was used to deliver biotin-coated polystyrene particles to the double nanohole trapping site. Once stable trapped of biotin coated polystyrene particle was achieved, a double-syringe pump was used to flow in streptavidin solution to the trapping site. Streptavidin-biotin binding was detected by means of increased transmission through the double nanohole aperture. A number of control experiments were preformed to confirm that the increased transmission through the double nanohole is a consequence of protein binding.

In addition, the double nanohole optical tweezer has been used to observe the

real-time dynamic variation in PSMIs with the primary focus on the effect of single and multiple binding events on the dynamics of the protein in the trap. In those studies, four forms of streptavidin were considered: bare streptavidin, bare monovalent streptavidin, biotinylated streptavidin and biotinylated monovalent streptavidin. Time traces of the trapping events of each one of the four forms were compared, with the bound form of the protein showing faster timescale dynamics as compared to the unbound forms of the protein. To confirm these results further, the cyclooxygenase 2-acetylsalicylic acid system which revealed results consistent with those obtained using the streptavidin model. This work shows great potential for applications to screening small molecule drug candidates by monitoring their influence on proteins of interest, and for understanding the mechanisms of PSMIs.

Furthermore, the double nanohole aperture tweezer has been used to study the real-time binding kinetics of PSMIs and to determine their disassociation constants. The interaction of HSA with tolbutamide and phenytoin was considered in that study. The dissociation constants of the interaction of HSA with tolbutamide and phenytoin obtained. From the time traces of the trapped HSA complex in the double nanohole aperture we obtained histograms of the protein. Decay rate constants of the interaction were obtained from the histogram; and hence binding constants were calculated. Dissociation constants obtained using our techniques were in good agreement with the values reported in the literature. This shows that that binding events can be detected by identifying the conformal changes a ligand makes on the target protein molecule opening new windows for studying molecular interactions.

5.2 Future Work

This thesis has focused on exploring the scalability of the double nanohole optical tweezer system for single molecule studies. In addition, it looked at different statistical analysis techniques that can be applied to the double nanohole aperture trap to gain information about trapped molecules and study their interactions with other molecules. Results that have been presented in this thesis lay down the foundations for some interesting projects that can be executed in the future.

First, it would be interesting to see how small molecule binding affects the vibrational modes of a protein. This could also be taken further by looking at how vibrational modes differ for a wild and mutant type of a protein which would help in cancer diagnosis.

Second, although our binding kinetics study only considered the interactions of affinity pairs which have dissociation constants in the μM range, it would be interesting to study a broader range of affinity pairs where the effects of multiple binding sites are taken into account and higher order transitions are considered. This would test the sensitivity versatility of our double nanohole trapping system.

Third, real-time dynamics work on bound and unbound proteins (Section 4.4) can be extended further by considering a flow-channel setup, similar to the one used for single protein binding detection (Section 4.3). In this scenario, it would be possible to first trap the vacant streptavidin and then introduce biotin into the channel. The goal would be to determine if the binding to the four binding sites in streptavidin can be observed individually. Obviously, it is of great interest to see if these results can be further extended to other PSMI systems that play a role in biological function.

Bibliography

[1] Arthur Ashkin, JM Dziedzic, JE Bjorkholm, and Steven Chu. Observation of a single-beam gradient force optical trap for dielectric particles. *Optics letters*, 11(5):288–290, 1986.

[2] Kishan Dholakia, Peter Reece, and Min Gu. Optical micromanipulation. *Chem. Soc. Rev.*, 37:42–55, 2008.

[3] Alexander Rohrbach and Ernst HK Stelzer. Optical trapping of dielectric particles in arbitrary fields. *JOSA A*, 18(4):839–853, 2001.

[4] Shida Tan, Herman A Lopez, Colin W Cai, and Yuegang Zhang. Optical trapping of single-walled carbon nanotubes. *Nano Letters*, 4(8):1415–1419, 2004.

[5] OM Marago, PH Jones, F Bonaccorso, V Scardaci, PG Gucciardi, AG Rozhin, and AC Ferrari. Femtonewton force sensing with optically trapped nanotubes. *Nano letters*, 8(10):3211–3216, 2008.

[6] OM Marago, PG Gucciardi, F Bonaccorso, G Calogero, V Scardaci, AG Rozhin, AC Ferrari, PH Jones, R Saija, F Borghese, et al. Optical trapping of carbon nanotubes. *Physica E: Low-dimensional Systems and Nanostructures*, 40(7):2347–2351, 2008.

[7] Thomas Rodgers, Satoru Shoji, Zouheir Sekkat, and Satoshi Kawata. Selective aggregation of single-walled carbon nanotubes using the large optical field gradient of a focused laser beam. *Physical review letters*, 101(12):127402, 2008.

[8] Peter J Pauzauskie, Arash Jamshidi, Justin K Valley, Joe H Satcher Jr, and Ming C Wu. Parallel trapping of multiwalled carbon nanotubes with optoelectronic tweezers. *Applied physics letters*, 95(11):113104, 2009.

[9] Onofrio M Maragó, Francesco Bonaccorso, Rosalba Saija, Giulia Privitera, Pietro G Gucciardi, Maria Antonia Iatì, Giuseppe Calogero, Philip H Jones, Ferdinando Borghese, Paolo Denti, et al. Brownian motion of graphene. *ACS nano*, 4(12):7515–7523, 2010.

[10] Christopher W Twombly, Julian S Evans, and Ivan I Smalyukh. Optical manipulation of self-aligned graphene flakes in liquid crystals. *Optics express*, 21(1):1324–1334, 2013.

[11] Michael Geiselmann, Mathieu L Juan, Jan Renger, Jana M Say, Louise J Brown, F Javier García De Abajo, Frank Koppens, and Romain Quidant. Three-dimensional optical manipulation of a single electron spin. *Nature nanotechnology*, 8(3):175–179, 2013.

[12] Peter J Reece, Wen Jun Toe, Fan Wang, Suriati Paiman, Qiang Gao, H Hoe Tan, and Chennupati Jagadish. Characterization of semiconductor nanowires using optical tweezers. *Nano letters*, 11(6):2375–2381, 2011.

[13] Ritesh Agarwal, Kosta Ladavac, Yael Roichman, Guihua Yu, Charles Lieber, and David Grier. Manipulation and assembly of nanowires with holographic optical traps. *Optics Express*, 13(22):8906–8912, 2005.

[14] Peter J Pauzauskie, Aleksandra Radenovic, Eliane Trepagnier, Hari Shroff, Peidong Yang, and Jan Liphardt. Optical trapping and integration of semiconductor nanowire assemblies in water. *Nature materials*, 5(2):97–101, 2006.

[15] Yuri Nakayama, Peter J Pauzauskie, Aleksandra Radenovic, Robert M Onorato, Richard J Saykally, Jan Liphardt, and Peidong Yang. Tunable nanowire nonlinear optical probe. *Nature*, 447(7148):1098–1101, 2007.

[16] Peter J Reece, Suriati Paiman, Osama Abdul-Nabi, Qiang Gao, Michael Gal, H Hoe Tan, and C Jagadish. Combined optical trapping and microphotoluminescence of single inp nanowires. *Applied Physics Letters*, 95(10):101109, 2009.

[17] Alessia Irrera, Pietro Artoni, Rosalba Saija, Pietro G Gucciardi, Maria Antonia Iatì, Ferdinando Borghese, Paolo Denti, Fabio Iacona, Francesco Priolo, and Onofrio M Marago. Size-scaling in optical trapping of silicon nanowires. *Nano letters*, 11(11):4879–4884, 2011.

[18] F Dutto, C Raillon, K Schenk, and A Radenovic. Nonlinear optical response in single alkaline niobate nanowires. *Nano letters*, 11(6):2517–2521, 2011.

[19] Fan Wang, Wen Jun Toe, Woei Ming Lee, David McGloin, Qiang Gao, Hark Hoe Tan, Chennupati Jagadish, and Peter J Reece. Resolving stable axial trapping points of nanowires in an optical tweezers using photoluminescence mapping. *Nano letters*, 13(3):1185–1191, 2013.

[20] Karel Svoboda and Steven M Block. Optical trapping of metallic rayleigh particles. *Optics letters*, 19(13):930–932, 1994.

[21] Matthew Pelton, Mingzhao Liu, Hee Y Kim, Glenna Smith, Philippe Guyot-Sionnest, and Norbert F Scherer. Optical trapping and alignment of single gold nanorods by using plasmon resonances. *Optics letters*, 31(13):2075–2077, 2006.

[22] KC Toussaint, M Liu, M Pelton, J Pesic, MJ Guffey, P Guyot-Sionnest, and NF Scherer. Plasmon resonance-based optical trapping of single and multiple au nanoparticles. *Optics express*, 15(19):12017–12029, 2007.

[23] Christine Selhuber-Unkel, Inga Zins, Olaf Schubert, Carsten Sonnichsen, and Lene B Oddershede. Quantitative optical trapping of single gold nanorods. *Nano letters*, 8(9):2998–3003, 2008.

[24] Maria Dienerowitz, Michael Mazilu, Peter J Reece, Thomas F Krauss, and Kishan Dholakia. Optical vortex trap for resonant confinement of metal nanoparticles. *Optics Express*, 16(7):4991–4999, 2008.

[25] Lana Bosanac, Thomas Aabo, Poul M Bendix, and Lene B Oddershede. Efficient optical trapping and visualization of silver nanoparticles. *Nano letters*, 8(5):1486–1491, 2008.

[26] PH Jones, F Palmisano, F Bonaccorso, PG Gucciardi, G Calogero, AC Ferrari, and OM Marago. Rotation detection in light-driven nanorotors. *ACS nano*, 3(10):3077–3084, 2009.

[27] Lianming Tong, Vladimir D Miljkovic, and Mikael Kall. Alignment, rotation, and spinning of single plasmonic nanoparticles and nanowires using polarization dependent optical forces. *Nano letters*, 10(1):268–273, 2009.

[28] Lianming Tong, Vladimir D Miljkovic, Peter Johansson, and Mikael Kall. Plasmon hybridization reveals the interaction between individual colloidal gold

nanoparticles confined in an optical potential well. *Nano letters*, 11(11):4505–4508, 2010.

[29] Elena Messina, Emanuele Cavallaro, Adriano Cacciola, Maria Antonia Iatì, Pietro G Gucciardi, Ferdinando Borghese, Paolo Denti, Rosalba Saija, Giuseppe Compagnini, Moreno Meneghetti, et al. Plasmon-enhanced optical trapping of gold nanoaggregates with selected optical properties. *ACS nano*, 5(2):905–913, 2011.

[30] M Ploschner, T Cizmar, M Mazilu, A Di Falco, and K Dholakia. Bidirectional optical sorting of gold nanoparticles. *Nano letters*, 12(4):1923–1927, 2012.

[31] Yuanjie Pang and Reuven Gordon. Optical trapping of a single protein. *Nano letters*, 12(1):402–406, 2011.

[32] Abhay Kotnala and Reuven Gordon. Double nanohole optical tweezers visualize protein p53 suppressing unzipping of single dna-hairpins. *Biomedical optics express*, 5(6):1886–1894, 2014.

[33] Abhay Kotnala, Damon DePaoli, and Reuven Gordon. Sensing nanoparticles using a double nanohole optical trap. *Lab on a Chip*, 13(20):4142–4146, 2013.

[34] Skyler Wheaton, Ryan M Gelfand, and Reuven Gordon. Probing the raman-active acoustic vibrations of nanoparticles with extraordinary spectral resolution. *Nature Photonics*, 9(1):68–72, 2015.

[35] Onofrio M Maragò, Philip H Jones, Pietro G Gucciardi, Giovanni Volpe, and Andrea C Ferrari. Optical trapping and manipulation of nanostructures. *Nature nanotechnology*, 8(11):807–819, 2013.

[36] JD Jackson. Classical electrodynamics. *Wiley, New York*, 1998.

[37] PW Smith, Arthur Ashkin, and WJ Tomlinson. Four-wave mixing in an artificial kerr medium. *Optics letters*, 6(6):284–286, 1981.

[38] Arthur Ashkin, JM Dziedzic, and PW Smith. Continuous-wave self-focusing and self-trapping of light in artificial kerr media. *Optics letters*, 7(6):276–278, 1982.

[39] Faegheh Hajizadeh and S Nader S Reihani. Optimized optical trapping of gold nanoparticles. *Optics express*, 18(2):551–559, 2010.

[40] Arthur Ashkin and JM Dziedzic. Optical trapping and manipulation of viruses and bacteria. *Science*, 235(4795):1517–1520, 1987.

[41] Timo A Nieminen, Gregor Knöner, Norman R Heckenberg, and Halina Rubinsztein-Dunlop. Physics of optical tweezers. *Methods in cell biology*, 82:207–236, 2007.

[42] Tongcang Li, Simon Kheifets, David Medellin, and Mark G Raizen. Measurement of the instantaneous velocity of a brownian particle. *Science*, 328(5986):1673–1675, 2010.

[43] Eun-Soo Kwak, Tiberiu-Dan Onuta, Dragos Amarie, Radislav Potyrailo, Barry Stein, Stephen C Jacobson, WL Schaich, and Bogdan Dragnea. Optical trapping with integrated near-field apertures. *The Journal of Physical Chemistry B*, 108(36):13607–13612, 2004.

[44] Lina Huang and Olivier JF Martin. Reversal of the optical force in a plasmonic trap. *Optics letters*, 33(24):3001–3003, 2008.

[45] M Nieto-Vesperinas, PC Chaumet, and A Rahmani. Near-field photonic forces. *PHILOSOPHICAL TRANSACTIONS-ROYAL SOCIETY OF LONDON SE-*

RIES A MATHEMATICAL PHYSICAL AND ENGINEERING SCIENCES, pages 719–738, 2004.

[46] K Okamoto and S Kawata. Radiation force exerted on subwavelength particles near a nanoaperture. *Physical review letters*, 83(22):4534, 1999.

[47] Lukas Novotny, Randy X Bian, and X Sunney Xie. Theory of nanometric optical tweezers. *Physical Review Letters*, 79(4):645, 1997.

[48] Allen HJ Yang, Sean D Moore, Bradley S Schmidt, Matthew Klug, Michal Lipson, and David Erickson. Optical manipulation of nanoparticles and biomolecules in sub-wavelength slot waveguides. *Nature*, 457(7225):71–75, 2009.

[49] Alexander Ohlinger, Spas Nedev, Andrey A Lutich, and Jochen Feldmann. Optothermal escape of plasmonically coupled silver nanoparticles from a three-dimensional optical trap. *Nano letters*, 11(4):1770–1774, 2011.

[50] Maurizio Righini, Anna S Zelenina, Christian Girard, and Romain Quidant. Parallel and selective trapping in a patterned plasmonic landscape. *Nature Physics*, 3(7):477–480, 2007.

[51] Maurizio Righini, Giovanni Volpe, Christian Girard, Dmitri Petrov, and Romain Quidant. Surface plasmon optical tweezers: tunable optical manipulation in the femtonewton range. *Physical review letters*, 100(18):186804, 2008.

[52] Yuanjie Pang and Reuven Gordon. Nanophotonics using a subwavelength aperture in a metal film. *Nanotechnology Reviews*, 1(4):339–362, 2012.

[53] Yuanjie Pang. *Nanophotonics with subwavelength apertures: theories and applications.* PhD thesis, University of Victoria, 2012.

[54] V Garcés-Chávez, R Quidant, PJ Reece, G Badenes, L Torner, and K Dholakia. Extended organization of colloidal microparticles by surface plasmon polariton excitation. *Physical Review B*, 73(8):085417, 2006.

[55] Martin Ploschner, Michael Mazilu, Thomas F Krauss, and Kishan Dholakia. Optical forces near a nanoantenna. *Journal of Nanophotonics*, 4(1):041570–041570, 2010.

[56] Yeonee Seol, Amanda E Carpenter, and Thomas T Perkins. Gold nanoparticles: enhanced optical trapping and sensitivity coupled with significant heating. *Optics letters*, 31(16):2429–2431, 2006.

[57] Poul M Bendix, S Nader S Reihani, and Lene B Oddershede. Direct measurements of heating by electromagnetically trapped gold nanoparticles on supported lipid bilayers. *ACS nano*, 4(4):2256–2262, 2010.

[58] Stefan Duhr and Dieter Braun. Why molecules move along a temperature gradient. *Proceedings of the National Academy of Sciences*, 103(52):19678–19682, 2006.

[59] Changjun Min, Zhe Shen, Junfeng Shen, Yuquan Zhang, Hui Fang, Guanghui Yuan, Luping Du, Siwei Zhu, Ting Lei, and Xiaocong Yuan. Focused plasmonic trapping of metallic particles. *Nature communications*, 4, 2013.

[60] Anders Kyrsting, Poul M Bendix, Dimitrios G Stamou, and Lene B Oddershede. Heat profiling of three-dimensionally optically trapped gold nanoparticles using vesicle cargo release. *Nano letters*, 11(2):888–892, 2010.

[61] Jon S Donner, Guillaume Baffou, David McCloskey, and Romain Quidant. Plasmon-assisted optofluidics. *Acs nano*, 5(7):5457–5462, 2011.

[62] Nathan C Lindquist, Jincy Jose, Sudhir Cherukulappurath, Xiaoshu Chen, Timothy W Johnson, and Sang-Hyun Oh. Tip-based plasmonics: squeezing light with metallic nanoprobes. *Laser & Photonics Reviews*, 7(4):453–477, 2013.

[63] Amr AE Saleh and Jennifer A Dionne. Toward efficient optical trapping of sub-10-nm particles with coaxial plasmonic apertures. *Nano letters*, 12(11):5581–5586, 2012.

[64] Yih-Fan Chen, Xavier Serey, Rupa Sarkar, Peng Chen, and David Erickson. Controlled photonic manipulation of proteins and other nanomaterials. *Nano letters*, 12(3):1633–1637, 2012.

[65] Shiyun Lin and Kenneth B Crozier. Trapping-assisted sensing of particles and proteins using on-chip optical microcavities. *ACS nano*, 7(2):1725–1730, 2013.

[66] Kai Wang and Kenneth B Crozier. Plasmonic trapping with a gold nanopillar. *ChemPhysChem*, 13(11):2639–2648, 2012.

[67] Kai Wang, Ethan Schonbrun, Paul Steinvurzel, and Kenneth B Crozier. Trapping and rotating nanoparticles using a plasmonic nano-tweezer with an integrated heat sink. *Nature communications*, 2:469, 2011.

[68] Pavel N Melentiev, Anton E Afanasiev, Artur A Kuzin, Andrey S Baturin, and Victor I Balykin. Giant optical nonlinearity of a single plasmonic nanostructure. *Optics express*, 21(12):13896–13905, 2013.

[69] A Ashkin and JM Dziedzic. Feedback stabilization of optically levitated particles. *Applied Physics Letters*, 30(4):202–204, 1977.

[70] Robert M Simmons, Jeffrey T Finer, Steven Chu, and James A Spudich. Quantitative measurements of force and displacement using an optical trap. *Biophysical Journal*, 70(4):1813, 1996.

[71] Anders E Wallin, Heikki Ojala, Edward Hæggström, and Roman Tuma. Stiffer optical tweezers through real-time feedback control. *Applied Physics Letters*, 92(22):224104, 2008.

[72] Mathieu L Juan, Reuven Gordon, Yuanjie Pang, Fatima Eftekhari, and Romain Quidant. Self-induced back-action optical trapping of dielectric nanoparticles. *Nature Physics*, 5(12):915–919, 2009.

[73] Allen HJ Yang, Tadsanapan Lerdsuchatawanich, and David Erickson. Forces and transport velocities for a particle in a slot waveguide. *Nano letters*, 9(3):1182–1188, 2009.

[74] RF Marchington, M Mazilu, S Kuriakose, V Garcés-Chávez, PJ Reece, TF Krauss, M Gu, and K Dholakia. Optical deflection and sorting of microparticles in a near-field optical geometry. *Optics express*, 16(6):3712–3726, 2008.

[75] Keir C Neuman and Steven M Block. Optical trapping. *Review of scientific instruments*, 75(9):2787–2809, 2004.

[76] Patrick C Chaumet, Adel Rahmani, and Manuel Nieto-Vesperinas. Optical trapping and manipulation of nano-objects with an apertureless probe. *Physical review letters*, 88(12):123601, 2002.

[77] Mathieu L Juan, Maurizio Righini, and Romain Quidant. Plasmon nano-optical tweezers. *Nature Photonics*, 5(6):349–356, 2011.

[78] Pau Mestres, Johann Berthelot, and Romain Quidant. Unraveling the optomechanical nature of plasmonic trapping. *arXiv preprint arXiv:1511.05310*, 2015.

[79] Poul Martin Hansen, Vikram Kjøller Bhatia, Niels Harrit, and Lene Oddershede. Expanding the optical trapping range of gold nanoparticles. *Nano letters*, 5(10):1937–1942, 2005.

[80] Liselotte Jauffred and Lene B Oddershede. Two-photon quantum dot excitation during optical trapping. *Nano letters*, 10(5):1927–1930, 2010.

[81] Stefan Enoch, Romain Quidant, and Gonçal Badenes. Optical sensing based on plasmon coupling in nanoparticle arrays. *Optics express*, 12(15):3422–3427, 2004.

[82] Prashant K Jain and Mostafa A El-Sayed. Noble metal nanoparticle pairs: effect of medium for enhanced nanosensing. *Nano letters*, 8(12):4347–4352, 2008.

[83] N Verellen et al. Symmetry breaking in a plasmonic metamaterial at optical wavelength. *Nano Lett*, 9:1663–1667, 2009.

[84] Na Liu, Thomas Weiss, Martin Mesch, Lutz Langguth, Ulrike Eigenthaler, Michael Hirscher, Carsten Sonnichsen, and Harald Giessen. Planar metamaterial analogue of electromagnetically induced transparency for plasmonic sensing. *Nano letters*, 10(4):1103–1107, 2009.

[85] Andrey B Evlyukhin, Sergey I Bozhevolnyi, Anders Pors, Michael G Nielsen, Ilya P Radko, Morten Willatzen, and Ole Albrektsen. Detuned electrical dipoles for plasmonic sensing. *Nano letters*, 10(11):4571–4577, 2010.

[86] CS Adams and E Riis. Laser cooling and trapping of neutral atoms. *Progress in quantum electronics*, 21(1):1–79, 1997.

[87] PWH Pinkse, T Fischer, P Maunz, and G Rempe. Trapping an atom with single photons. *Nature*, 404(6776):365–368, 2000.

[88] Takuya Iida and Hajime Ishihara. Theoretical study of the optical manipulation of semiconductor nanoparticles under an excitonic resonance condition. *Physical review letters*, 90(5):057403, 2003.

[89] M Righini, P Ghenuche, S Cherukulappurath, Viktor Myroshnychenko, Francisco Javier Garcia de Abajo, and Romain Quidant. Nano-optical trapping of rayleigh particles and escherichia coli bacteria with resonant optical antennas. *Nano letters*, 9(10):3387–3391, 2009.

[90] Weihua Zhang, Lina Huang, Christian Santschi, and Olivier JF Martin. Trapping and sensing 10 nm metal nanoparticles using plasmonic dipole antennas. *Nano letters*, 10(3):1006–1011, 2010.

[91] Brian J Roxworthy, Kaspar D Ko, Anil Kumar, Kin Hung Fung, Edmond KC Chow, Gang Logan Liu, Nicholas X Fang, and Kimani C Toussaint Jr. Application of plasmonic bowtie nanoantenna arrays for optical trapping, stacking, and sorting. *Nano letters*, 12(2):796–801, 2012.

[92] Yasuyuki Tsuboi, Tatsuya Shoji, Noboru Kitamura, Mai Takase, Kei Murakoshi, Yoshihiko Mizumoto, and Hajime Ishihara. Optical trapping of quantum dots based on gap-mode-excitation of localized surface plasmon. *The Journal of Physical Chemistry Letters*, 1(15):2327–2333, 2010.

[93] Tatsuya Shoji and Yasuyuki Tsuboi. Plasmonic optical tweezers toward molecular manipulation: Tailoring plasmonic nanostructure, light source, and resonant trapping. *The journal of physical chemistry letters*, 5(17):2957–2967, 2014.

[94] S Arnold, D Keng, SI Shopova, S Holler, W Zurawsky, and F Vollmer. Whispering gallery mode carousel–a photonic mechanism for enhanced nanoparticle detection in biosensing. *Optics Express*, 17(8):6230–6238, 2009.

[95] Juejun Hu, Shiyun Lin, Lionel C Kimerling, and Kenneth Crozier. Optical trapping of dielectric nanoparticles in resonant cavities. *Physical Review A*, 82(5):053819, 2010.

[96] Michael Barth and Oliver Benson. Manipulation of dielectric particles using photonic crystal cavities. *Applied physics letters*, 89(25):253114, 2006.

[97] Shiyun Lin, Ethan Schonbrun, and Kenneth Crozier. Optical manipulation with planar silicon microring resonators. *Nano letters*, 10(7):2408–2411, 2010.

[98] Sudeep Mandal, Xavier Serey, and David Erickson. Nanomanipulation using silicon photonic crystal resonators. *Nano letters*, 10(1):99–104, 2009.

[99] Frank Vollmer and Stephen Arnold. Whispering-gallery-mode biosensing: label-free detection down to single molecules. *Nature methods*, 5(7):591–596, 2008.

[100] F Vollmer, S Arnold, and D Keng. Single virus detection from the reactive shift of a whispering-gallery mode. *Proceedings of the National Academy of Sciences*, 105(52):20701–20704, 2008.

[101] EX Jin and X Xu. Plasmonic effects in near-field optical transmission enhancement through a single bowtie-shaped aperture. *Applied Physics B*, 84(1-2):3–9, 2006.

[102] Liang Wang, Sreemanth M Uppuluri, Eric X Jin, and Xianfan Xu. Nanolithography using high transmission nanoscale bowtie apertures. *Nano letters*, 6(3):361–364, 2006.

[103] Bin Ai, Ye Yu, Helmuth Möhwald, and Gang Zhang. Novel 3d au nanohole arrays with outstanding optical properties. *Nanotechnology*, 24(3):035303, 2012.

[104] Bin Ai, Limin Wang, Helmuth Möhwald, Ye Yu, and Gang Zhang. Asymmetric half-cone/nanohole array films with structural and directional reshaping of extraordinary optical transmission. *Nanoscale*, 6(15):8997–9005, 2014.

[105] Antoine Lesuffleur, L Kiran Swaroop Kumar, and Reuven Gordon. Enhanced second harmonic generation from nanoscale double-hole arrays in a gold film. *Applied physics letters*, 88(26):261104, 2006.

[106] A Lesuffleur, LKS Kumar, and R Gordon. Apex-enhanced second-harmonic generation by using double-hole arrays in a gold film. *Physical Review B*, 75(4):045423, 2007.

[107] A Lesuffleur, LKS Kumar, AG Brolo, KL Kavanagh, and R Gordon. Apex-enhanced raman spectroscopy using double-hole arrays in a gold film. *The Journal of Physical Chemistry C*, 111(6):2347–2350, 2007.

[108] L Kumar and Reuven Gordon. Overlapping double-hole nanostructure in a metal film for localized field enhancement. *Selected Topics in Quantum Electronics, IEEE Journal of*, 12(6):1228–1232, 2006.

[109] Tiberiu-Dan Onuta, Matthias Waegele, Christopher C DuFort, William L Schaich, and Bogdan Dragnea. Optical field enhancement at cusps between adjacent nanoapertures. *Nano letters*, 7(3):557–564, 2007.

[110] DE Grupp, HJ Lezec, TW Ebbesen, KM Pellerin, and Tineke Thio. Crucial role of metal surface in enhanced transmission through subwavelength apertures. *Applied Physics Letters*, 77(11):1569–1571, 2000.

[111] Reuven Gordon and Alexandre G Brolo. Increased cut-off wavelength for a subwavelength hole in a real metal. *Optics Express*, 13(6):1933–1938, 2005.

[112] Chang Chen, Mathieu L Juan, Yi Li, Guido Maes, Gustaaf Borghs, Pol Van Dorpe, and Romain Quidant. Enhanced optical trapping and arrangement of nano-objects in a plasmonic nanocavity. *Nano letters*, 12(1):125–132, 2011.

[113] Yuanjie Pang and Reuven Gordon. Optical trapping of 12 nm dielectric spheres using double-nanoholes in a gold film. *Nano letters*, 11(9):3763–3767, 2011.

[114] J. Berthelot, S. S. Acimovic, M. L. Juan, M. P. Kreuzer, J. Renger, and R. Quidant. Three-dimensional manipulation with scanning near-field optical nanotweezers. *Nat Nano*, 9(4):295–299, Apr 2014.

[115] Raju Regmi, Ahmed A Al Balushi, Hervé Rigneault, Reuven Gordon, and Jérôme Wenger. Nanoscale volume confinement and fluorescence enhancement with double nanohole aperture. *Scientific reports*, 5, 2015.

[116] Yuanyuan Chen, Abhay Kotnala, Li Yu, Jiasen Zhang, and Reuven Gordon. Wedge and gap plasmonic resonances in double nanoholes. *Optics express*, 23(23):30227–30236, 2015.

[117] Hongcang Guo, Todd P Meyrath, Thomas Zentgraf, Na Liu, Liwei Fu, Heinz Schweizer, and Harald Giessen. Optical resonances of bowtie slot antennas and their geometry and material dependence. *Optics express*, 16(11):7756–7766, 2008.

[118] I Abdoulkader Ibrahim, M Mivelle, T Grosjean, J-T Allegre, GW Burr, and FI Baida. Bowtie-shaped nanoaperture: a modal study. *Optics letters*, 35(14):2448–2450, 2010.

[119] Eyal Feigenbaum and Meir Orenstein. Nano plasmon polariton modes of a wedge cross section metal waveguide. *Optics express*, 14(19):8779–8784, 2006.

[120] Steven Jones, Ahmed A Al Balushi, and Reuven Gordon. Raman spectroscopy of single nanoparticles in a double-nanohole optical tweezer system. *Journal of Optics*, 17(10):102001, 2015.

[121] Abhay Kotnala, Skyler Wheaton, and Reuven Gordon. Playing the notes of dna with light: extremely high frequency nanomechanical oscillations. *Nanoscale*, 7(6):2295–2300, 2015.

[122] Hideki Taguchi, Taro Ueno, Hisashi Tadakuma, Masasuke Yoshida, and Takashi Funatsu. Single-molecule observation of protein–protein interactions in the chaperonin system. *Nature biotechnology*, 19(9):861–865, 2001.

[123] Mark P Elenko, Jack W Szostak, and Antoine M van Oijen. Single-molecule imaging of an in vitro-evolved rna aptamer reveals homogeneous ligand binding kinetics. *Journal of the American Chemical Society*, 131(29):9866–9867, 2009.

[124] Ciro Cecconi, Elizabeth A Shank, Carlos Bustamante, and Susan Marqusee. Direct observation of the three-state folding of a single protein molecule. *Science*, 309(5743):2057–2060, 2005.

[125] Alessandro Borgia, Philip M Williams, and Jane Clarke. Single-molecule studies of protein folding. *Annu. Rev. Biochem.*, 77:101–125, 2008.

[126] Iddo Heller, Gerrit Sitters, Onno D Broekmans, Géraldine Farge, Carolin Menges, Wolfgang Wende, Stefan W Hell, Erwin JG Peterman, and Gijs JL Wuite. Sted nanoscopy combined with optical tweezers reveals protein dynamics on densely covered dna. *nAture methods*, 10(9):910–916, 2013.

[127] Meindert A van Dijk, Lukas C Kapitein, Joost van Mameren, Christoph F Schmidt, and Erwin JG Peterman. Combining optical trapping and single-

molecule fluorescence spectroscopy: enhanced photobleaching of fluorophores. *The Journal of Physical Chemistry B*, 108(20):6479–6484, 2004.

[128] Christopher B Fox, Joshua R Wayment, Grant A Myers, Scott K Endicott, and Joel M Harris. Single-molecule fluorescence imaging of peptide binding to supported lipid bilayers. *Analytical chemistry*, 81(13):5130–5138, 2009.

[129] Yasmina SN Day, Cheryl L Baird, Rebecca L Rich, and David G Myszka. Direct comparison of binding equilibrium, thermodynamic, and rate constants determined by surface-and solution-based biophysical methods. *Protein Science*, 11(5):1017–1025, 2002.

[130] Adessamad Ababou and John E Ladbury. Survey of the year 2005: literature on applications of isothermal titration calorimetry. *Journal of Molecular Recognition*, 20(1):4–14, 2007.

[131] Adrián Velázquez Campoy and Ernesto Freire. Itc in the post-genomic era? priceless. *Biophysical chemistry*, 115(2):115–124, 2005.

[132] Stephanie Leavitt and Ernesto Freire. Direct measurement of protein binding energetics by isothermal titration calorimetry. *Current opinion in structural biology*, 11(5):560–566, 2001.

[133] Francisco E Torres, Peter Kuhn, Dirk De Bruyker, Alan G Bell, Michal V Wolkin, Eric Peeters, James R Williamson, Gregory B Anderson, Gregory P Schmitz, Michael I Recht, et al. Enthalpy arrays. *Proceedings of the National Academy of Sciences of the United States of America*, 101(26):9517–9522, 2004.

[134] Darryl J Bornhop, Joey C Latham, Amanda Kussrow, Dmitry A Markov, Richard D Jones, and Henrik S Sørensen. Free-solution, label-free molecular

interactions studied by back-scattering interferometry. *science*, 317(5845):1732–1736, 2007.

[135] WE Moerner. A dozen years of single-molecule spectroscopy in physics, chemistry, and biophysics. *The Journal of Physical Chemistry B*, 106(5):910–927, 2002.

[136] Guillaume AT Chansin, Rafael Mulero, Jongin Hong, Min Jun Kim, Andrew J Demello, and Joshua B Edel. Single-molecule spectroscopy using nanoporous membranes. *Nano letters*, 7(9):2901–2906, 2007.

[137] Ahmed A Al Balushi and Reuven Gordon. Label-free free-solution single-molecule protein–small molecule interaction observed by double-nanohole plasmonic trapping. *ACS Photonics*, 1(5):389–393, 2014.

[138] Alexander Gust, Adrian Zander, Andreas Gietl, Phil Holzmeister, Sarah Schulz, Birka Lalkens, Philip Tinnefeld, and Dina Grohmann. A starting point for fluorescence-based single-molecule measurements in biomolecular research. *Molecules*, 19(10):15824–15865, 2014.

[139] Ryan M Gelfand, Skylar Wheaton, and Reuven Gordon. Cleaved fiber optic double nanohole optical tweezers for trapping nanoparticles. *Optics letters*, 39(22):6415–6417, 2014.

[140] Jin-Ho Ahn, Jong-Ho Kim, Nigel F Reuel, Paul W Barone, Ardemis A Boghossian, Jingqing Zhang, Hyeonseok Yoon, Alice C Chang, Andrew J Hilmer, and Michael S Strano. Label-free, single protein detection on a near-infrared fluorescent single-walled carbon nanotube/protein microarray fabricated by cell-free synthesis. *Nano letters*, 11(7):2743–2752, 2011.

[141] Abdennour Abbas, Matthew J Linman, and Quan Cheng. New trends in instrumental design for surface plasmon resonance-based biosensors. *Biosensors and Bioelectronics*, 26(5):1815–1824, 2011.

[142] Armin Hoffmann, Krishna Neupane, and Michael T Woodside. Single-molecule assays for investigating protein misfolding and aggregation. *Physical Chemistry Chemical Physics*, 15(21):7934–7948, 2013.

[143] Irene Ament, Janak Prasad, Andreas Henkel, Sebastian Schmachtel, and Carsten Sonnichsen. Single unlabeled protein detection on individual plasmonic nanoparticles. *Nano letters*, 12(2):1092–1095, 2012.

[144] Yue Zhuo, Huan Hu, Weili Chen, Meng Lu, Limei Tian, Hojeong Yu, Kenneth D Long, Edmond Chow, William P King, Srikanth Singamaneni, et al. Single nanoparticle detection using photonic crystal enhanced microscopy. *Analyst*, 139(5):1007–1015, 2014.

[145] Srdjan S Acimovic, Maria A Ortega, Vanesa Sanz, Johann Berthelot, Jose L Garcia-Cordero, Jan Renger, Sebastian J Maerkl, Mark P Kreuzer, and Romain Quidant. Lspr chip for parallel, rapid, and sensitive detection of cancer markers in serum. *Nano letters*, 14(5):2636–2641, 2014.

[146] Peter Zijlstra, Pedro MR Paulo, and Michel Orrit. Optical detection of single non-absorbing molecules using the surface plasmon resonance of a gold nanorod. *Nature nanotechnology*, 7(6):379–382, 2012.

[147] Ana Zehtabi-Oskuie, Hao Jiang, Bryce R Cyr, Douglas W Rennehan, Ahmed A Al-Balushi, and Reuven Gordon. Double nanohole optical trapping: dynamics and protein-antibody co-trapping. *Lab on a Chip*, 13(13):2563–2568, 2013.

[148] Ahmed A Al Balushi, Ana Zehtabi-Oskuie, and Reuven Gordon. Observing single protein binding by optical transmission through a double nanohole aperture in a metal film. *Biomedical optics express*, 4(9):1504–1511, 2013.

[149] Ahmed Al Balushi and Reuven Gordon. Real-time dynamics of single protein-small molecule interactions with label-free, free-solution double-nanohole optical trapping. In *Frontiers in Optics*, pages FTh1E–7. Optical Society of America, 2014.

[150] Ronald E Stenkamp, Isolde Le Trong, Lisa Klumb, Patrick S Stayton, and Stefanie Freitag. Structural studies of the streptavidin binding loop. *Protein Science*, 6(6):1157–1166, 1997.

[151] Elizabeth A Meade, William L Smith, and David L Dewitt. Differential inhibition of prostaglandin endoperoxide synthase (cyclooxygenase) isozymes by aspirin and other non-steroidal anti-inflammatory drugs. *Journal of Biological Chemistry*, 268(9):6610–6614, 1993.

[152] Ahmed A Al Balushi and Reuven Gordon. A label-free untethered approach to single-molecule protein binding kinetics. *Nano letters*, 14(10):5787–5791, 2014.

[153] Matthew D Shortridge, David S Hage, Gerard S Harbison, and Robert Powers. Estimating protein- ligand binding affinity using high-throughput screening by nmr. *Journal of combinatorial chemistry*, 10(6):948–958, 2008.

[154] Rebecca L Rich, Yasmina SN Day, Thomas A Morton, and David G Myszka. High-resolution and high-throughput protocols for measuring drug/human serum albumin interactions using biacore. *Analytical biochemistry*, 296(2):197–207, 2001.

[155] Claire Dufour and Olivier Dangles. Flavonoid–serum albumin complexation: determination of binding constants and binding sites by fluorescence spectroscopy. *Biochimica et Biophysica Acta (BBA)-General Subjects*, 1721(1):164–173, 2005.

[156] Jianzhong Chen and David S Hage. Quantitative analysis of allosteric drug-protein binding by biointeraction chromatography. *Nature biotechnology*, 22(11):1445–1448, 2004.

[157] Peter Kurtzhals, Svend Havelund, IB Jonassen, and Jan Markussen. Effect of fatty acids and selected drugs on the albumin binding of a long-acting, acylated insulin analogue. *Journal of pharmaceutical sciences*, 86(12):1365–1368, 1997.

[158] Margarita Valero, Brígida Esteban, Rafael Peläez, and Licesio J Rodrïguez. Naproxen: hydroxypropyl-β-cyclodextrin: polyvinylpyrrolidone ternary complex formation. *Journal of Inclusion Phenomena and Macrocyclic Chemistry*, 48(3):157–163, 2004.

[159] Jianzhong Chen, Corey Ohnmacht, and David S Hage. Studies of phenytoin binding to human serum albumin by high-performance affinity chromatography. *Journal of Chromatography B*, 809(1):137–145, 2004.

Appendix A

Observing single protein binding by optical transmission through a double nanohole aperture in a metal film

Originally published:

Ahmed A. Al Balushi, Ana Ana Zehtabi-Oskuie, and Reuven Gordon, Observing single protein binding by optical transmission through a double nanohole aperture in a metal film, Biomedical Optics Express, 4(9), 1504 1511 (2013).

A.1 Abstract

We experimentally demonstrate protein binding at the single particle level. A double nanohole (DNH) optical trap was used to hold onto a 20 nm biotin-coated polystyrene (PS) particle which subsequently is bound to streptavidin. Biotin-streptavidin binding has been detected by an increase in the optical transmission through the DNH. Similar optical transmission behavior was not observed when streptavidin binding sites where blocked by mixing streptavidin with excess biotin. Furthermore, interaction of non-functionalized PS particles with streptavidin did not induce a change in the optical transmission through the DNH. These results are promising as the DNH trap can make an excellent single molecule resolution sensor which would enable studying biomolecular interactions and dynamics at a single particle/molecule level.

A.2 Introduction

Single protein studies typically bind a protein to a surface and then look at protein-protein interactions through additional binding events. Impressively, recent studies have shown single protein binding sensitivity using plasmonic nanoparticle by monitoring resonance shifts and by photo-thermal transduction to achieve increased sensitivity. Those works, however, have the disadvantage of using one of the binding sites of the protein for the surface-attachment and obscuring/blocking a specific side of the protein by the surface. They also restrict the motion of the protein, and so the binding event is not in its native state.

Optical trapping of single proteins can, in principle, allow for studying protein interactions without the need for surface binding. Recently, our group has developed an optical trapping approach using nano-apertures, which allows for trapping of single

proteins. Here we show single protein binding, using the biotin-streptavidin model system. Since biotin is a small molecule it requires tethering to a larger particle to observe binding with streptavidin, however, we might be able in the future to observe single protein binding of bigger molecules without the need of tethering because molecules can be held in place by the optical trap. Protein binding is confirmed by performing two appropriate control experiments: 1) we trapped biotin-coated PS particles and then flowed in streptavidin with the binding sites being blocked off by mixing it with excess biotin, and 2) we trapped non-functionalized PS particles and then flowed in streptavidin. Both of the control experiments consistently did not show any binding. We believe that this is the first definitive measurement of single protein binding using an optical trapping system, without the need for tethering the protein to a larger particle.

A.3 Experimental Setup

Figure A.1 shows a schematic of the DNH optical trapping system which is based on Thorlabs optical tweezer kit (OTKB). We used an 830 nm continuous laser (Sacher Lasertechnik Group, Model TEC 120) which has the advantage of better detection efficiency for the photodetector than a 980 nm laser and helps with trapping smaller objects due to the favorable wavelength-dependent scaling. The trapping beam was focused into the sample using a 100 oil immersion microscope objective with a 1.25 numerical aperture. A half-wave plate (HWP) was used to rotate the polarization of the incident beam so that the electric field of the beam is aligned along the cusps of the DNH giving a large local field enhancement and hence creating a strong trapping point. Transmitted light through the DNH was collected using a 10 condenser microscope objective with 0.25 numerical aperture, and measured by a silicon-based

avalanche photodetector (APD) (Thorlabs APD110A). We used a data acquisition board to record the voltage values generated by the APD at a sampling frequency of 2 kHz. The setup is modified so as to allow for microfluidic delivery to the trapping site where we used a dual Fusion Syringe Pump (Chemyx Inc., Model Fusion 200) to sequentially flow biotin-coated PS particles and streptavidin into the microfluidic channel. Here, we followed the same microfluidic chip fabrication process outlined in the Supporting Information of our previous work on flow dependant trapping, with the resultant microfluidic channel dimensions being 65 m by 800 m.

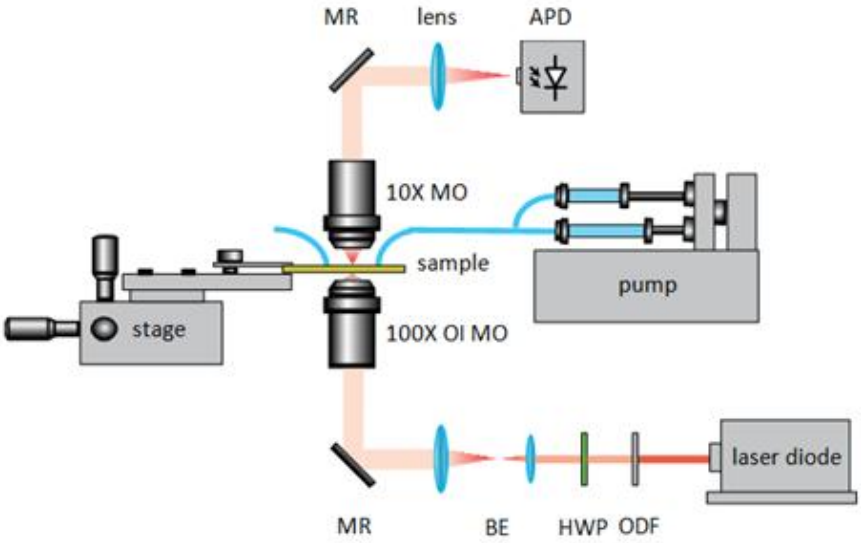

Figure A.1: A schematic of the DNH optical trap with dual microfluidic input. Abbreviations used: ODF = optical density filter; HWP = half-wave plate; BE = beam expander; MR = mirror; MO = microscope objective; OI MO = oil immersion objective; APD = avalanche photodetector.

A focused ion beam (Hitachi FB-2100 FIB) was used to mill a DNH in a 100 nm thick Au film on a glass substrate with a 5 nm titanium adhesion layer (EMF Corp.). Figure A.2 shows a schematic of the protein binding experiments and a scanning electron microscope image (Hitachi S-4800 FESEM) of the DNH used in trapping experiments. Separation between the cusps is measured to be 30 nm which is nearly

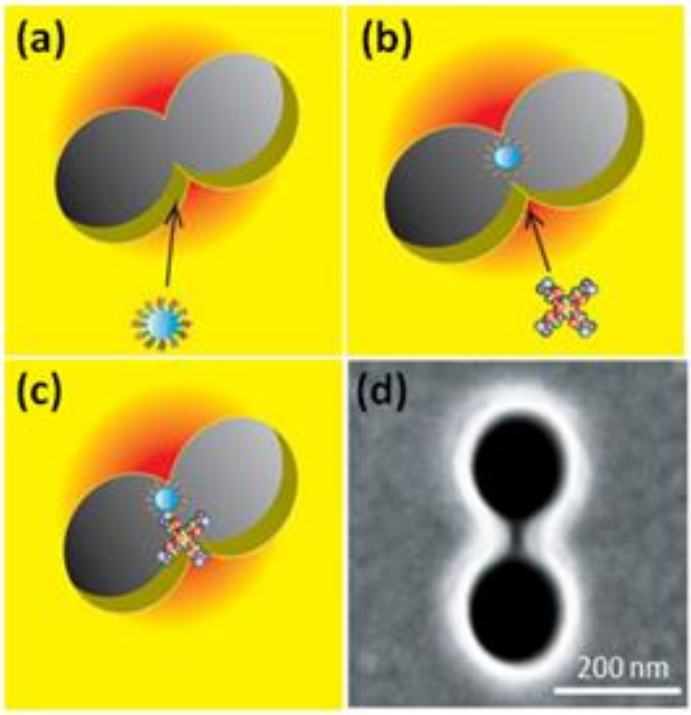

Figure A.2: A schematic showing the protein binding experiments. (a) 20 nm biotin-coated PS particle approaches the DNH. (b) Introduction of streptavidin to the trapping site once a successful trapping event of 20 nm biotin-coated PS particle is achieved. (c) Streptavidin is bound to biotin between the two sharp cusps of the DNH. (d) A scanning electron microscope image of the DNH used in the protein binding and control experiments.

optimal to the 25 nm separation found to be the best for trapping 20 nm PS particles according to our previous studies. As with our previous work on trapping a protein, prior to conducting trapping experiments we formed a monolayer of mPEG thiol on the Au surface by immersing the Au sample in a 5 mM aqueous solution of mPEG thiol (molecular weight, 5 kDa) at room temperature overnight and then rinsing it with DI water. This helps prevent streptavidin from adsorbing on the Au surface.

Here we experimentally demonstrate protein binding by trapping 20 nm biotin-coated PS particles (NANOCS PS20-BN-2) and then bind it with streptavidin with a molecular weight 60 kDa. The streptavidin was purchased in powder form (SIGMA-ALDRICH, Product No. 85878) and the desired concentration was obtained by dis-

solving it in phosphate buffered saline (PBS). Biotin, which is also known as vitamin B7 and vitamin H, has an extraordinary binding affinity to streptavidin, with a dissociation constant in the order of about 10^{-14} mol/L, making it the strongest non covalent bond found in nature.

A.4 Protein Binding Experiments

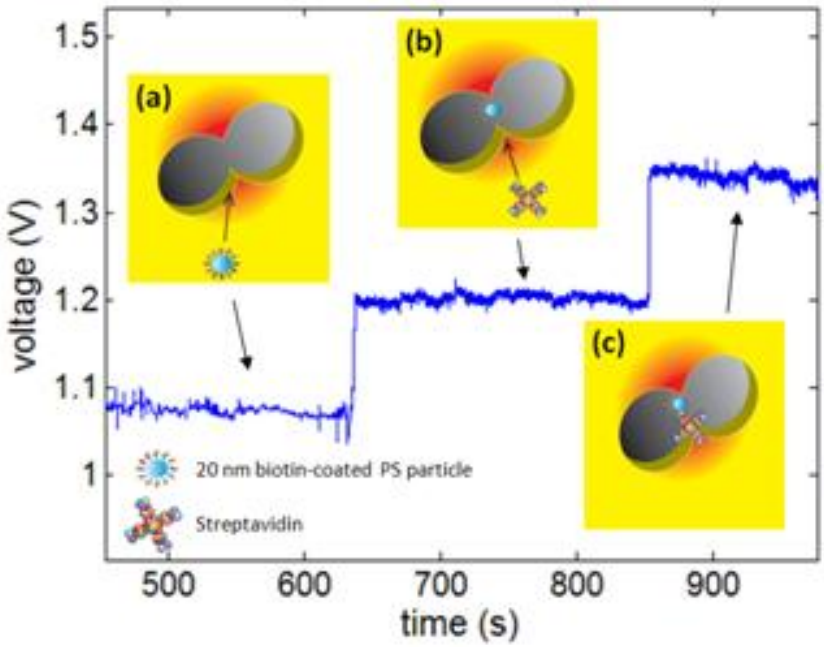

Figure A.3: Time trace of optical transmission through the DNH where (a) shows flowing 20 nm biotin-coated PS particles through the microfluidic channel, (b) trapping of 20 nm biotin-coated PS particle between the two sharp tips formed by two overlapping DNHs and subsequently flowing streptavidin, and (c) binding between 20 nm biotin-coated PS particle and streptavidin.

Figure A.3 shows the time evolution of the optical power transmitted through the DNH and the schematics the corresponding steps of the protein binding experiments, where (a) shows flowing 20 nm biotin-coated PS particles (0.01% w/v in DI water), (b) trapping event of 20 nm biotin-coated PS particle between the two sharp tips of the DNH and subsequently flowing streptavidin (0.01% w/v in PBS), (c) binding

of streptavidin with the trapped biotin-coated PS particle. We repeated all of the experiments and controls at least 4 times. When a biotin-coated PS particle gets trapped between the cusps of the DNH it dielectrically loads the region and causes an enhancement of the local optical field intensity and increased DNH transmission. Once a stable trapping event of a biotin-coated PS particle is achieved, streptavidin is flowed into the channel where it gets bound to the trapped particle, causing further dielectric loading to the DNH region and consequently a higher optical transmission is obtained. We used a moderate flow rate of 5 μL/min which enables fast enough delivery of streptavidin to the trapping site and at the same time does not wash away the trapped particle, as was investigated in one of our previous studies.

The setup is designed such that delivery of streptavidin to the trapping site takes about 150 seconds from the time a successful trapping of biotin-coated PS particle is achieved. The delivery time of streptavidin to the trapping site of 150 seconds was related to the time for it to flow from the syringe to the trapping site at a flow rate of 5 μL/min. This indicates that a binding event occurs within a few seconds after the introduction of streptavidin to the trapping site, which is expected due to the high binding affinity of the streptavidin-biotin pair. Similar binding results were obtained on different days and with freshly made solutions. After each set of experiments, we flowed deionized water through the microfluidic channel for 30 minutes to make sure that the channel is clean for the next set of experiments.

A.5 Control Experiments

To show clearly that we are actually observing specific streptavidin-biotin binding, and not just co-trapping, we performed two separate control experiments using: 1) saturated streptavidin, 2) non-functionalized PS particles.

A.5.1 Saturated streptavidin

Figure A.4 shows the time trace of the optical transmission through the DNH with the schematic of the corresponding steps for the saturated streptavidin control experiment where, (a) shows flowing 20 nm biotin-coated PS particles, (b) trapping event of 20 nm biotin-coated PS particle and subsequently flowing saturated streptavidin, and (c) saturated streptavidin does not bind to the trapped 20 nm biotin-coated PS particle. In this set of control experiments, we trapped a biotin-coated PS particle and then flowed in saturated streptavidin in which all the binding sites were blocked off by mixing it with excess biotin (SIGMA-ALDRICH), molecular weight 344.31 Da. As the figure shows, there is an increase in the optical transmission through the DNH observed after flowing the 20 nm biotin-coated PS particles indicating a successful trapping event of biotin-coated PS particle. However, we have not observed any further increase in the optical transmission for the subsequent 25 minutes after flowing saturated streptavidin.

A.5.2 Non-functionalized PS particles

Figure A.5 shows the time evolution of optical transmission through the DNH with the schematic of the corresponding steps for the non-functionalized 20 nm PS particles where (a) shows flowing 20 nm non-functionalized PS particles (0.01% in DI water), (b) trapping event of 20 nm PS particle and then flowing streptavidin, and (c) streptavidin does not bind to the trapped 20 nm PS particle. Here, we flowed in streptavidin (with the same concentration used in the main binding experiments) after successfully achieving a trapping event of a 20 nm non-functionalized PS particle. Introduction of streptavidin to the trapping site did not cause any change in the optical transmission through the DNH for the subsequent 25 minutes of achieving a stable trapping event of a non-functionalized PS particle.

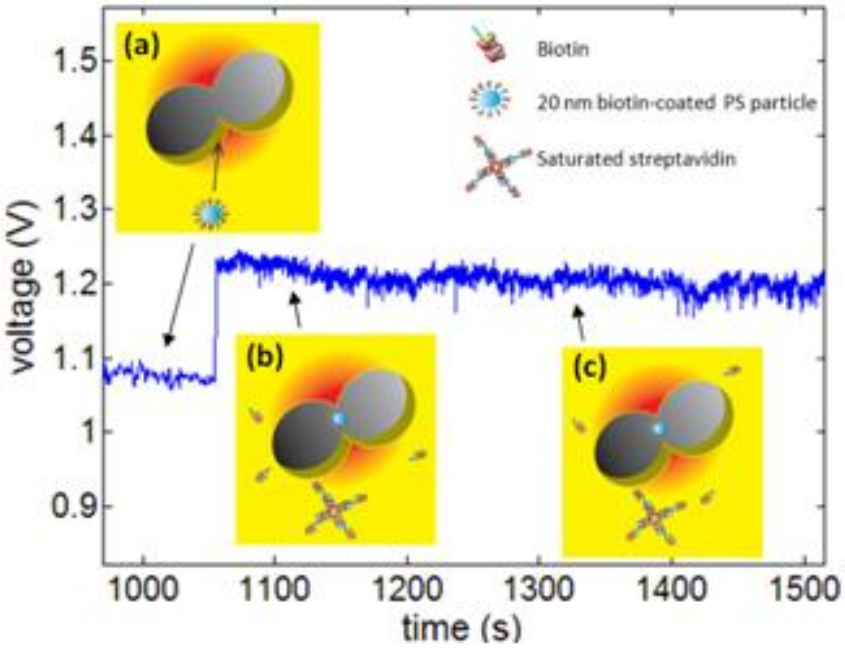

Figure A.4: Time trace of optical transmission through the DNH for the saturated streptavidin control experiment where (a) shows flowing 20 nm biotin-coated PS particles through the microfluidic channel, (b) trapping of 20 nm biotin-coated PS particle between the cusps of the DNH and subsequently flowing saturated streptavidin, and (c) saturated streptavidin does not bind to the trapped 20 nm biotin-coated PS particle.

A.6 Discussion

A.6.1 DNH trap for single protein binding detection

Our objective in this current study has been to observe single protein binding using the DNH trap system. Our experimental results on single protein binding as well as the control experiments explicitly demonstrate that single protein binding detection is achievable by using the DNH optical trap system. Unlike other detection systems which require tethering and/or surface functionalizeation of the particles of interest, our system uses the trapping laser beam to hold the trapped particle in a well defined trapping region between the two cusps of the DNH. Furthermore, our DNH trap allows for single protein binding detection by simply measuring optical transmission

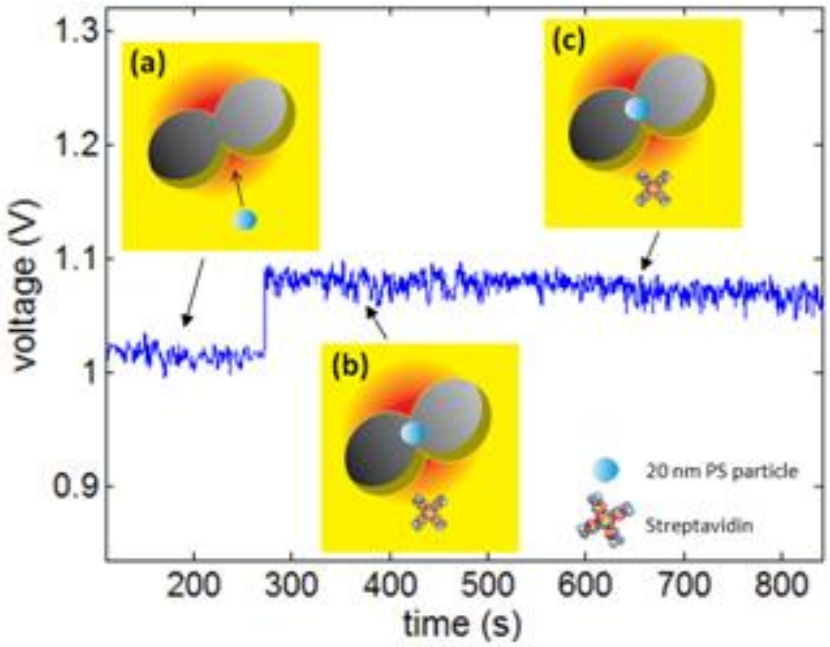

Figure A.5: Time trace of optical transmission through the DNH for the non-functionalized PS particle control experiment where (a) shows flowing 20 nm PS particles through the microfluidic channel, (b) trapping of 20 nm PS particle between the cusps of the DNH and subsequently flowing streptavidin, and (c) streptavidin does not bind to the trapped 20 nm PS particle.

of the same trapping laser beam through the DNH aperture without the need of measuring wavelength or having additional laser sources or fluorescently labeling the target particle. This straightforward intensity measurement of optical transmission could yield a much faster detection of protein binding and therefore, allow the study of single protein binding dynamics at a nanosecond scale. Besides, the distinct and abrupt jump in the optical transmission through the DNH serves as a potential protein binding sensor with a signal-to-noise ratio (SNR) of 18. Indeed a recent study used a streptavidinR-phycoerythrin conjugate with a molecular weight of 300 kDa (50 times bigger molecule than the one we used in our study) to clearly detect protein binding using surface plasmon resonance shift of Au nanorods.

Protein-protein interactions are generally temperature-sensitive and require systems which operate below the denaturation temperature of the proteins under study.

For instance, recent works on protein studies, like the resonant-based plasmonic particle trapping and photonic crystal trapping systems suffer from heating effects and might need to apply one or more thermal management strategies to overcome heating issues; for example, the use of adjacent metal films as a natural heat sink in nanopillar plasmonic trapping. These resonant trapping systems do not only generate heat under resonant absorption but also add experimental complexity in terms of applying thermal management strategies. On the other hand, the DNH trap system is non-resonant and the Au film plays a role in reducing the heating effects due to its good thermal conductivity. Considering other works on optical trapping where there is a metal membrane, we expect that the temperature increase is only a few degrees Celsius and so this is not expected to hinder protein binding, protein folding, or other molecular investigations. We are presently working on integrating Raman into the setup so that we could potentially measure the temperature distribution by looking at the ratio between Stokes and anti-Stokes peaks. Here, we expect the temperature at the trapping point to be well below 70 °C as this is the temperature required to break the streptavidin-biotin bond without denaturing streptavidin and such thermal effects on streptavidin-biotin pair have not been observed in our experiments. This feature makes our DNH optical aperture trapping system thermally suitable for protein-protein studies, for example, studying the dynamics of protein folding and unfolding of BSA.

It is possible to envision schemes whereby the optical polarization may be used to rotate the trapped molecules, as has been achieved for other works. The double nanohole constrains the polarization of the maximum trapping field along the cusps between the two nanoholes, and therefore trapping is not possible.

In our previous studies we found that steric hindrance prevents co-trapping of two similar particles in the region between the two sharp tips of DNH. Therefore, it stands

reasonable here to assume that co-trapping of two 20 nm biotin-coated PS particles in a 30 nm gap is subject to steric hindrance too. Indeed, in our current study we have neither observed co-trapping of a biotin-coated PS particle with another biotin-coated PS particle nor co-trapping of streptavidin with streptavidin. In addition, we have not observed any co-trapping behavior in our control experiments. This further proves that the results obtained in this study are as a consequence of streptavidin-biotin binding and not co-trapping of two similar particles.

A.6.2 Future directions

It is interesting that we observed protein binding at a single molecule level using the DNH aperture trap. We aim to extend our study to further test the binding sensitivity of our system by using binding affinity pairs which have lower disassociation constants. In addition, there is also the potential of analyzing time traces of binding events of different binding affinity pairs to investigate the possibility of identifying the nature of trapped/bound particle(s). It is also possible to modify our existing setup to analyze the Raman signal of the trapped/bound particle(s) for which we have experience with Raman spectroscopy. In fact, we are presently attempting to simultaneously measure the Raman signal of the trapped object by using a trapping laser, a Raman excitation source and appropriate filters, and a spectrometer after the double nanohole. Moreover, it is interesting to study isolated nanoparticles within a heterogeneous mixture. Furthermore, we are interested in studying the dynamics of folding and unfolding of single proteins. Moreover, we are interested in fluorescence studies of trapped particles provided that quenching effects at the Au surface can be avoided.

A.7 Conclusion

In conclusion, we have used a DNH-based optical trap to detect streptavidin-biotin binding at the single molecule level. This was achieved by measuring the optical transmission through the DNH. To further confirm that the observed increase in optical transmission through the DNH is due to the specific binding of streptavidin to biotin, we preformed two appropriate control experiments that did not show binding, i.e. using saturated streptavidin and non-functionalized PS particles. The control experiment results were consistent with the main experimental results. These results are promising for biomolecular interaction studies at the single molecule/particle level; for example studying single protein binding interactions and dynamics at single molecule level.

Appendix B

Label-free free solution single-molecule protein-small molecule interaction observed by double nanohole plasmonic trapping

Originally published:

Ahmed. A. Al Balushi, and Reuven Gordon, Label-free free solution single-molecule protein-small molecule interaction observed by double nanohole plasmonic trapping, ACS Photonics, 1(5), 389 393 (2014).

B.1 Abstract

The interaction of proteins with small molecules is fundamental to their function in living organisms and it is widely studied in drug development. Here we use the double nanohole optical trapping technique to observe real-time label-free free-solution single molecule dynamics of three complexes: the biotin-streptavidin, biotin-monovalent streptavidin and acetylsalicylic acid-cyclooxygenase 2. Radically different behavior is seen between the protein with and without the small molecule binding. This detection platform is scalable, inexpensive and highly sensitive, which may transform drug discovery based on protein small molecule interactions.

B.2 Paper Content

Protein-small molecule interactions (PSMIs) play an important role in biological functions. PSMIs are also of primary interest for the development of drugs, for example through inhibition of protein interactions. While many works have studied PSMIs, only few approaches exist that do not require tethering to a surface or labeling. Tethering to a surface has the disadvantages of using a binding site, restricting the protein motion with an anchor and introducing steric hindrance from the surface proximity. Exogeneous labels, such as fluorescent tags, present similar challenges, including using up a binding site and altering the natural state of the molecules of interest, but also add the complexity of using a label. So far, calorimetry and interferometry have been used as label-free, free-solution techniques. Calorimetry has high concentration detection limits and is restricted to systems with an appreciable reaction enthalpy. Interferometry makes use of refractive index changes from PSMIs and can detect PSMIs in the micromolar range.

Ideally, we would like to introduce new label-free, free-solution methods that work

at the single molecule level, where it is possible to observe real time dynamics that are not obscured by an ensemble. There are many advantages of working at the single molecule level. For example, with access to these dynamics and without the need for synchronization, we can compare more directly to molecular dynamics calculations. Working at the single molecule level represents the ultimate practical sensitivity limit. It also offers opportunities for distinguishing components of heterogeneous systems, such as cell lysates.

Here we consider the use of optical trapping to observe, in real time, the dynamics of a single streptavidin molecule, comparing the cases with and without exposure to biotin. Our optical trapping approach is similar to that reported in previous works, as shown schematically in Figure B1(a). Briefly, a double nanohole (DNH) aperture is milled using a focused ion beam in a 100 nm Au film adhered to a glass slide with a 5 nm Ti layer (Figure B1(c)). The gold film forms the top of a microwell in an inverted microscope optical trapping setup using an 820 nm laser diode. The transmission of the laser diode through the double nanohole aperture is used to detect and monitor the trapping events since dielectric loading creates a large variation in the transmitted intensity. Typically, a trapping event gives a 10% change in transmission, depending on the size of the nanoparticle trapped and the size of the aperture. Our previous studies show that trapping of two particles of a comparable size induce a two step increased transmission through the DNH structure, and this has also been reported by other groups. We have not observed such behavior in our current study, which is likely due to steric hindrance which prevents trapping of two similar particles between the two sharp tips of the DNH. It should be noted that this method produces negligible heating due to the presence of a gold film; the heating is expected to be of the order of 0.1K. Furthermore, the technique produces copious signal for only 3 mW of laser power, such that an optical density filter is used to avoid saturation of the avalanche

photodiode.

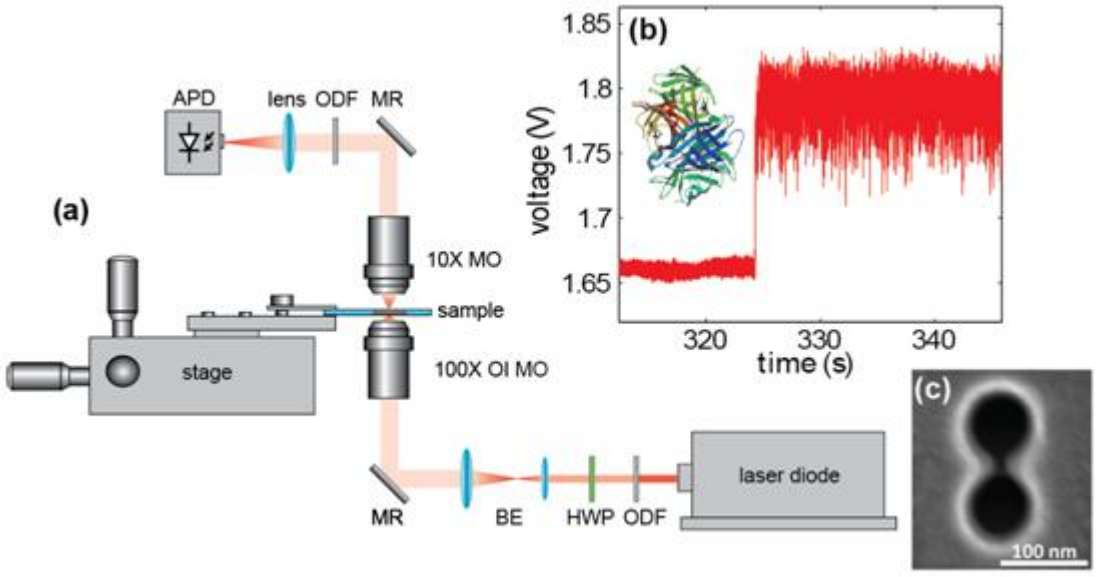

Figure B.1: (a) A schematic of the double nanohole optical trap. Abbreviations used: ODF = optical density filter; HWP = half-wave plate; BE = beam expander; MR = mirror; MO = microscope objective; OI MO = oil immersion objective; APD = avalanche photodetector. (b) Optical trapping of biotinylated streptavidin (inset) seen as a sudden discrete jump in APD signal. (c) An SEM image of the double nanohole.

We prepared streptavidin solutions (Sigma Aldrich, 85878, molecular weight 60 kDa) in buffer with 0.01% w/v concentration. A portion of the solution was separated and exposed to excess biotin (Sigma Aldrich, B4501, molecular weight 244.31 Da), which fully saturates the binding sites due to its high affinity. Figure 2 shows the trapping dynamics of the streptavidin solution with and without the biotin. For the concentrations used in this study, the time to trap was typically 5 minutes; however, this can be made shorter by increasing the concentration, and we have studied this quantitatively in another work. The trapping event is seen by a discrete jump in the transmitted laser intensity, as denoted by arrows in Figures B2(a) and (d). The streptavidin without biotin shows fluctuations in the transmitted intensity of the trapping laser with a timescale of about 600 ms, as seen in Figures B2(b) and (c)

(taken from different samples on different days). These fluctuations are absent in the biotinylated streptavidin, as seen in Figures B2(e) and (f). An autocorrelation of the trapping events found for streptavidin and biotinylated streptavidin is shown in Figure 3 which shows clearly the slower timescale dynamics of the streptavidin as compared to biotinylated streptavidin molecule. We preformed these experiments on different days and from different solutions and all the results obtained are consistent with Figure B3. To obtain the autocorrelation, we typically used a time sequence of 400 seconds (sampling at 1 MHz) after trapping. This extended time duration is highly conservative, but in general, at least 100 periods of the shortest timescale of interest is recommended to avoid spurious artefacts. We then used the Matlab function autocorr() to compute the autocorrelation.

The change in the light transmitted through the (DNH) aperture can arise from differences in the size of the particle trapped, but also from changes in the particle shape or orientation, for example due to unfolding of proteins or conformal changes. These marked differences are not expected to arise from mass-loading since biotin has a mass ¡0.5% the mass of streptavidin. The streptavidin without biotin shows fluctuations that are not present when biotin is added. This is consistent with numerical studies of streptavidin that suggest that the binding loop is highly mobile in the absence of biotin it would be interesting to attempt quantitative comparisons with molecular dynamics simulations in the future. There are many cases in the literature where binding of a small molecule alters the molecular dynamics of a protein substantially. The change in the optical transmission through the double nanohole aperture is expected to vary considerably due to stretching of the protein since the dipole moment increases along the axis of elongation. It is energetically favorable of the optical trap to stretch out the protein and this leads to more light transmitted through the double nanohole. Similar stretching behavior has been reported in

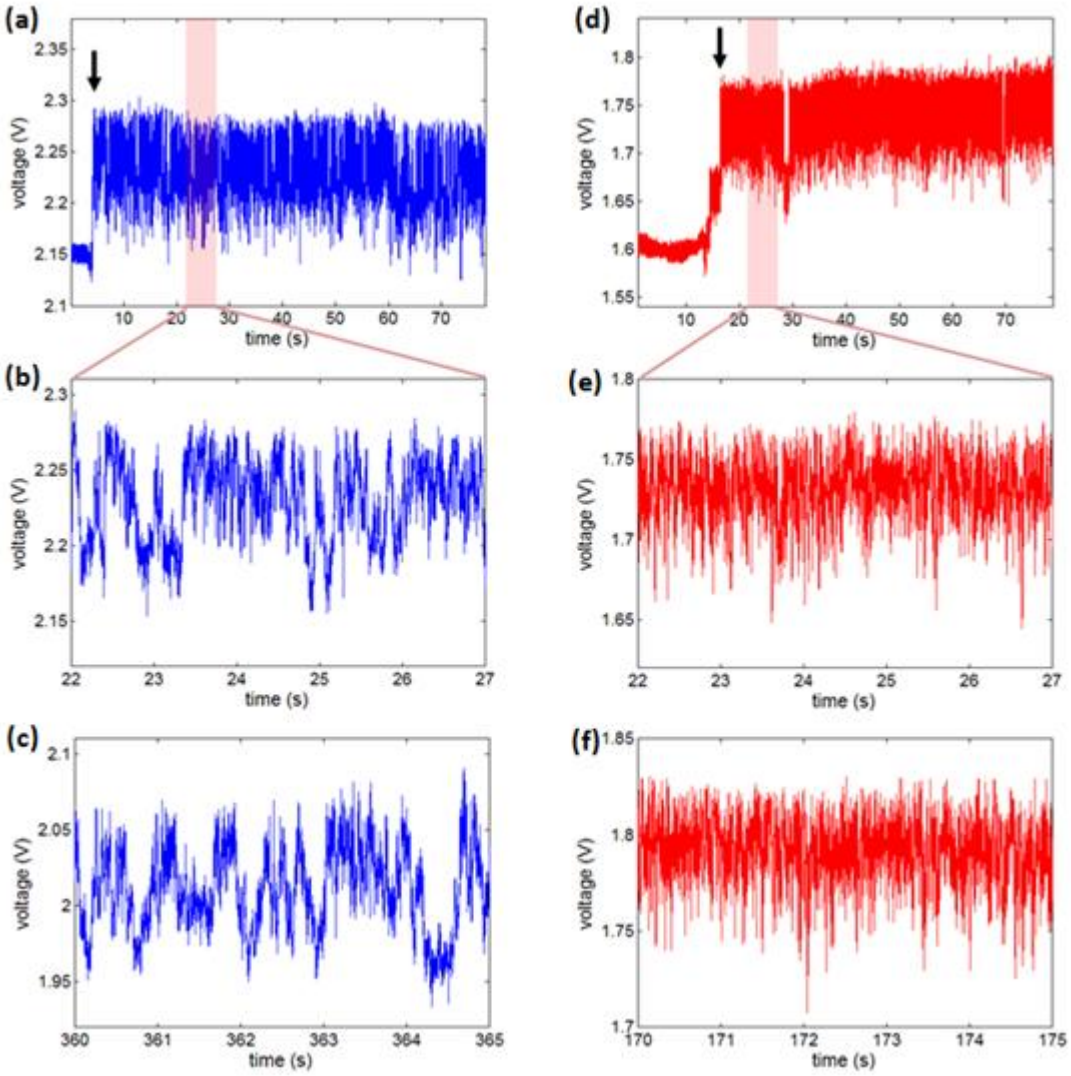

Figure B.2: Trapping dynamics of streptavidin without and with biotin as measured from the APD voltage. (a) A time trace of a trapping event of a bare streptavidin molecule seen as an abrupt jump in the voltage level as denoted by the arrow. (b) Zoom-in of (a). (c) Repeat of (a) taken from a different sample on different day. (d) A time trace of a trapping event of a biotinylated streptavidin molecule seen as a discrete jump in the voltage level as indicated by the arrow. (e) Zoom-in of (d). (f) Repeat of (e) taken from a different sample on different day.

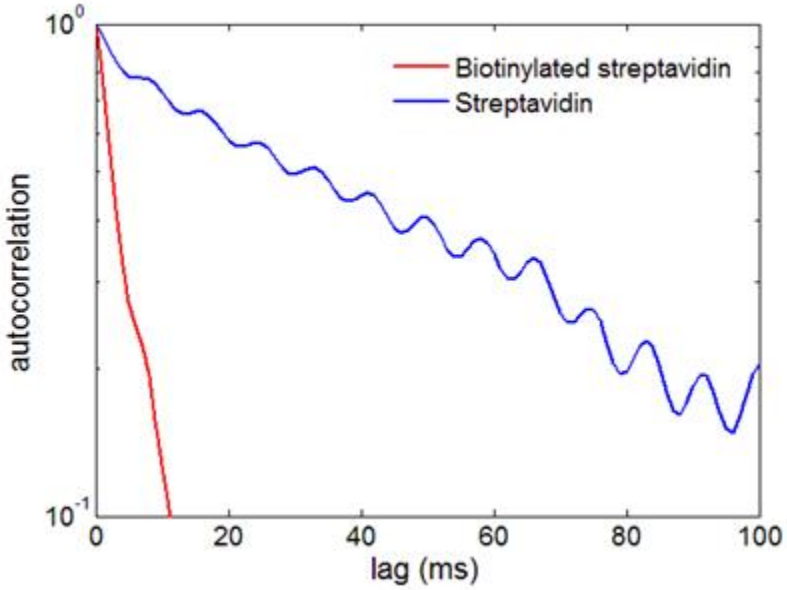

Figure B.3: Autocorrelation of trapped streptavidin APD signal fluctuations with and without biotin, as seen in Figures 2(b) and (e).

other optical trapping systems, albeit for much larger particles such as cells. The increase in intensity at the trapping event comes from dielectric loading of the DNH by the protein, which allows for more light transmission. The trapped particle is subject to Brownian motion and conformal changes, which also change the amount of light transmitted, and show up as increased fluctuations in the signal after trapping. A more elongated particle should have higher polarizability, and therefore will give higher light transmission through the aperture. The streptavidin alone has larger fluctuations than the streptavidin-biotin complex, and these suggest that the streptavidin can fluctuate between an elongated and compressed state in the absence of biotin. These fluctuations occur on a timescale of 600 ms, which is directly related to the autocorrelation as the slope of the decay. The fluctuations of the biotinylated streptavidin are likely to be from translational Brownian motion, and have a timescale of 20 ms, as we have seen for the autocorrelation of nanoparticles in our past work.11 In our previous study, the DNH unfolded bovine serum albumin (BSA), which is well

known to have an elongated unfolded state. It appears that the DNH does elongate the streptavidin, as seen by increased light transmission through the aperture which comes from high polarizability of an elongated streptavidin molecule; however, we have not found any reference to the hinge-like unfolding of streptavidin as seen with BSA. Figure B.2(d) shows occasional steps for the biotinylated-streptavidin; which suggest that conformal or orientation changes can occur even in the presence of biotin, although much less frequently as compared with bare streptavidin. We do not believe that these changes are the result of dissociation of the biotin, since this typically occurs on the timescale of 108 s. Further investigation, perhaps comparing with numerical simulations, should help to clarify which process is taking place here. In addition, the autocorrelation approach may be used to measure transitions between the bound and unbound states and extract binding kinetics; however, this was not seen in the present work due to the high binding affinity of the biotin-streptavidin system. The confidence of distinguishing the bound and unbound states will require typically autocorrelation times that are 100 times the shortest timescale of interest, as mentioned previously. In the present study, the time scales of interest are around 10 to 100 ms, so this would limit the autocorrelation to the study of binding rates of the order of 0.1-1 Hz. This is also clear from Figures 2(b) and (c), even without the autocorrelation, where the jumpy behaviour has a timescale of the order of 1 second and so we can see transitions between the two states by analysis of the time series as well (e.g., by looking at the RMS deviation). We have observed fouling of the nanoholes as seen by a drop in intensity, which depends on the cleanliness of the Au sample handling. When this happens, we no longer use the trap and we have not studied the time dynamics of this process. With care, the typical period of usage for a single sample is around a month. A particle of comparable size to the proteins being studied would also show a step-like time response, but would give a different

time series (e.g., autocorrelation would vary), as we have studied in detail in other works.

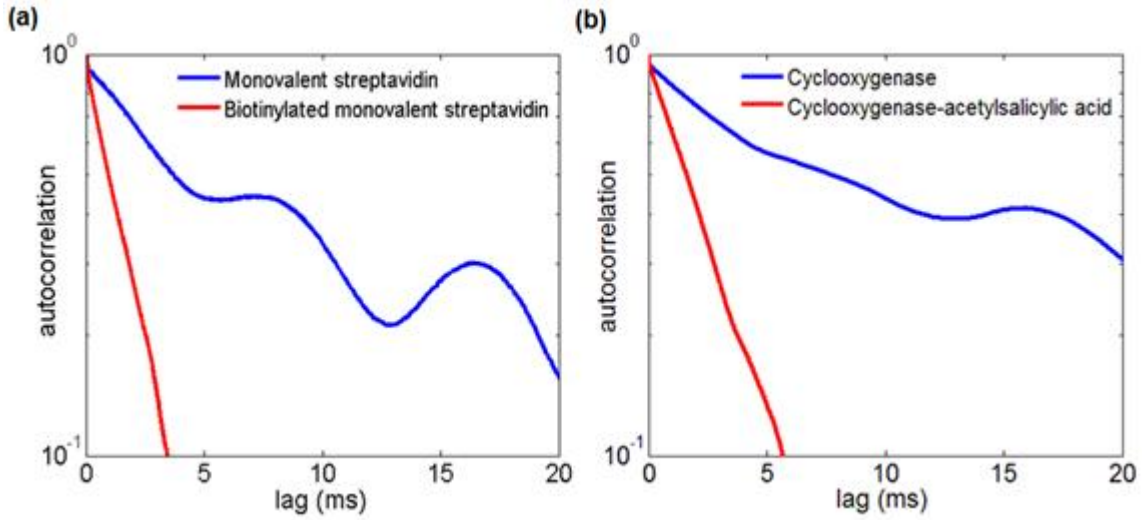

Figure B.4: Autocorrelation of time traces of trapped monovalent streptavidin (a) and cyclooxygenase 2 (b) with and without small molecule binding.

To further establish the applicability of our approach to distinguish between the bound and unbound forms of a protein, we used two different proteins: (i) monovalent streptavidin and (ii) cyclooxegenase 2. As for (i) we obtained monovalent streptavidin (molecular weight 54 kDa) with E6 tag as described in ref. 24 from the Howarth group, UK. The monovalent streptavidin solution was prepared at 0.01 % w/v concentration in buffer with some portion of it mixed with excess biotin to block the active binding site of the monovalent streptavidin. For (ii) we prepared cyclooxygenase 2 (Sigma Aldrich, C0858, molecular weight 72 kDa) in buffer with 0.01% w/v concentration. A portion of the cyclooxygenase 2 solution was mixed with acetylsalicylic acid (known also as asprin) with a molecular weight 180.16 Da, which irreversibly inhibits the cyclooxygenase by binding the acetyl group of acetylsalicylic acid to a serine residue of cyclooxegenase protein. Figures B4(a) and (b) show the respective autocorrelation of the time traces of a trapped monovalent streptavidin and cyclooxegenase proteins

with and without the small molecule binding. It is clear from both figures that a bare form of the protein in the trap has a slower time variation as when compared with the bound protein which can be easily inferred by looking at the autocorrelation of the signals in Figures B.4(a) and (b).

Future measurements are anticipated to observe the individual biotin binding events. In order to achieve this, we are considering a flow-channel setup, similar to our past work using nanospheres, which may be used to first trap the vacant streptavidin and then introduce biotin into the channel. The goal here will be to determine if the binding to the four binding sites in streptavidin can be observed individually. Obviously, it is of great interest to see if these results can be further extended to other PSMI systems that play a role in biological function. Also of interest is to see how scalable this approach is to enable multiplexed screening, for example by using multiple optical traps.

In summary, we have shown that by studying the optical trapping dynamics on a single protein we can easily distinguish between the bare and bound forms of a protein. Our approach does not require surface immobilization or exogeneous markers, and it gives the real-time dynamics of individual protein molecules, representing the ultimate practical limit for sensitivity. While our work only uses the model biotin-streptavidin system, this work shows great potential for applications to screening small molecule drug candidates by monitoring their influence on proteins of interest,1 and for the understanding the mechanisms of PSMIs.

B.3 Methods

B.3.1 Fabrication of DNH

We used a Hitachi FB-2100 focused ion beam to mill the DNH in 100 nm thick Au film on a glass substrate with a 5 nm Ti adhesion layer (EMF Corporation). The structure was fabricated at a magnification of 80 k with the accelerating voltage and current of the gallium ion beam being 40 kV and 0.001 nA respectively.

B.3.2 Gold sample preparation

A gold film sample, which contains the DNH as described in a past work, was washed with acetone, rinsed with isopropanol and dried with nitrogen. An imaging spacer (Sigma Aldrich, GBL654002) is placed on cover glass no. 0 (Goldseal, Ted Pella, inc.), which forms the microwell. 150 L of the protein solution was pipetted into the chamber and then the gold sample (with the gold side facing down) was placed on the imaging spacer to seal the well. The whole sample assembly was then mounted in the inverted microscope optical trapping setup as shown in Figure B1(a).

Appendix C

A label-free untethered approach to single-molecule protein binding kinetics

Originally published:

Ahmed. A. Al Balushi, and Reuven Gordon, A label-free untethered approach to single-molecule protein binding kinetics, Nanoletters 14(10), 5787 5791 (2014).

C.1 Abstract

Single molecule approaches provide rich real-time dynamics of molecular interactions that are not accessible to ensemble measurements. Previous single molecules studies have relied on labelling and tethering, which alters the natural state of the protein. Here we use the double-nanohole (DNH) optical tweezer approach to measure protein

binding kinetics at the single molecule level in a label-free, free-solution (untethered) way. The binding kinetics of human serum albumin (HSA) to tolbutamide and to phenytoin are in quantitative agreement with previous measurements, and our single-molecule approach reveals a bi-exponential behaviour characteristic of a multi-step process. The DNH optical tweezer is an inexpensive platform for studying the real-time binding kinetics of protein-small molecule interactions in a label-free, free-solution environment, which will be of interest to future studies including drug discovery.

C.2 Paper Content

Detecting protein - small molecule interactions (PSMIs) and studying their kinetics have generated significant interest due to their importance in diverse fields ranging from addressing fundamental questions about life at the cellular level to drug development. Conventional PSMI studies require labeling the molecule of interest and/or tethering it to a larger object. Tethering uses some of the available binding sites for surface attachment and restricts the free motion of the protein; and hence prevents monitoring binding partners in their native state. Labeling techniques often alter surface characteristics and natural activities of the molecules of interest, adding to the complexity of the measurements and creating photobleaching and heating problems. In order to overcome these issues, a number of label-free, free-solution methods like calorimetery, enthalpic arrays and interferometery have emerged as potential complements to approaches with labeling and tethering. However, these alternative ensemble methods also have disadvantages; for example, the requirement for large sample volumes, low sensitivity, long preparation times and poor detection limits.

Optical trapping using nanoapertures in metal films is an attractive method for de-

tecting real-time interactions at the single-molecule level in a label-free, free-solution environment. For example, we have shown that the DNH optical trap can distinguish between the bound and unbound forms of a single protein and also that it can detect the effect of protein binding on zipping and unzipping single DNA-hairpins. Unlike conventional perturbative trapping methods, where the laser power needed to trap a particle scales with the inverse fourth power of the particle size, our DNH trap has a strong signal for only 3 mW of laser intensity with negligible heating effects at the trapping site due to the good thermal conductivity of the gold film.

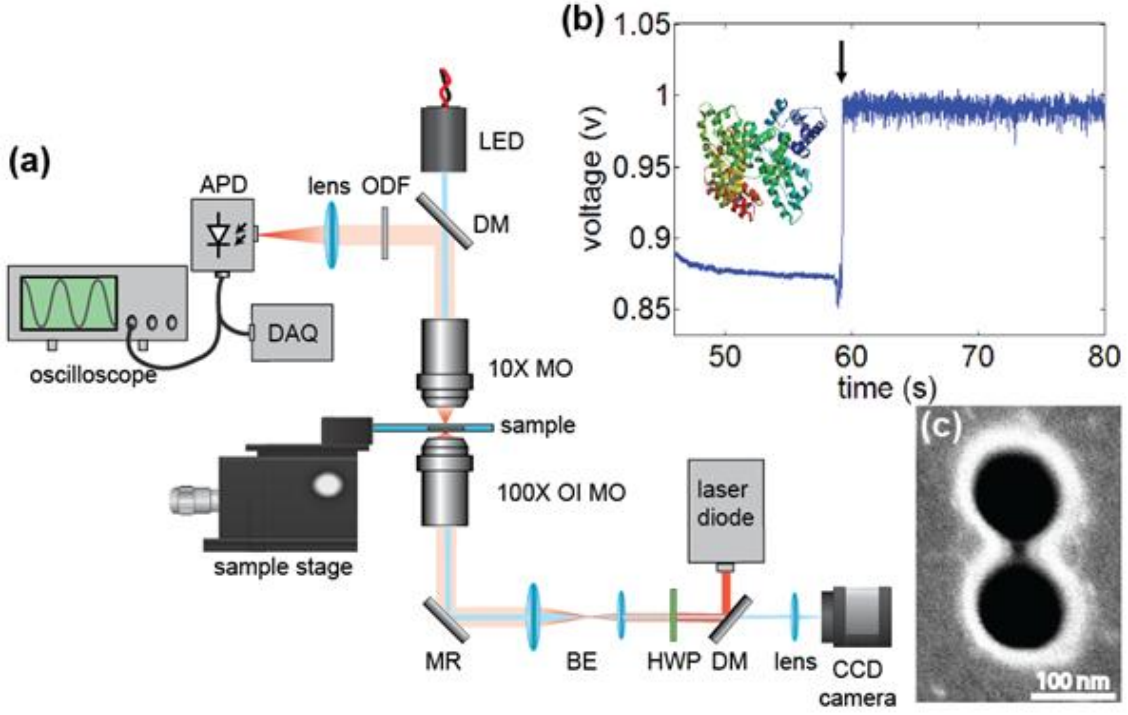

Figure C.1: (a) A schematic of the DNH optical trap. Abbreviations used: DM = dichroic mirror; HWP = half-wave plate; BE = beam expander; MR = mirror; MO = microscope objective; OI MO = oil immersion microscope objective; LED = light emitting diode; ODF = optical density filter; APD = avalanche photodiode; DAQ = data acquisition card. (b) Optical trapping of a bare HSA molecule (inset) seen as a sudden discrete jump in APD signal. (c) An SEM image of the DNH.

Here we use the DNH optical trapping system to measure the binding kinetics of a single human serum albumin (HSA) molecule interaction with two different ligands:

tolbutamide and phenytoin. Our optical trapping system (Figure C1 (a)) is based on a simple inverted microscope geometry, which is similar to that used in our previous studies. The transmission of an 820 nm laser diode through the DNH is used to detect a trapping event which, due to dielectric loading, corresponds to an abrupt increase in the transmission through the DNH aperture, typically around 10%, as denoted by the arrow in Figure C1(b). Associated with the abrupt increase in the transmission is an increase in the signal fluctuations attributed to the Brownian motion and the conformal changes of the trapped molecule in the DNH aperture. It has been reported that a small molecule binding to a protein alters its molecular dynamics. Recently we have shown that the DNH tweezer system can detect the change in dynamics of a protein due to binding and thus presents the possibility of distinguishing between its bound and unbound forms. A limiting factor that prevented us from studying the binding kinetics in our previous study was the high binding affinity of the complexes involved, requiring excessive observation times for single molecule studies. For example, the streptavidin-biotin complex has a dissociation constant, K_D, on the order of 10 fM. Our previous study focused on reporting on the ability of our DNH trap to distinguish between the bound and unbound forms of proteins. We were not able to show binding dynamics in that work, which is of critical importance when assessing the interactions between proteins and small molecules. Our past approach was to use multiple steps to analyse the bound and unbound configurations separately, instead of looking at on-off binding rates in situ.

Here, we extend our study of PSMIs using the DNH optical trap by considering affinity pairs that have larger dissociation constants than those considered in our pervious study. We have chosen HSA protein in our current study because it is a well established protein for studying protein-ligand interactions and because it has dissociation constants in the M range. In addition, the binding kinetics of HSA have

been characterized using a number of methods including nuclear magnetic resonance (NMR), surface plasmon resonance, fluorescence spectroscopy and chromatography. HSA is composed of three domains (I III), each containing two subdomanis (A and B) with the ligand-binding sites located at subdomains IIA and IIIA. Studies on HSA revealed that most ligands bind with high affinity to only one of the binding sites; with tolbutamide and phenytoin having a high affinity to site IIA. It should be noted here that there are a number of studies in the literature which suggest that HSA interacts at multiple binding sites with tolbutamide and with phenytoin, in which case a more general form of Eqn. 1 will need to be used, where the number of binding sites is taken into account. Therefore, assuming single-site binding, the interaction between the HSA and a ligand can be described by

$$P + L \underset{k_d}{\overset{k_a}{\rightleftharpoons}} PL \tag{C.1}$$

where k_a and k_d are the association and dissociation rate constants, with the dissociation constant $K_D = k_d/k_a$.

We prepared HSA solutions (Sigma-Aldrich, A1653500, molecular weight 66.478 kDa) in phosphate buffered saline solution (pH 7.4) with 0.01% w/v concentration. Separate portions of the HSA solution were exposed to tolbutamide (Toronto Research Chemicals, T535150, molecular weight 270.35 Da) and phenytoin (Toronto Research Chemicals, D491650, molecular weight 252.27 Da) such that the final concentration of the ligand in the solution is 30 μM.

Figure C2(a) shows typical time evolutions of a trapped HSA-tolbutamide pair in the DNH aperture, with the data normalized to the mean value which is shown as a red dotted line in the figure. The mean value of the time traces is used to define the threshold level between the bound and unbound states of the HSA molecule. We obtained the time traces of trapped molecules by sampling the APD voltage at

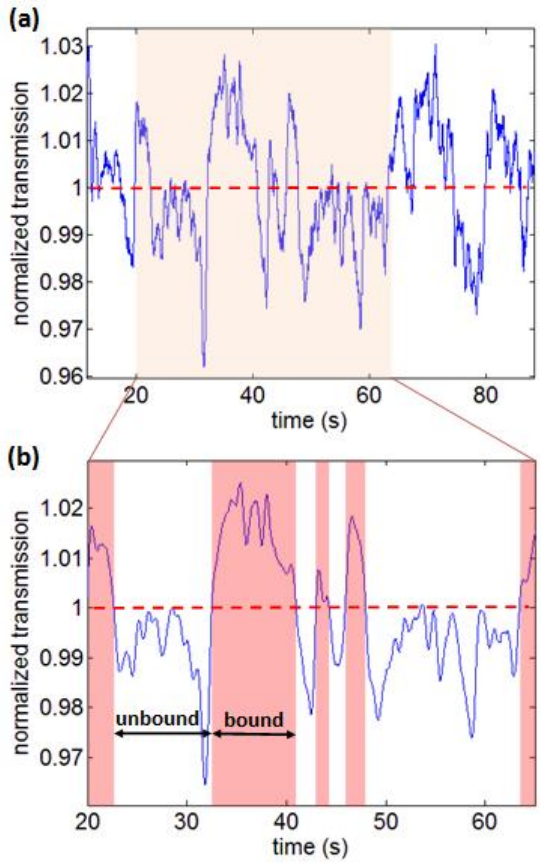

Figure C.2: (a) Time trace of the interaction of HSA with tolbutamide in the DNH aperture. (b) Zoom-in of (a) showing the bound and unbound states of the HSA molecule with the high transmission regions denoted by pink corresponding to the bound state.

1 MHz using a data acquisition card. We used a Savitzky-Golay noise reduction algorithm due to its advantage in preserving the features of the signal such as relative maxima, minima and width. The change in the light transmission through the DNH aperture for the HSA molecule with tolbutamide is due to conformal changes of the trapped protein with the protein in the bound state having higher polarizability and hence higher transmission through the aperture as compared with the protein in the unbound state. The interaction of HSA with tolbutamide can be characterized by Eqn. C1. From the time traces of the trapped HSA-tolbutamide pair (Figure C2 (a)) we obtained histograms of the residence times of the HSA molecule by calculating

the time it spends in the bound and unbound states as shown in Figure C3 (a) and (b). We used the residence time of the protein in the bound and unbound states to estimate the association and dissociation kinetics of the interaction of HSA with tolbutamide. Residence times of the HSA molecule in the bound and unbound states are shown in Figure C3(a) and (b) respectively as obtained from Figure C2(a).

Our single molecule approach reveals that the residence time of the HSA molecule in the bound state has a double exponential behavior with decay rate constants η_1 and η_2 of 1.317 s^{-1} and 0.1251 s^{-1}. The residence time of HSA molecule in the unbound state was also best fit by a double exponential equation having decay rate constants $\lambda_1 = 3.052s^{-1}$ and $\lambda_2 = 0.1018s^{-1}$. Although multistage kinetics have been observed in past single molecule fluorescence based studies, we show them here for a single HSA kinetics but without labeling or tethering. The association and dissociation rate constants of the reaction as described in Eqn. C.1 are given by $k_a = \lambda_1/[L]$ and $k_d = \eta_1$; hence the dissociation constant, K_D, of the interaction is 13 μM, which falls within the 4.5 μM - 31.25 μM range reported in the literature.

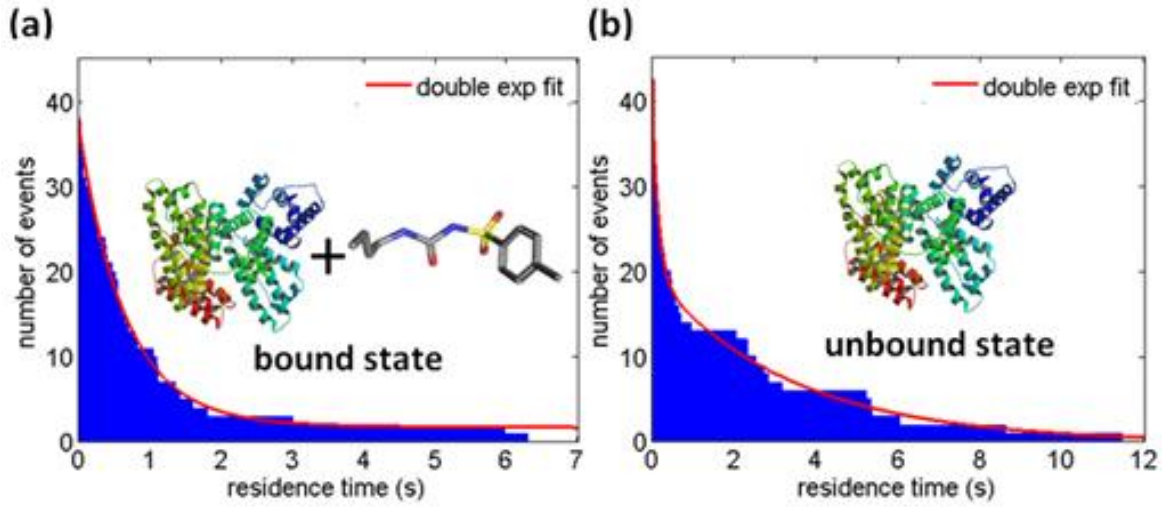

Figure C.3: (a),(b) Histograms of residence times of HSA molecule in the bound and unbound states respectively as obtained from the signal of a trapped HSA molecule with tolbutamide in Figure 2 (a).

We also considered the interaction of HSA with phenytoin. Typical time traces of the interaction of HSA with phenytoin are shown in the Supporting Information (Figure CS2). It is clear that the time traces of the HSA-phenytoin complex show faster binding-unbinding dynamics as compared with the HSA-tolbutamide complex. This is attributed to the fact that phenytoin is relatively more loosely bound to HSA than tolbutamide. Assuming that the HSAphenytion interaction follows Eqn. C.1, we performed similar analysis to that used for tolbutamide. Figures C.4 (a) and (b) show the histograms of the residence times of the HSA molecule in the bound and unbound states with respective decay rate constants of $\eta_1 = 1.795\ s^{-1}$ and $\lambda_1 = 0.5686\ s^{-1}$; hence giving a dissociation constant $K_D = 94.7\ \mu$M. This dissociation constant falls within the 71.43 μM - 111 μM range reported in the literature.

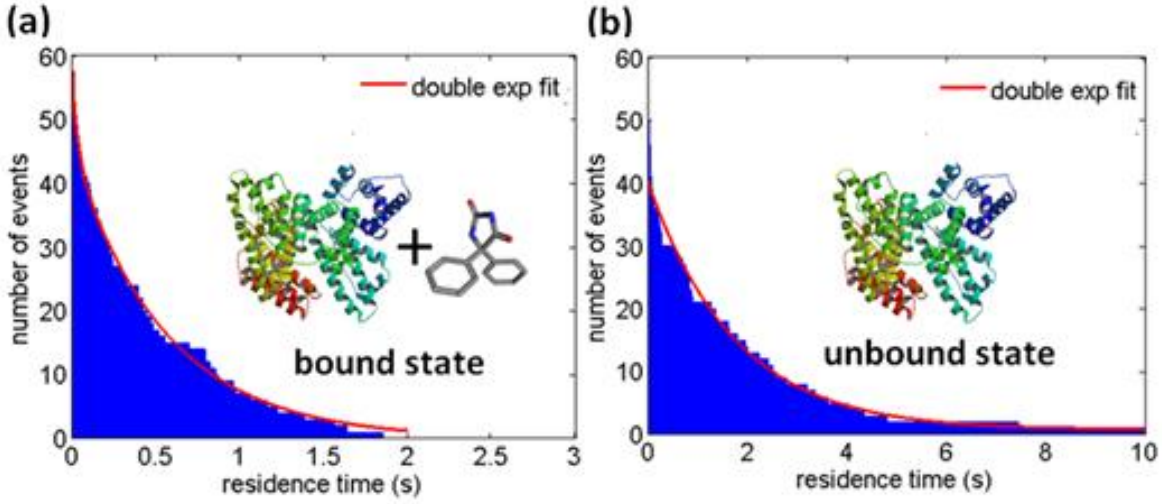

Figure C.4: (a),(b) Histograms of residence times of HSA molecule in the bound and unbound states respectively as obtained from the signal of a trapped HSA molecule with phenytoin.

Our aim in this current study has been to study PSMIs using the DNH trapping approach. Our work on HSA interaction with two ligands, i.e. tolbutamide and phenytoin, show that it is possible to measure the binding kinetics of biological interactions using the DNH trapping method. Unlike other methods which use teth-

ering or labeling the molecules of interest, our approach uses light to hold on to the molecule of interest and thus allows the molecule to be in its native state. For trapping particles in the Rayleigh regime the gradient force scales with the third power of the particle size. However, considering Stokes drag force in liquid environment, which scales linearly with the particle size adds an additional dependence on size; and hence the power required for trapping a particle against Brownian motion scales with the inverse fourth power of the particle size. In addition, the optical power scattered by a particle in the Rayleigh regime has a square power dependence on the polarizability of the particle. Therefore, when a protein in the DNH aperture gets bound to a ligand it experiences conformal changes due to protein binding which result in higher polairzability of the molecule in the bound state and hence higher transmission. In order to investigate the effect of the DNH aperture resonance on the transmission, we preformed transmission spectrum measurements as well as finite-difference time-domain (FDTD) simulation on the DNH aperture which showed that the main transmission peak is at 805 nm, slightly shorter than the 820 nm trapping laser beam see Figure CS3 in Supporting Information.

One of the critical components in our analysis of binding kinetics is the determination of the threshold level between the bound and unbound states. In our current study the threshold level is determined by the mean value of the time traces of the HSA-ligand complex, i.e. the red dotted line, as seen in Figure C.2 (b). We investigated the effect of varying the threshold level on the dissociation constant of the interaction of HSA protein with the ligand. Our results show that there is a range of threshold level values below and above the mean level in which KD values remain within 20% of our reported values. However, the percentage variation in K_D increases dramatically as the threshold level is extended outside the tolerance window see Figure CS4 in Supporting Information. The high sensitivity of our system makes it

possible to detect intermolecular interactions and characterize them by studying the effect they have on the transmitted light through the DNH aperture. Similar effects were not present when trapping a bare HSA molecule (Figure C2 (a)), which shows that the fluctuations present in the signal for the protein-ligand complexes were because of changes to the protein due to binding and unbinding events with the ligand. In addition, this variation in light transmission is not expected to be due to trapping of two HSA molecules in the DNH aperture because such events would induce a two-step increase in the transmission through the aperture, as we reported in an earlier study and as reported by other groups, and we have not observed such behavior in our current study. Furthermore, steric hindrance as well as HSAs negative charge (i.e. like charge repulsion) prevent two or more HSA molecules from getting trapped in the DNH aperture. Therefore, our system allows for working at the single molecule level and hence it can provide information about single molecule interactions, which are not accessible by ensemble methods, such as showing the bi-exponential kinetics.

Residence time histograms of the data obtained from the time traces of the interaction of HSA with tolbutamide and with phenytoin are both better fitted by double exponential fits. However, in order to determine the appropriateness of the single and double fit functions used in our binding kinetics analysis we preformed goodness of fit analysis using the gof() Matlab function. For example, in the case of the interaction of HSA with tolbutamide, goodness of fit analysis revealed a 7% fit improvement from a single to a double exponential function for the bound state and a 4% fit improvement for the unbound state see Figure CS5 in Supporting Information. This indicates that there is an improvement in the fit by using a double exponential function for the unbound state, however, this improvement is only 4% which suggests that it might be possible to fit the unbound state with a single exponential function. In addition, the fast decay rate observed in Figure C.3 (b) (see also Figure CS5(b) in

Supporting Information) is likely the result of noise giving spuriously short vacancy times, especially when the signal crosses the threshold value. We have investigated this spurious effect on simulated data with random noise added to verify that this is indeed a possible explanation (see Supporting Information); however, in the present study we have not discriminated against these short events. Although a number of single-molecule binding studies have reported similar biexponential behavior, these were carried out either with tethering or with labels. This usually alters the natural state of the protein and can introduce complications: for example, in the case of fluorescence labeling, photobleaching can affect the accuracy of determining single molecule residence time. Our approach does not only eliminate the time and cost related to labeling or tethering but it also allows binding partners to be monitored in their native states without additional ligands all at the single molecule level. In addition, the DNH system is well suited for studying PSMIs because it uses low optical powers and the temperature rise at the trapping site is expected to be on the order of 0.1K.

Although our current study only considered the interactions of affinity pairs which have dissociation constants in the μM range, it would be interesting to study a broader range of affinity pairs where the effects of multiple binding sites are taken into account and higher order transitions are considered. We are also planning on integrating our DNH trap on the end of an optical fiber, which will have a number of advantages including reducing the cost of the system by removing the need for a microscope setup, and increasing its robustness by eliminating the vulnerability to beam misalignment, hence saving time. It is also interesting to see how scalable our approach is for multiplexed screening. This will potentially enable us to isolate (multiple) individual proteins from an ensemble and translate them once trapped to different solutions for further studies.

In summary, we have shown that our DNH optical trap approach can potentially provide an alternative platform for studying intermolecular interactions in a free-solution, label-free environment at the single molecule level. In addition, we have shown that binding events can be detected by identifying the conformal changes a ligand makes on the target protein molecule; and hence molecular interactions can be studied by using an intrinsic signal other than refractive index change, as in back scattering infererometery, or temperature, as in isothermal calorimetery. The potential low-cost, robustness and scalability features of our system makes it attractive for future PSMI studies and for drug discovery applications.

C.3 Methods

C.3.1 Fabrication of DNH

We used a Hitachi FB-2100 focused ion beam to mill the DNH in 100 nm thick Au film on a glass substrate with a 5 nm Ti adhesion layer (EMF Corporation). The structure was fabricated at a magnification of 80,000 with the accelerating voltage and current of the gallium ion beam being 40 kV and 0.001 nA.

C.3.2 Gold sample preparation

A gold film sample, which contains the DNH as described above, was washed with acetone, rinsed with isopropanol and dried with nitrogen. An imaging spacer (Sigma Aldrich, GBL654002) is placed on cover glass no. 0 (Goldseal, Ted Pella, inc.), which forms the microwell. 150 L of the protein solution was pipetted into the chamber and then the gold sample (with the gold side facing down) was placed on the imaging spacer to seal the well. The whole sample assembly was then mounted in the trapping setup as shown in Figure C.1(a).

C.4 Supporting Information

C.4.1 Time Traces of a Bare HSA in the DNH

Figure C.5 shows typical time traces of a bare HSA molecule in the DNH aperture. Data is normalized to its mean value. It is clear that time traces of the interaction of HSA with tolbutamide (Figure C.2 (a)) and with phenytoin (Figure C.6) show stronger changes as compared with signal of a bare HSA molecule.

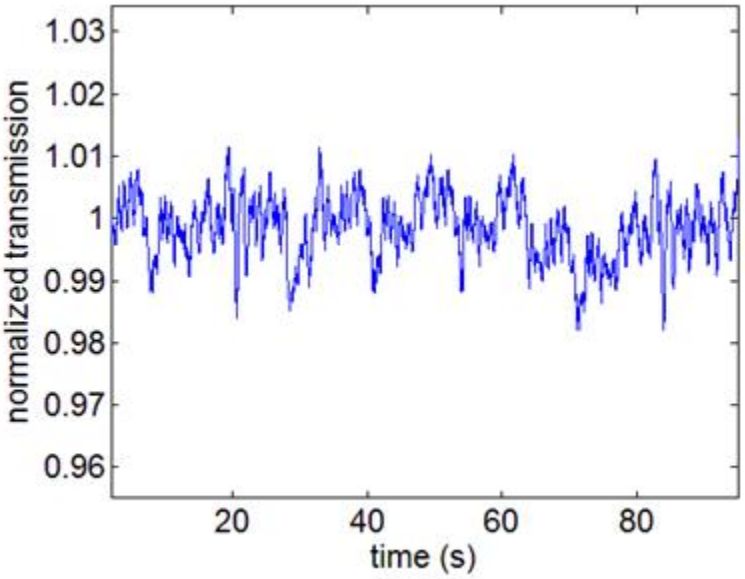

Figure C.5: Time traces of a single HSA molecule in the DNH aperture

C.4.2 Time Traces of HSA Interaction with Phenytoin

Figure C.6 shows typical time traces of the interaction of HSA with phenytoin showing significantly larger fluctuations than HSA alone.

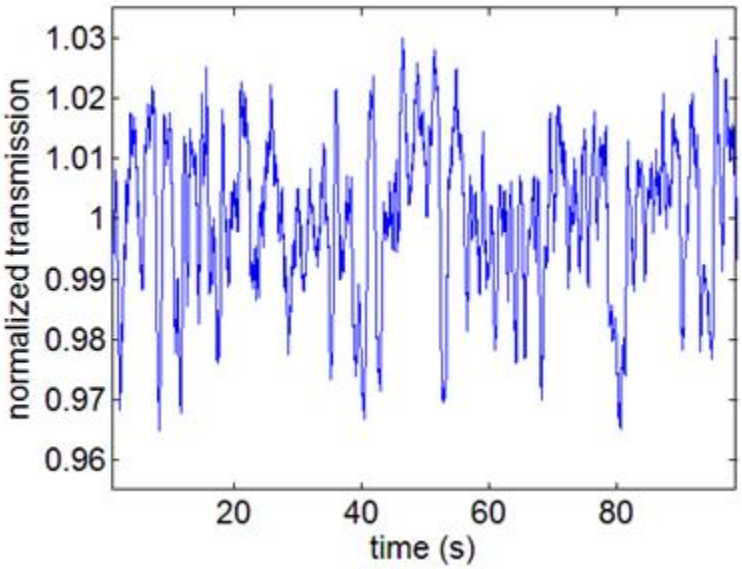

Figure C.6: Time traces of the interaction of the HSA with phenytoin

C.4.3 Transmission spectrum of the DNH aperture

Experimental measurements

Figure CS3 shows the transmission spectrum of the DNH aperture with the main transmission peak at 805 nm, slightly shorter than the 820 nm trapping laser beam. The optical transmission measurements were taken on an Olympus inverted microscope setup. An acousto-optic tunable filter (AOTF) was used to filter the supercontinuum laser source (Fianium, SC400-4W). The output of the AOTF was focused on the sample which contains the DNH using a 100 microscope objective with a 0.9 numerical aperture. The electric field of the beam was aligned along the two close tips of the DNH aperture. The transmitted light through the DNH aperture was collected using a 20 microscope objective with a numerical aperture of 0.45, and measured by a CCD camera (Allied Vision Technologies, Model: GC660).

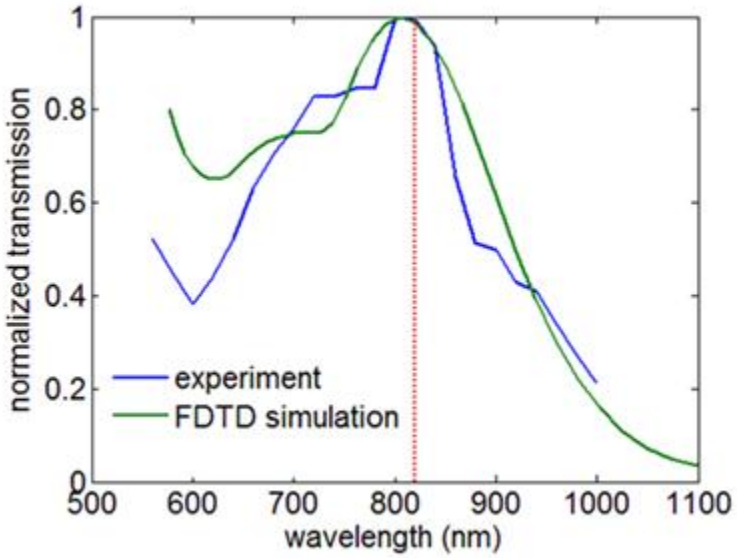

Figure C.7: Experiment and FDTD simulation transmission spectra of the DNH aperture.

FDTD Simulations

We preformed finite-difference time-domain (FDTD) simulation (Lumerical FDTD 8.1) of the transmission through the DNH aperture. The SEM image of DNH structure was imported to the simulation software layout environment. We used a total-field scattered-field source and the 3D simulation region was enclosed with perfectly-matched-layer (PML) boundaries. The permittivity of Au was taken from Johnson and Christy,1 and the refractive indices for the glass substrate and water were set to be 1.5 and 1.33 respectively.

C.4.4 Varying Threshold Level Tolerance

In our current study the boundary between the bound and unbound states is set by the mean of the time traces of the interaction of HSA with the ligand. However, we preformed dissociation constant percentage variation analysis to investigate the vulnerability of our approach to errors due to varying threshold levels. It is clear from

Figure C.8 that there is a threshold level range in which the percentage variation in the dissociation constant fall within 20% of the value obtained at the default mean level.

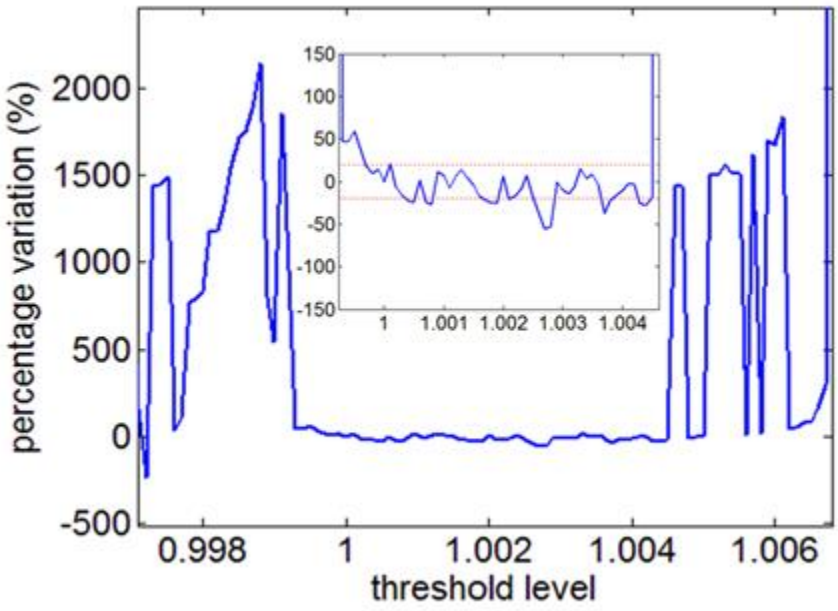

Figure C.8: Dissociation constant percentage variation with varying threshold level for the interaction of HSA with tolbutamide, with the horizontal red dotted lines corresponding to ±20% percentage variation levels.

C.4.5 Goodness of fit

Figure CS5 shows the bound and unbound residence time histograms of the interaction of HSA with tolbutamide. We used goodness of fit analysis to evaluate the appropriateness of single and double fit functions used in our binding kinetic analysis. Goodness of fit analysis revealed a 7% fit improvement from a single to a double exponential function for the bound state and a 4% fit improvement from a single to a double exponential fit for the unbound state.

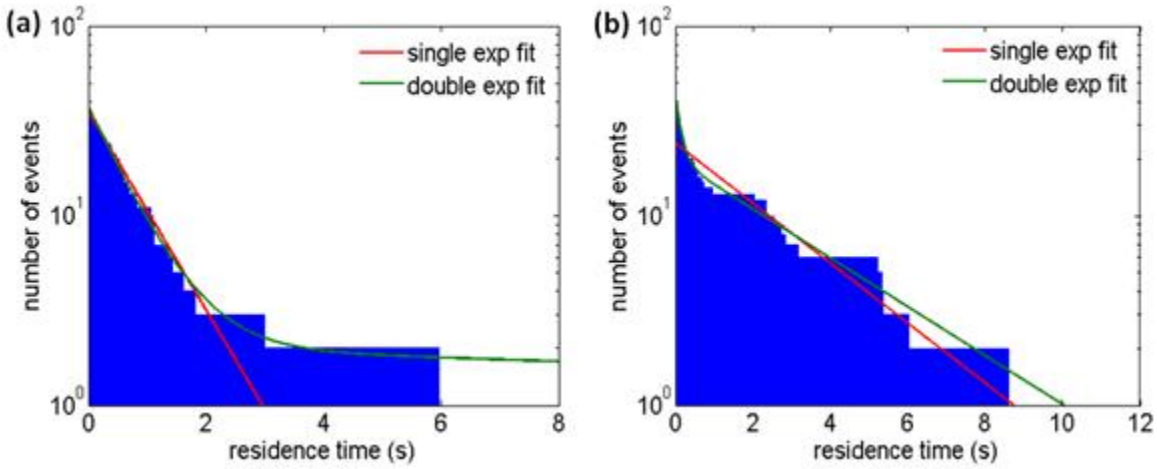

Figure C.9: Histograms of residence times of HSA molecule in the bound (a) and unbound (b) states respectively as obtained from the signal of a trapped HSA molecule with tolbutamide in Figure C2 (a).

C.4.6 Effect of Noise on Decay Rate Constants

Figure C.10 shows the effect of noise on simulated data. It is clear that the presence of noise in the data introduces spurious errors which might explain the fast decay rates observed in the unbound states in our study. Goodness of fit analysis on the simulated data without noise reveal that there is an almost negligible fit improvement from a single to double exponential function with only 0.7% improvement for the residence time of the signal above the 1 V mean value, and 0.2% improvement for the residence time of the signal below the mean value. As for the simulated data with random noise added, there is a 5% fit improvement from a single to a double exponential function for the residence time of the signal above the mean value and a 3% fit improvement from a single to a double exponential function for the residence time of the signal below the mean value.

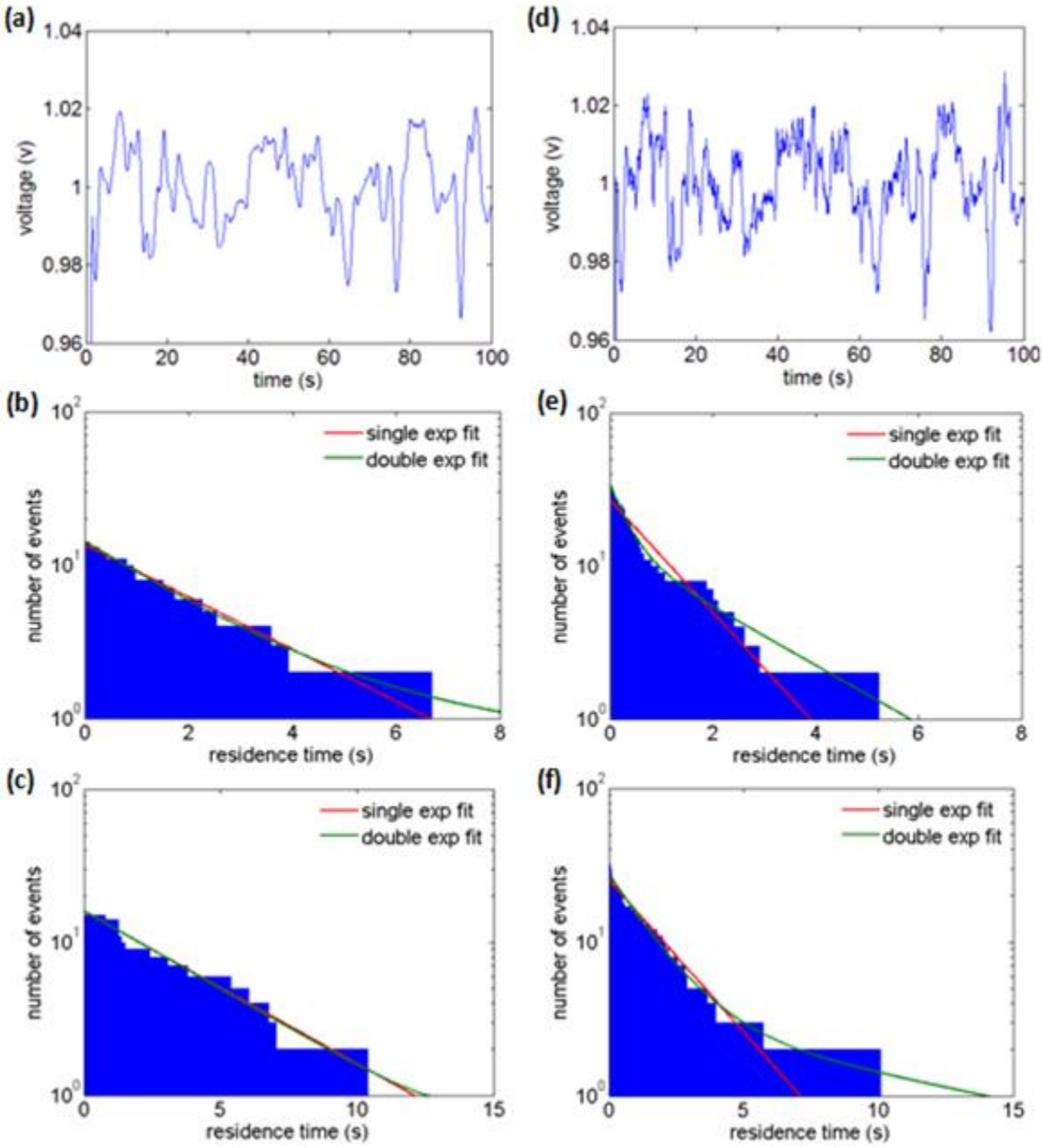

Figure C.10: Effect of noise on decay constants. (a) Simulated data. (b),(c) Histograms of residence time of data in (a) above and below mean voltage level of 1 V. (d) Simulated data in (a) with random noise added. (e),(f) Histograms of residence time of data in (a) above and below mean voltage level of 1 V.

Appendix D

Raman Spectroscopy of Single Nanoparticles in a double-nanohole optical tweezer system

Originally published:

Steven Jones, Ahmed A. Al Balushi, and Reuven Gordon, Raman spectroscopy of single nanoparticles in a double-nanohole optical tweezer system, Journal of Optics 17, 102001 (2015).

D.1 Abstract

A double nanohole in a metal film was used to trap nanoparticles (20 nm diameter) and simultaneously record their Raman spectrum using the trapping laser as the excitation source. This allowed for the identification of characteristic Stokes lines for

titania and polystyrene nanoparticles, showing the capability for material identification of nanoparticles once trapped. Increased Raman signal was observed for the trapping of multiple nanoparticles. This system combines the benefits of nanoparticle isolation and manipulation with unique identification.

D.2 Paper Content

The first demonstrations of gradient force optical tweezers recognized the limitation of trapping objects smaller than 100 nm due to the requirement for large optical intensities. Many nanophotonic and nanoplasmonic approaches have been used to achieve trapping of nanoparticles with subwavelength confined optical fields. In 2009, a circular nanohole in a metal film was used to trap 50 nm dielectric particles with low optical power. That work used the strong influence of the apertures transmission due to dielectric loading to achieve efficient trapping.

Several works have developed shaped nanoapertures to achieve trapping of even smaller nanoparticles. Double nanoholes (DNHs) that strongly confine the electromagnetic field at the cusps where the holes overlap have been used for trapping (and unfolding) a single protein, a 12 nm silica sphere, and a single DNA molecule. Rectangular nanoholes have trapped 22 nm polystyrene particles. Similar to the DNH, the bowtie nanohole has been fabricated on the end of a tapered optical fiber, allowing for not only the trapping but also the translation of 50 nm fluorescent beads. Apertures for trapping have also been integrated on other near-field fiber probes as well as cleaved optical fibers. A recent work has used the bowtie nanoholes to isolate quantum dots and excite them with two-photon luminescence. While these works illustrate the potential of nanoapertures to isolate nanoparticles and manipulate them, it is of considerable interest to identify the trapped nanoparticle. Recently, we have

developed an approach to excite the vibrational modes of the trapped nanoparticles, proteins and DNA in the low-wavenumber regime. This requires multiple trapping lasers and so far has only been demonstrated for extremely low frequency vibrational modes that probe the nanoparticle size, shape and mechanical properties. To achieve conventional Raman spectra for the identification of the trapped nanoparticle material, here we integrate a Raman spectroscopy setup with our DNH tweezer system. A recent report showed multiple polystyrene nanoparticles (on the order of 100) detected with Raman using a nanohole. Other groups have shown conventional Raman spectroscopy of single trapped nanowires using optoelectronic tweezers; however, this method is limited to relatively large particles, typically on the order of several microns in length. Here we demonstrate single nanoparticle sensitivity to achieve characteristic Raman peaks for titania and polystyrene nanoparticles. This combines surface enhanced Raman spectroscopy, which has enabled single molecule sensitivity, with nanohole optical tweezers for the isolation and manipulation of nanoparticles.

Figure D.1(a) shows a schematic of the optical tweezer system with integrated Raman detection. While similar to our past works there are notable differences in this setup: it uses a 671 nm solid state laser (Laserglow, LRS-0671-TSM-00200-10; 100 mW, reduced to around 10mW at the nanoaperture due to filters) with a notch filter (Semrock, LL01-671) and a high-pass dichroic (Semrock, FF685-Di02) to isolate the Rayleigh line from the detected Raman spectra. The Raman spectrum was recorded in the reflection path by collecting with a broad area optical fiber and a cooled CCD spectrometer (Ocean Optics, QE Pro).

Figure D.1(b) shows a scanning electron microscope image of a typical DNH used in the setup. The gap sizes were slightly larger than 20 nm to allow for trapping of 20 nm particles without steric hindrance (although gaps down below 10 nm have been achieved in the past). Figure D.1(c) shows the transmission through the aper-

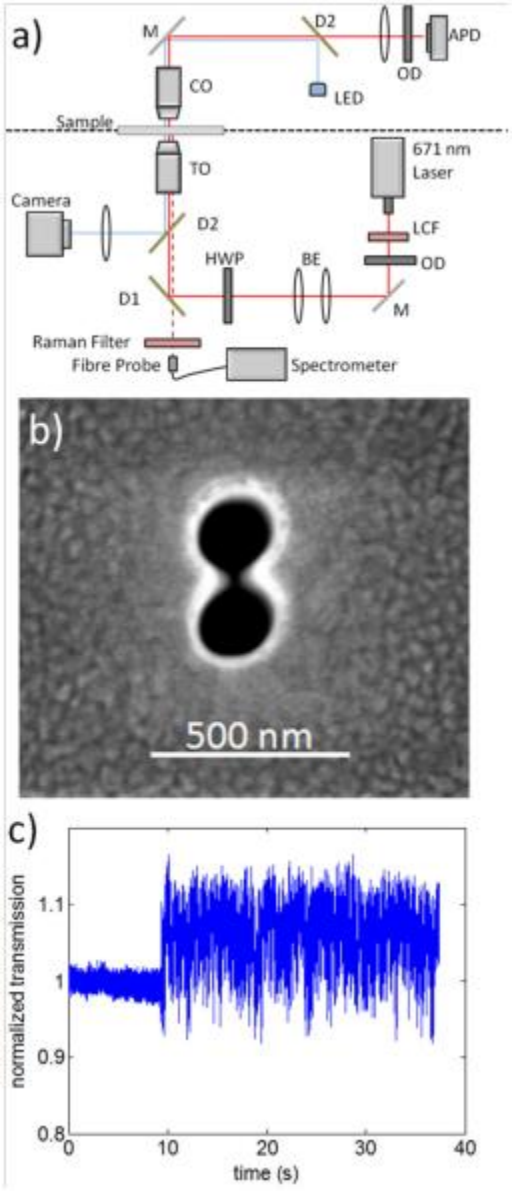

Figure D.1: (a) Schematic of the trapping setup used to obtain single nanoparticle Raman spectra. APDavalanche photodiode; BEbeam expander; CO10x condenser objective; D1685 nm long pass dichroic; D2650 nm long pass dichroic; HWPhalf wave plate; LCFlaser clean-up filter; Msilvered mirror; ODoptical density filter; TO50x trapping objective. (b) Scanning electron microscope image of the double nanohole aperture used in trapping. (c) Characteristic single particle trapping event (polystyrene)

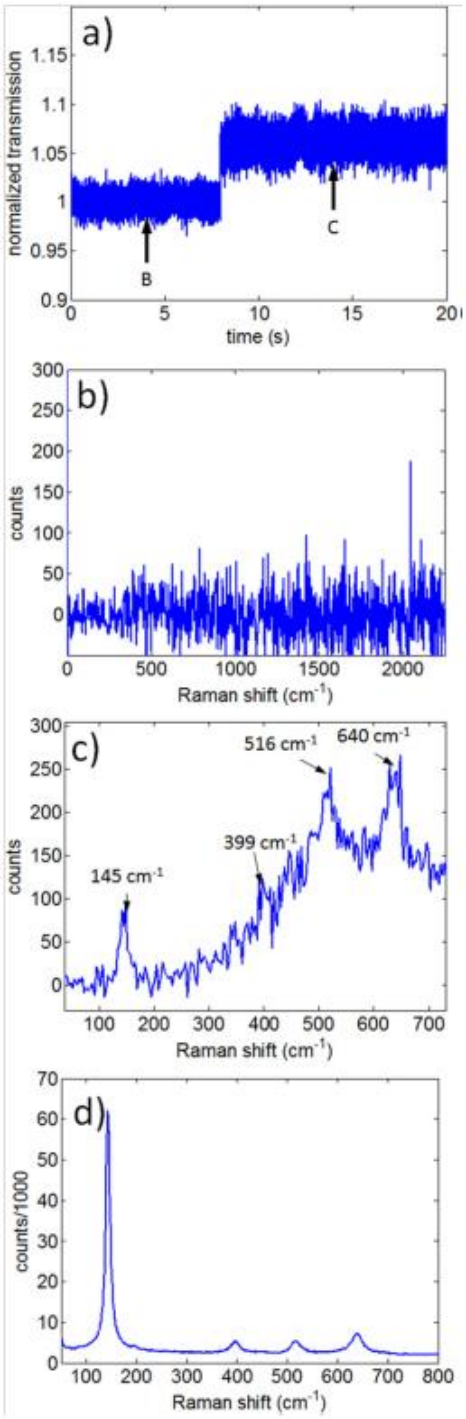

Figure D.2: (a) Trapping event of 20 nm titania used for obtainingRaman spectrum, B is the untrapped state and C is the trapped state. The Raman spectra in the (b) untrapped and (c) trapped states (5 min integration time each). The Raman spectra for a bulk 20 nm titania solution is shown in (d) as a reference.

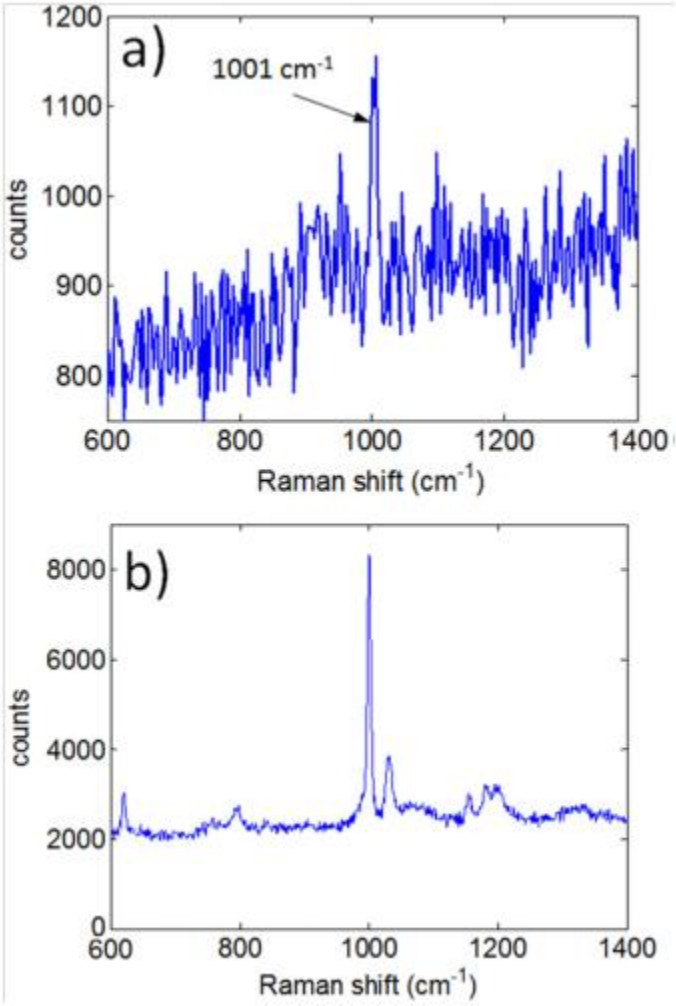

Figure D.3: (a) Raman spectra of trapped 20 nm polystyrene particle (5 min integration time). The Raman spectra for a bulk 20 nm polystyrene solution is shown in (b) as a reference.

ture with a characteristic step increase when a particle is trapped in the aperture. The transmission is normalized to the mean value before trapping. There is also an increase in the fluctuations of the transmitted power which is due to the motion of the particle in the trap. We have used this in the past to characterize the strength of the optical tweezer as well as identify the size of proteins. Typically, the initial trapping event will occur anywhere from several minutes to a few hours after the system has been setup and stabilized. The ease at which trapping occurs is highly particle

dependent, with titania showing a greater trapping affinity as a result of its higher relative permittivity. Once trapped the particle remained in the trapped state for a minimum of 5 min, with no additional trapping events during the period in which the Raman spectra is recorded.

Figure D.2(a) shows a trapping event for a 21 nm titania nanoparticles (Sigma: 718467- 00G). Prior to trapping, the Raman spectrum (background subtracted) shows no peaks, as seen in figure D.2(b). After trapping, there is a Stokes peak at 145, 399, 516 and 640 cm^1 (figure D.1(c)), which agree well with the Stokes peaks observed for a bulk 21 nm titania solution observed with the Renishaw inVia confocal Raman microscope system using a 785 nm excitation laser (figure D2(d)), and as previously reported. Note that the attenuation of Raman peaks from 0 to 500 cm^1 is expected in the trapping setup, due to the band edge of the dichroic filter. There also appears to be a fluorescence background from the titania nanoparticle.

To show that this configuration can be used to identify different nanoparticles, we repeated the experiment for 20 nm polystyrene spheres (Thermo Scientific, 3020A). The trapping event for polystyrene is shown in figure D1(c) and the corresponding Raman spectrum is shown in figure D.3(a). The main peak for polystyrene at 1001 cm^1 is clearly seen. Additional Stokes peaks were too small to be observed, which is expected for polystyrene (the next largest peak in the detection range is around 4 times smaller as seen in figure D.3(b) also obtained with the Renishaw inVia system). Typically, the signal to noise ratio of the Raman spectra in the single-particle trapped state is on the order of 5x the local background signal, which is above the limit of detection. This is limited by the fluorescent background as well as the ability to maintain a single particle trapped during the data acquisition.

In some cases, trapping of multiple particles was observed by multiple steps in the transmission time series (figure D.4(b)). In these cases, the Raman spectrum also

showed an increase, approximately doubling for the second particle. Repeated measurements showed the same results for both the titania and polystyrene nanoparticles (in particular, the titania results have been reproduced for more than 20 trapping events).

DNHs also have the advantage of rapidly dissipating heat away from the nanohole. It has been predicted that the heating of nanoholes is over three orders of magnitude lower than a corresponding nanoparticle (for the same local field intensity) due to the high thermal conductivity of the surrounding gold film. In the future, it may be possible to quantify the heating by comparing Stokes and anti-Stokes lines. This will require modifying the setup with a band stop filter that is not possible in the current configuration.

In conclusion, we have demonstrated the ability to record the Raman spectra of individual and multiple nanoparticles in a DNH laser tweezer system. This allows for identifying the nanoparticle trapped for further investigation. This work may be used to study the characteristics of nanoparticles already investigated with the nanohole tweezers, such as quantum dots, proteins, DNA, and viruses. Such identification capability will allow operation in heterogeneous solutions. The Raman spectra also allows the potential of analyzing material changes due to interactions (e.g., chemical reactions, binding, strain), as well as probe the local temperature in the aperture.

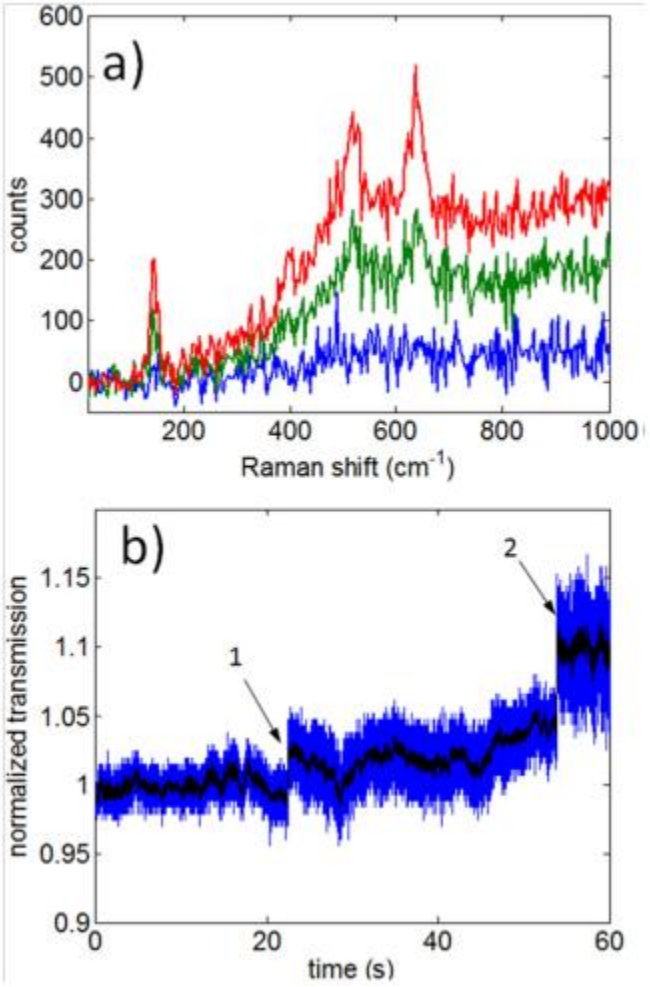

Figure D.4: (a) Raman spectra of titania nanoparticles for multiple trapping events. The Raman spectra of the untrapped state is shown in blue, the first trapped state in green, and the second trapped state in red. (b) Time series illustrating trapping events 1 and 2, the black line is a filtered time series to better illustrate the stepped transmission increases at discrete times (in contrast to slower drift variations).

Appendix E

Nanoscale volume confinement and fluorescence enhancement with double nanohole aperture

Originally published:

R. Regmi, A. A. Al Balushi, H. Rigneault, R. Gordon, J. Wenger, "Nanoscale volume confinement and fluorescence enhancement with double nanohole aperture," Scientific Reports 5, 15852 (2015).

E.1 Abstract

Diffraction ultimately limits the fluorescence collected from a single molecule, and sets an upper limit to the maximum concentration to isolate a single molecule in the detection volume. To overcome these limitations, we introduce here the use

of a double nanohole structure with 25 nm gap, and report enhanced detection of single fluorescent molecules in concentrated solutions exceeding 20 micromolar. The nanometer gap concentrates the light into an apex volume down to 70 zeptoliter (10^{21} L), 7000-fold below the diffraction-limited confocal volume. Using fluorescence correlation spectroscopy and time-correlated photon counting, we measure fluorescence enhancement up to 100-fold, together with local density of optical states (LDOS) enhancement of 30-fold. The distinctive features of double nanoholes combining high local field enhancement, efficient background screening and relative nanofabrication simplicity offer new strategies for real time investigation of biochemical events with single molecule resolution at high concentrations.

E.2 Paper Content

E.2.1 Introduction

Plasmonic nanoantennas realize a new paradigm to concentrate light energy into nanoscale dimensions, enhance the luminescence of quantum emitters and trap single nano-objects. To overcome the diffraction limit, nanoantenna designs take advantage of sharp curvature radii, nanoscale gaps and plasmonic resonances, using metal nanoparticles, nanorods, dimer gap antennas or bowtie antennas.

The enhanced detection of single fluorescent molecules in concentrated solutions is an emerging field of application for plasmonic antennas. Transient interactions between proteins, nucleic acids, and enzymes typically occur at micromolar concentrations, however single-molecule diffraction-limited confocal techniques are restricted to concentrations in the pico to nanomolar range due to femtoliter detection volumes. Reaching single molecule sensitivity at the physiologically relevant micromolar concentrations thus requires over three orders of magnitude reduction in the detection

volume. Sub-wavelength nanoapertures milled into optically thick metal layers (also called "zero-mode waveguides") concentrate light at the bottom of the apertures, constraining the detection volume to the attoliter range. However, the fluorescence enhancement with single circular nanoapertures is limited around typically ten-fold and the signal-to-noise ratio rapidly deteriorates when the aperture diameter goes below 100 nm. To get higher volume confinement and fluorescence enhancement factors, we have recently developed the "antenna-in-box" design combining a resonant gap antenna into a rectangular nanoaperture. Experimentally, this design provides fluorescence enhancement up to several hundred folds while the detection volume is confined in the range 70-100 zeptoliter (1 zL = 10^{-21} L). However, the fabrication of this structure remains quite demanding due to the complex shape of the antenna. Moreover, even for 80 nm particle antenna-in-box, the resonances are typically in the range 700-800 nm, away from the emission bands of the most common fluorescent dyes.

As alternative plasmonic antenna design, the double nanohole (DNH) structure milled into a metal film has recently attracted much interest to realize an efficient platform to trap single nano-objects down to the ultimate single protein level. The DNH design has a distinctive set of advantages: (i) the apex between the two holes directly realizes sharp radii of curvatures and nanometer gap sizes, providing high local intensity enhancement, (ii) the optically thick metal film efficiently screens out the background from the solution around the structure, (iii) heating effects are avoided thanks to the good thermal conductivity of the gold film, and (iv) the structure remains relatively simple to fabricate as compared to bowtie antenna, bowtie aperture or antenna-in-box. These specific features make DNH highly relevant to enhance the detection of fluorescent molecules in concentrated solutions. Moreover, the quantification of the fluorescence enhancement factor in DNH is interesting for

plasmon-enhanced luminescence applications, and the measurement of the apex near-field volume is important to better understand the phenomenon leading to enhanced plasmonic trapping in DNH.

Here we use double nanohole structure with 25 nm gap to enhance the detection of single fluorescent molecules in solutions up to 20 μM concentration (Fig. E.1a). Using fluorescence correlation spectroscopy (FCS), we measure the near-field apex volume to 70 zeptoliter, realizing a volume reduction of 7000-fold as compared to diffraction-limited confocal setups. This high intensity confinement goes with fluorescence enhancement up to 100-fold, together with microsecond transit time and single molecule sensitivity at concentrations exceeding 20 micromolar. We also conclusively demonstrate the acceleration of the fluorescence photodynamics in the nanometer apex region, and report experimentally 30-fold enhancement of the local density of optical states (LDOS), in good agreement with numerical simulations. In all the experiments, the polarization-dependent response ensures that the relevant signal stems from the nanoscale apex area, and not from the surrounding holes . The cutting-edge optical performance, the relative ease of nanofabrication and the efficient background screening make the DNH structure ideal to study complex biochemical dynamics at physiological concentrations.

E.2.2 Results: zeptoliter volume with 100-fold fluorescence enhancement

The DNH structure is realized by focused ion beam milling of two 190 nm diameter nanoholes connected by an apex region of 60 nm length and 25 nm gap width (Fig. E.1d). The DNH bears a clear polarization dependence (Fig. E.1b,c): when the incoming light polarization is oriented parallel to the apex between the nanoholes, light is mainly concentrated in the gap region. Conversely, when the incoming light

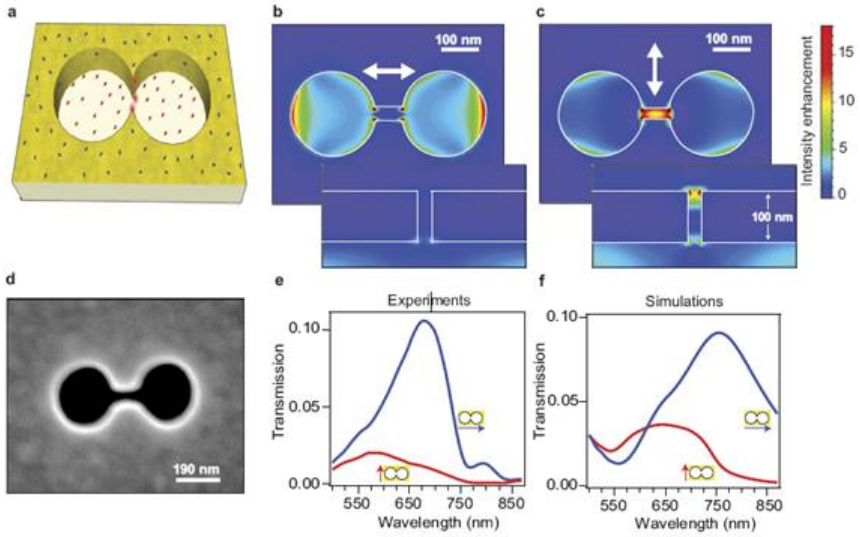

Figure E.1: (a) Sketch of double nanohole (DNH) structure to enhance single molecule fluorescence in the apex region. (b,c) Local intensity enhancement (linear scale) for a DNH of 25 nm gap and 190 nm diameter excited at 633 nm with a linear polarization perpendicular (b) and parallel (c) to the apex between the holes, taken in a plane 5 nm below the top metal surface. The inserts show the intensity enhancement along a vertical cut in the DNH center. All images share the same colorscale. (d) Scanning electron microscope image of the structure milled in 100 nm thick gold film using focused ion beam. (e) Experimental and (f) simulated transmission spectra for a DNH illuminated with normal incidence for two orthogonal linear polarizations along the apex (red) and perpendicular to the apex (blue).

polarization is oriented perpendicular to the apex, there is a minimum intensity in the gap as light is mainly concentrated in the nanohole region. This behavior is confirmed by recording far-field transmission spectra using polarized illumination (Fig. E.1e,f). When the orientation is set parallel to the apex, a minimum of transmission is found as the electromagnetic intensity is concentrated in the gap, whereas a maximum transmission is obtained for a polarization oriented perpendicular to the apex. These findings are well reproduced by FDTD numerical simulations of the transmission spectra (Fig. E.1f). Moreover, the recorded spectra show that the DNH response covers well the 633 nm laser excitation wavelength and the 650-690 nm fluorescence emission band for the Alexa Fluor 647 dye.

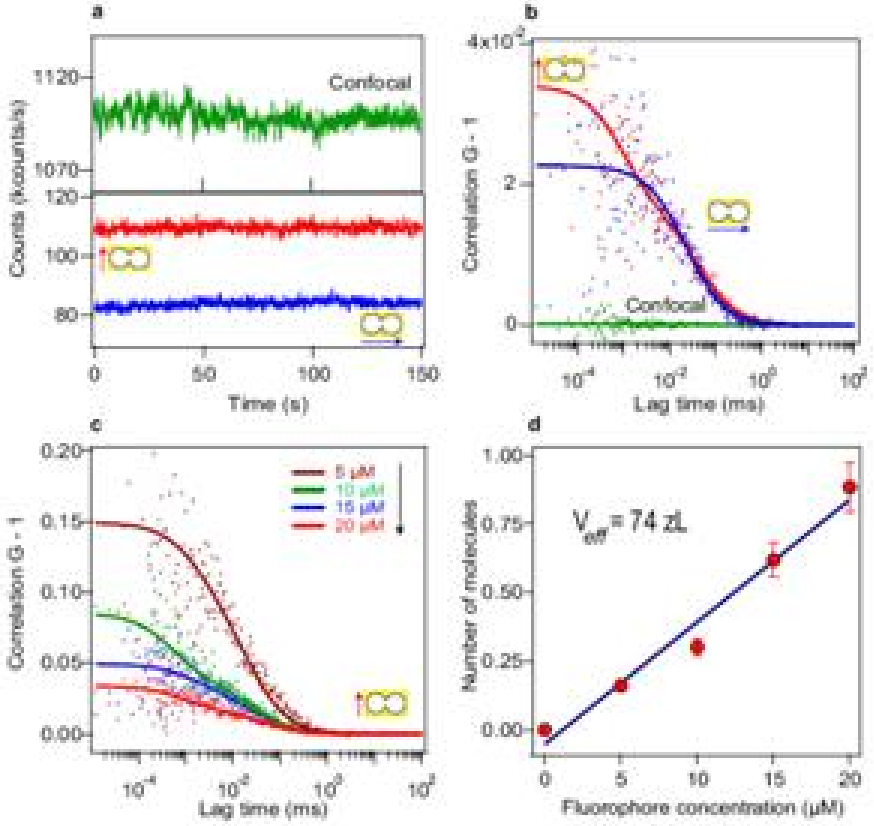

Figure E.2: FCS analysis to measure the near-field apex volume. (a) Fluorescence time trace with excitation light parallel (red line) and perpendicular (blue line) to the apex region. The time trace found for the confocal case (0.5 fL diffraction-limited volume) is shown in green for comparison. (b) FCS correlation function of the traces shown in (a). For all cases, the Alexa Fluor 647 concentration 20 μM with 200 mM of methylviologen as chemical quencher, and the excitation power is 10 μW. Dots are experimental points, lines are fits using the model described in the Methods section. A higher correlation amplitude is observed with the polarization parallel to the apex, and corresponds to a lower number of detected molecule (stronger confinement of light). The fit parameters are summarized in Table 1. (c) FCS correlation functions for increasing concentrations of fluorescent dyes in a double nanohole with excitation polarization parallel to the apex. (d) Number of detected molecules in the apex region as function of the molecular concentration. The slope of the curve quantifies the apex near-field volume V_{eff}.

For fluorescence experiments, the DNH structure is first cleaned by UV-ozone treatment for 10 minutes to remove organic impurities and render the gold surface hydrophilic. Next, the DNH structure is covered by the solution containing

the fluorescent probe molecules (Alexa Fluor 647 from Invitrogen, Carlsbad, CA) at micromolar concentrations along with 200 mM methyl viologen (1,1'-Dimethyl-4,4'-bipyridinium dichloride, Sigma-Aldrich). The use of methyl viologen quenches the dye quantum yield to 8% and maximizes the fluorescence enhancement. Figure E.2a shows the raw fluorescence intensity traces in a DNH with 20 μM Alexa Fluor 647 and 200 mM methyl viologen. A higher fluorescence intensity is obtained when the excitation polarization is set parallel to the apex region between the double nanohole structure, in accordance with the higher excitation intensity expected from the simulations (Fig. E.1c). To characterize the apex detection volume and the fluorescence enhancement, we perform fluorescence correlation spectroscopy (FCS) analysis and compute the temporal correlation of the intensity traces in (a). The FCS data supports the polarization dependency of the DNH (Fig. E.2b): a high FCS correlation amplitude is found when the excitation is set parallel to the apex region, which relates to a reduced number of molecules within the nanoscale detection volume (the FCS amplitude scales inversely with the number of detected molecules, see Methods section for details). The confocal measurement for the reference solution (without nanostructure) shows comparatively high average fluorescence intensity (green curve in Fig. E.2a) and very weak FCS correlation amplitude (Fig. E.2b). This corresponds to the expected situation that at 20 μM there are about 6200 molecules in the 0.5 fL diffraction-limited confocal detection volume with a low average brightness per molecule (the brightness per molecules in confocal setup is $Q_{sol} = 0.17$ kcounts/s at 10 μW excitation due to the presence of the chemical quencher).

The fitting parameters for the FCS analysis are summarized in Tab. E.1. In the case of excitation polarization parallel to the DNH apex, we obtain an average number of $N^* = 0.9$ molecules in the hot spot with brightness $Q^* = 15.6$ kcounts/s. These values correspond to a fluorescence enhancement of $Q^*/Q_{sol} = 92$, and a hot

spot volume of 74 zL (1 zL = 10^{-21} L), equivalent to a detection volume reduction of $N_{sol}/N^* = 6900$. In addition to the fluorescence enhancement and nanoscale confinement of light, the FCS curves in DNH also show polarization-dependent microsecond residence time in the apex region, which is consistent with the 25 nm gap size and overrule the occurrence of molecular adhesion to the metal surfaces.

	Confocal	**Double nanohole**	
Excitation polarization	Linear	Parallel	Perpendicular
F (kcounts/s)	1090	110	85
G(0)-1	0.16×10^{-3}	34×10^{-3}	22×10^{-3}
N	6200	0.9	46
τ_d (μs)	62	1.2	33
Q (kcounts/s)	0.17	15.6	1.9
Detection volume (zL)	500×10^3	74	4×10^3
Fluorescence enhancement		92	11
Volume reduction		6900	140

Table E.1: Fitting parameter results for the FCS curves obtained on double nanohole (Fig. E.2b). The polarization orientation is respective to the DNH apex. For the DNH-parallel case, the FCS fit considers two species. The number of molecules and diffusion time for the slowly diffusing species (aperture region) are respectively $N_0 = 49$ and $\tau_{d,0} = 33$ μs (see Methods section for details).

To demonstrate the control and reproducibility of our experiments, we conduct a series of FCS measurements with increasing concentrations of fluorescent dye (Fig. E.2c). As expected, the increase in fluorophore concentration results to higher number of molecules within the detection volume and lower amplitude of the correlation curves. The linear relationship between the number of detected molecules (N^*) in the near-field region with the fluorophore concentration confirms the effective detection volume V_{eff} of 74 zL (Fig. E.2d). Remarkably, this volume corresponds very well to the geometrical dimensions of the apex region of $60 \times 25 \times 50$ nm^3 = 75 zL, considering a typical thickness of 50 nm for the intensity profile decaying evanescently inside the DNH obtained from numerical simulations (see Fig. 1c insert).

In Fig. E.3a we vary the excitation power and report the average fluorescence

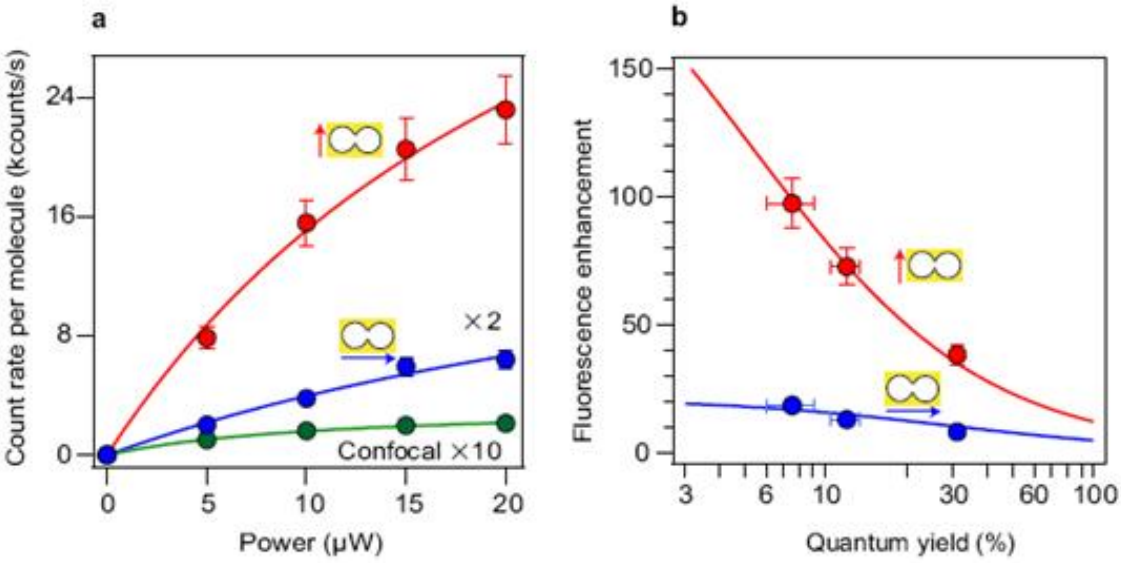

Figure E.3: (a) Fluorescence brightness per molecule versus the excitation power for Alexa Fluor 647 with 200 mM methyl viologen (quantum yield $\sim$ 8%). The data for the double nanohole with perpendicular orientation respective to the apex (blue) and the reference confocal data (green) are multiplied respectively by 2x and 10x. (b) Fluorescence enhancement factors with excitation polarization parallel (red) and perpendicular (blue) respective to the apex. Different concentrations of chemical quencher are used, corresponding to different values of quantum yield in solution: from left to right the data points correspond to methyl viologen concentrations of 200 mM, 80 mM and 0. For (b), the excitation power is 10 μW.

brightness per molecule for both polarization orientations. In the DNH with parallel orientation, count rates per molecule above 20 kcounts/s can be readily obtained, while for the confocal reference the fluorescence brightness saturates to values below 1 kcounts/s in the presence of methyl viologen. The experimental points follow the general model of the fluorescence brightness $AI_e/(1+I_e/I_s)$, where I_e is the excitation power, I_s the saturation power, and A is a constant proportional to the molecular absorption cross-section, quantum yield, and setup collection efficiency.

The effect of the fluorophore's quantum yield is studied using different concentrations of methyl viologen. Figure E.3b summarizes the fluorescence enhancement results for both DNH polarization orientations and the three cases of 200 mM, 80 mM,

and no methyl viologen. The fluorescence enhancement factor increases significantly from 40 to 100× while Alexa Fluor 647 quantum yield is quenched from 30% to 8%. This behavior is well taken into account by a model of the fluorescence enhancement factor η_F as function of the fluorophore's quantum yield in reference solution ϕ:

$$\eta_F = \frac{\eta_{exc}\,\eta_{em}}{(1-\phi)+\phi\zeta} \tag{E.1}$$

where η_{exc} is the excitation intensity enhancement, η_{em} is the radiative rate enhancement times the collection efficiency enhancement, and $\zeta = (\Gamma^*_{rad} + \Gamma^*_{loss})/\Gamma_{rad}$ is a parameter describing the ratio of the radiative rate Γ^*_{rad} and the nonradiative rate to the metal Γ^*_{loss} due to ohmic losses relative to the dye's radiative rate Γ_{rad} in confocal reference. We will show in the next section that ζ is actually equivalent to the enhancement of the local density of optical states (LDOS). Therefore, in the analysis of the data in Fig. E.3b using Eq. (E.1), we set the value of ζ to the LDOS enhancement found experimentally from the fluorescence decay dynamics. As shown in Fig. E.3b, the agreement with the Eq. (E.1) model and the experimental data is excellent for both polarizations. Assuming that $\eta_{exc} \approx \eta_{em}$ and neglecting the gain in collection efficiency, the extrapolation of the data to $\phi \to 0$ indicates a local intensity enhancement of $\eta_{exc} \sim 14$ for parallel and ~ 4 for perpendicular orientation, in good agreement with the numerical simulations in Fig. E.1b,c.

E.2.3 Fluorescence photodynamics acceleration and LDOS enhancement

Time correlated single photon counting (TCSPC) measurements record the fluorescence decay kinetics upon picosecond pulsed excitation. Figure E.4 displays typical decay traces for the confocal reference and the DNH with excitation polarization par-

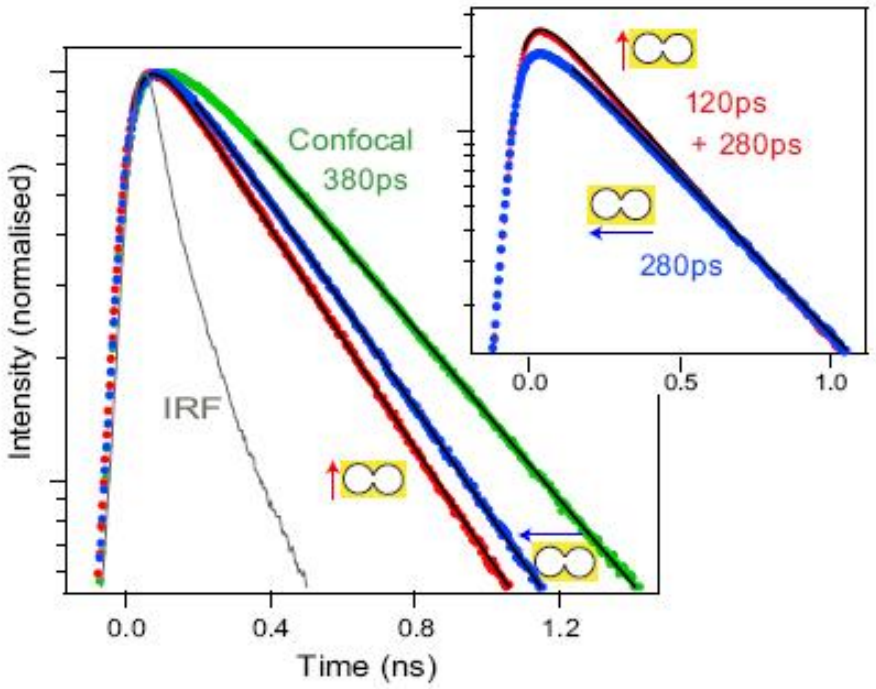

Figure E.4: Amplitude-normalized fluorescence decay traces with excitation light parallel (red line) and perpendicular (blue line) to the apex region. The decay trace with the diffraction-limited volume (green) provides the reference for Alexa Fluor 647 with 200 mM methyl viologen. Black lines are numerical fits used to determine the fluorescence lifetime indicated on the traces. IRF denotes the instrument response function. For a supplementary comparison between parallel and perpendicular cases, the inset displays the traces normalized so that the longer time decay component has a similar amplitude for both cases. The additional short lifetime contribution representative of the apex region clearly emerges when the polarization orientation is parallel to the apex.

allel and perpendicular to the apex. The TCSPC data show clear acceleration of the decay dynamics from confocal to DNH and from perpendicular to parallel orientation. Fitting the TCSPC data with a single exponential model (black lines in Fig. E.4) provides the fluorescence lifetime for the confocal case and DNH with perpendicular orientation. For the DNH with parallel orientation, we use a bi-exponential model to account for the respective contributions of the N^* molecules in the apex region and the N_0 molecules in the nanoholes (outside the gap). For each case, the model takes into

account the temporal resolution of our apparatus by computing the (re)convolution of the exponential decay with the instrument response function (IRF, full width at half maximum 120 ps).

In the presence of 200 mM methyl viologen, the Alexa Fluor 647 fluorescence lifetime becomes 380 ps. For the DNH with perpendicular orientation, the presence of the nanohole further reduces this lifetime to 280 ps (1.35× lifetime reduction), a value that is similar to the lifetime reduction obtained with single gold apertures. For the DNH with parallel orientation, two exponential decays are observed (see insert in Fig. E.4): a fast 120 ps decay corresponding to the N^* molecules in the gap, and a longer 280 ps decay for the N_0 molecules outside the gap. Remarkably, the longer decay time corresponds to the decay time obtained for perpendicular orientation, confirming that the background fluorescence stems mainly from the nanohole region.

With the use of 200 mM methyl viologen, the chemical quenching rate Γ_q represents a large fraction of the total decay rate Γ_{tot} (inverse of fluorescence lifetime). To estimate the LDOS (local density of optical states) enhancement with the DNH, the influence of the chemical quenching rate Γ_q must be taken into account prior to computing the ratio of decay rates. The LDOS encompasses both radiative and non-radiative transitions set by the photonic environment (such as energy transfer to the free electrons in the metal). However, the LDOS is not proportional to the chemical quenching rate set by the presence of methyl viologen. To estimate the amount of decay rate that actually depend on the LDOS, we write the dye total decay rate in the confocal case as $\Gamma_{tot} = \Gamma_{rad} + \Gamma_{nr} + \Gamma_q$, where Γ_{rad} denotes the radiative rate, and Γ_{nr} is the internal non-radiative decay rate. In the presence of the DNH, the decay rate becomes $\Gamma^*_{tot} = \Gamma^*_{rad} + \Gamma_{nr} + \Gamma_q + \Gamma^*_{loss}$. We have added a supplementary term Γ^*_{loss} to account for non-radiative energy transfer to the metal, and we assume that the internal non-radiative decay rate Γ_{nr} and the methyl viologen quenching rate Γ_q are

independent of the presence of the DNH. The LDOS enhancement is then obtained as $(\Gamma^*_{rad} + \Gamma^*_{loss})/\Gamma_{rad}$, keeping only the rate influenced by the photonic environment, and taking into account non-radiative transfer to the metal. This expression of the LDOS enhancement corresponds to the quantity ζ used in Eq. (E.1).

We estimate the internal non-radiative rate $\Gamma_{nr} = 0.67$ ns^{-1} and the quenching rate $\Gamma_q = 1.75$ ns^{-1} using the knowledge of the 30% quantum yield of Alexa Fluor 647 in pure water solution which is quenched to 8% by 200 mM methyl viologen. We can now subtract these values of Γ_{nr} and Γ_q from the total decay rate Γ^*_{tot} with the DNH so as to estimate the part depending on the LDOS. For the DNH with perpendicular orientation, we get $\Gamma^*_{rad} + \Gamma^*_{loss} = 1.15$ ns^{-1} and a LDOS enhancement of 5.5× which is characteristic of nanoholes. For the parallel orientation, the apex further influences the decay rates so that $\Gamma^*_{rad} + \Gamma^*_{loss} = 5.9$ ns^{-1}. This corresponds to a LDOS enhancement of $5.9/0.21 = 28\times$, providing a clear demonstration of the DNH apex significant influence on the LDOS. Table E.2 summarizes the different rates, providing a complete overview of the fluorescence photokinetics alteration in the DNH. For the enhancement of the radiative rate Γ_{rad}, we use the value of η_{em} deduced from Fig. E.3b. The analysis of Tab. E.2 also reveals the increase of the non-radiative losses Γ_{loss} to the metal, which contribute to quench the fluorescence emission. Fortunately, this electromagnetic quenching is compensated by the simultaneous increase in radiative rate Γ_{rad} (Purcell effect), so that the effective quantum

	Γ_{rad}	Γ_{loss}	Γ_{nr}	Γ_q	Γ_{tot}	ϕ
Confocal	0.21	-	0.67	1.75	2.63	0.08
DNH perpendicular	0.84	0.31	0.67	1.75	3.57	0.24
DNH parallel	2.94	2.97	0.67	1.75	8.33	0.35

Table E.2: Fluorescence photokinetic rates inside DNH: Γ_{rad} radiative rate, Γ_{loss} non-radiative transitions to the metal, Γ_{nr} intramolecular non-radiative transitions, Γ_q methyl viologen quenching rate, Γ_{tot} total decay rate (inverse of fluorescence lifetime), ϕ quantum yield. All rates are expressed in ns^{-1}, the typical uncertainty is ± 0.05 ns^{-1}.

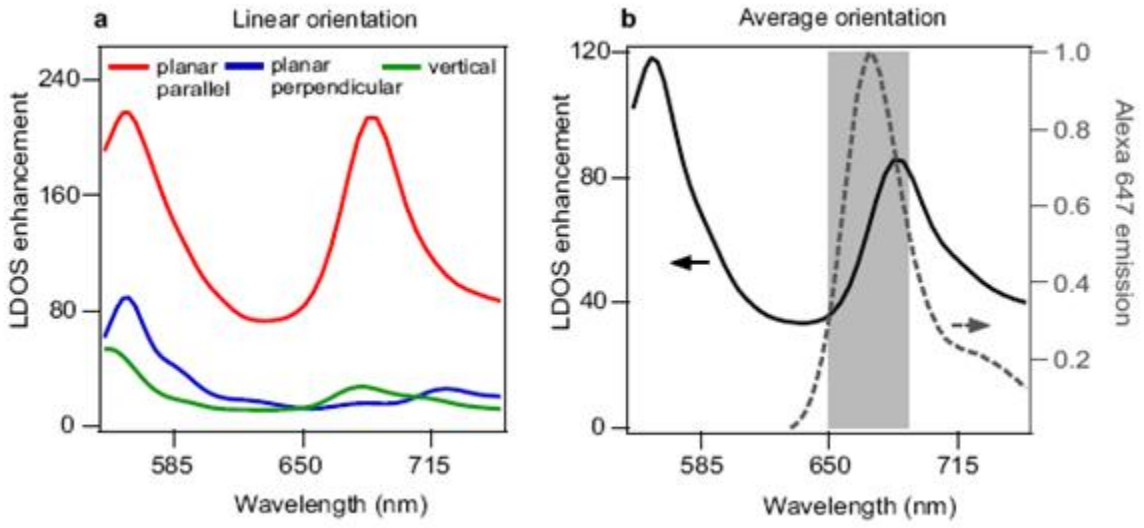

Figure E.5: Numerical simulations of LDOS enhancement for a dipolar emitter located in the center of the DNH gap. In (a), three different dipole orientations are displayed, the case when the dipole is oriented parallel to the apex provides the highest LDOS enhancement. In (b), the orientation-averaged LDOS enhancement is plotted as function of the emission wavelength (solid line). The normalized Alexa Fluor 647 emission spectrum is shown in dashed gray line, and the 650-690 nm region used experimentally for fluorescence collection is indicated.

yield ϕ of the dye is actually increased by the DNH presence.

To corroborate the experimental findings, we compute the LDOS enhancement as the relative increase in power released by a dipolar emitter located at the center between the DNH apex. Figure E.5a shows the LDOS enhancement for a dipole with different orientations. The case of orientation parallel to the DNH apex clearly stands out with a maximum LDOS enhancement up to 210x. Considering the orientation-averaged LDOS enhancement in the 650-690 nm region (Fig. E.5b), we obtain a mean 60x LDOS enhancement. This value is within a factor 2 of the experimental observation, which is satisfactory considering the 3D spatial averaging in the experiments, the limited temporal resolution of our apparatus, and some minor nanofabrication deficiencies. Moreover, the simulations show that the DNH design bears a resonance around 685 nm that covers well the Alexa Fluor 647 emission spectrum.

Conclusion

We provide a complete picture of the enhanced emission from nanoscale DNH volumes by analyzing the fluorescence temporal dynamics from pico- to milliseconds time scales. The clear polarization-dependent response allows to extract the relevant signal from the 25 nm gap area. We measure a nanometer detection volume of 74 zL, 7000-fold below the diffraction-limited confocal volume, and report fluorescence enhancement up to 100-fold, together with local density of optical states (LDOS) enhancement around 30-fold. As compared to state-of-the-art antenna-in-box design, the DNH has a comparatively lower detection volumes due to a better lateral and axial confinement. It is also significantly easier to fabricate using simple focused ion beam patterning. The DNH spectral resonance occurs in the range 550-700 nm, while it is in the near-infrared for the antenna-in-box. The DNH therefore enables a better spectral overlap with the emission band of most common red fluorescent dyes. While the antenna-in-box provides a higher gap intensity thanks to a nanoantenna disconnected from the metal film, the DNH partly compensates this feature by lower non-radiative losses and a better spectral overlap with the resonance. We also point out that much room remains for a thorough optimization of the DNH design parameters. Altogether, the distinctive features of double nanoholes combining high enhancement, efficient background screening and relative nanofabrication simplicity, open promising perspectives to study complex biochemical dynamics at physiological concentrations.

E.2.4 Methods

Double nanohole fabrication

The double nanohole structure is milled using focused ion beam (FEI Strata DB235) in a 100 nm thick gold film adhered to the glass substrate with 5 nm Ti adhesion layer. Prior to all experiments, the sample is cleaned by UV-ozone treatment for 10 minutes to remove organic impurities and render the gold surface hydrophilic. Experiments are performed immediately afterwards, with the sample being exposed to air for less than 2 minutes. After the FCS experiments, the sample is rinsed with ethanol, dried with nitrogen and cleaned again under UV illumination for 10 minutes. With this protocol, the sample can be reused several times without observing any change in optical performance (see the experiment series in Fig. 2).

Experimental setup

The fluorescence experiments are carried on a confocal inverted microscope (40×, 1.2 NA water-immersion objective) equipped with a three-axis piezoelectric stage for precise positioning of nanostructure within the laser focus. The excitation source is a linearly polarized He-Ne laser at 633 nm with 10 μW incident on the sample. Out-of-focus fluorescence is rejected by a 30 μm pinhole conjugated to the sample plane. Finally, the fluorescence is recorded using two avalanche photodiodes with 670±20 nm bandpass filters. Further for time-correlated counting measurements, the excitation source is switched to a picosecond pulsed laser diode operating at 636 nm (PicoQuant LDH-P-635, with 80 MHz repetition rate).

Fluorescence correlation spectroscopy method to quantify the apex volume and fluorescence enhancement

To quantify the hot spot detection volume and fluorescence enhancement, we analyze the fluorescence intensity temporal fluctuations $F(t)$ with a hardware correlator (Flex02-12D/C correlator.com, Bridgewater NJ, 12.5 ns minimum channel width) to perform fluorescence correlation spectroscopy (FCS). FCS computes the temporal correlation of the fluorescence signal $G(\tau) = \langle F(t).F(t+\tau)\rangle / \langle F(t)\rangle^2$, where τ is the delay (lag) time, and $\langle\,\rangle$ indicates time averaging.

In the DNH, the total fluorescence signal is the sum of the enhanced fluorescence from molecules within the apex region and the fluorescence from the molecules present in each nanohole. The FCS analysis discriminates between these contributions by considering the trace as a sum of two molecular species with different number of molecules and brightness: N^* molecules within the apex region with brightness Q^*, and N_0 background molecules with brightness Q_0 diffusing away from the region of interest (essentially inside the two nanoholes). An essential feature in FCS is that the molecules contribute to G in proportion to the square of their fluorescence brightness, so that the fluorescence from molecules in the apex region experiencing the maximum enhancement will have a major contribution in the FCS correlation. The temporal correlation of the fluorescence intensity F can be written as:

$$G(\tau) = \frac{\langle F(t).F(t+\tau)\rangle}{\langle F(t)\rangle^2} = 1 + \frac{N^* Q^{*2} G_d^*(\tau) + N_0 Q_0^2 G_{d0}(\tau)}{(N^* Q^* + N_0 Q_0)^2} \tag{E.2}$$

where $G_d^*(\tau)$ and $G_{d0}(\tau)$ are the normalized correlation functions for each species taken individually based on a classical three dimensional model:

$$G_{di}(\tau) = \frac{1}{(1+\tau/\tau_{d,i})\sqrt{1+s_i^2\,\tau/\tau_{d,i}}} \tag{E.3}$$

$\tau_{d,i}$ stands for the mean residence time (set by translational diffusion) and s_i is the ratio of transversal to axial dimensions of the analysis volume, whose value is set to $s = 0.2$ as it has negligible influence on the estimates of molecular concentration and brightness within the apex region (N^*, Q^*).

To extract the number of molecules within the apex region (N^*) and the corresponding fluorescence brightness Q^* (for a given sample concentration), we use the asymptotic value of the correlation function towards zero lag time:

$$G(0) = 1 + \frac{N_0 Q_0^2 + N^* Q^{*2}}{(N_0 Q_0 + N^* Q^*)^2} \tag{E.4}$$

The value of total fluorescence intensity F (i.e, $N_0 Q_0 + N^* Q^*$) is known from the experimental measurement, thus replacing $N^* Q^* = F - N_0 Q_0$ into Eq. (E.4), we obtain the fluorescence brightness and number of molecules within the apex region:

$$Q^* = \frac{F^2(G(0) - 1) - N_0 Q_0^2}{(F - N_0 Q_0)}, \quad N^* = \frac{(F - N_0 Q_0)^2}{F^2(G(0) - 1) - N_0 Q_0^2} \tag{E.5}$$

These expressions show that in addition to the experimentally measured parameters F and $G(0)$, we need to estimate the number of molecules and brightness (N_0, Q_0) for the molecules diffusing away from the apex region. At 20 μM concentration, we get $N_0 = 49$, and $Q_0 = 1.95$ kcounts/s from the results obtained from a control experiment with a double nanohole without any connecting gap region. These experimental findings are further validated from earlier work on single nanoaperture.

Numerical simulations

We performed two sets of finite-difference time-domain (FDTD) simulation (Lumerical 8.1). First, transmission through the DNH aperture was correlated with the experimental results. The SEM image of the structure was imported to the simula-

tion software environment. We used a total-field scattered-field source and the 3D simulation region was enclosed with perfectly-matched-layer boundaries with a 2 nm mesh override (1 nm mesh for the intensity maps in Fig. E.1b,c). The permittivity of gold was taken from Johnson and Christy and the refractive indices for the glass substrate and water were set to be 1.52 and 1.33. Second, the LDOS enhancement was calculated where dipole emitter located at the center between the cusps of the DNH was used to mimic the emission of the fluorescent molecule. The imaginary part of the Green's Function was evaluated along three axes, i.e. Imag(G_{xx}), Imag(G_{yy}), Imag(G_{zz}); and from that partial LDOS along the three axes were obtained and then averaged. The averaged LDOS was normalised to that of a homogeneous water medium.

Appendix F

Double nanohole optical trapping: dynamics and protein-antibody co-trapping

Originally published:

Zehtabi-Oskuie, H. Jiang, B. R. Cyr, D. W. Rennehan, A. A. Al Balushi, R. Gordon, Double nanohole optical trapping: dynamics and protein-antibody co-trapping, Lab Chip 13, 2563-2568 (2013).

F.1 Abstract

A double nanohole in a metal film can optically trap nanoparticles such as polystyrene/silica spheres, encapsulated quantum dots and up-converting nanoparticles. Here we study the dynamics of trapped particles, showing a skewed distribution and low roll-off

frequency that are indicative of Kramers-hopping at the nanoscale. Numerical simulations of trapped particles show a double-well potential normally found in Kramers-hopping systems, as well as providing quantitative agreement with the overall trapping potential. In addition, we demonstrate co-trapping of bovine serum albumin (BSA) with anti-BSA by sequential delivery in a microfluidic channel. This co-trapping opens up exciting possibilities for the study of protein interactions at the single particle level.

F.2 Introduction

Optical trapping using nanostructures has been of interest to trap nanoparticles for bio-analytical studies. In particular, aperture optical trapping allows for trapping at low powers, and easy detection of the trapping events by noting abrupt jumps in the transmission intensity of the trapping beam through the aperture. Improved trapping efficiency has been achieved by changing the aperture shape from a circle; for example, to a rectangle, double nanohole (DNH), or coaxial aperture. Of note, the rectangular aperture showed the dynamical trapping of 22 nm particles, showing a preference for dual-particle trapping. The DNH has the advantage of a well-defined trapping region between the two cusps where the nanoholes overlap, which typically allows only single particle trapping due to steric hindrance. The DNH has been used to trap and unfold a single protein. Recently, we studied the DNH integrated in a microfluidic chip with flow to show that stable trapping can be achieved under reasonable flow rates of a few mL min^{-1}. With such stable trapping under flow, it is possible to envision co-trapping of proteins to study their interactions.

Here we study the dynamics of single trapped nanoparticles in the DNH showing skewed distribution and low frequency roll-off. We interpret these results as coming

from Kramers hopping, which has been seen in dual-beam optical traps, but here it occurs at the scale of a few nanometers. We also study co-trapping. Co-trapping is achieved for the case where we flow in a protein (bovine serum albumin BSA) and co-trap its antibody (anti-BSA). Numerical simulations of the trapping potential agree well with our experimental results as well as showing a double well potential, as found in Kramers hopping systems. These experiments are significant steps towards future studies of nanoparticle interactions in the micro/nano-fluidic environment, where there is a natural convergence of plasmonic and fluidics for manipulation and sensing applications.

F.3 Microfluidic integration of double nanohole trap

F.3.1 Setup

Fig. F.1(a) shows a schematic of the DNH optical trapping system. The DNH is integrated in a system for microfluidic delivery that is compact enough to accommodate the high-NA transmission microscope geometry. Compared to past works, here we use a dual syringe pump system to allow for sequential delivery of a protein and its complementary antibody.

Fig. F.1(b) shows a scanning electron microscope image of the DNH as fabricated by focused ion beam milling in a 100 nm thick gold film with a 5 nm Ti adhesion layer (EMF Corp.). The separation between the cusps of the DNHs used in this work is 30 nm.

F.3.2 Trapping nanoparticles

We have reported in the past on trapping of polystyrene spheres, silica spheres (down to 12 nm), and single proteins. Fig. F.1(c) shows an example of trapping a quantum

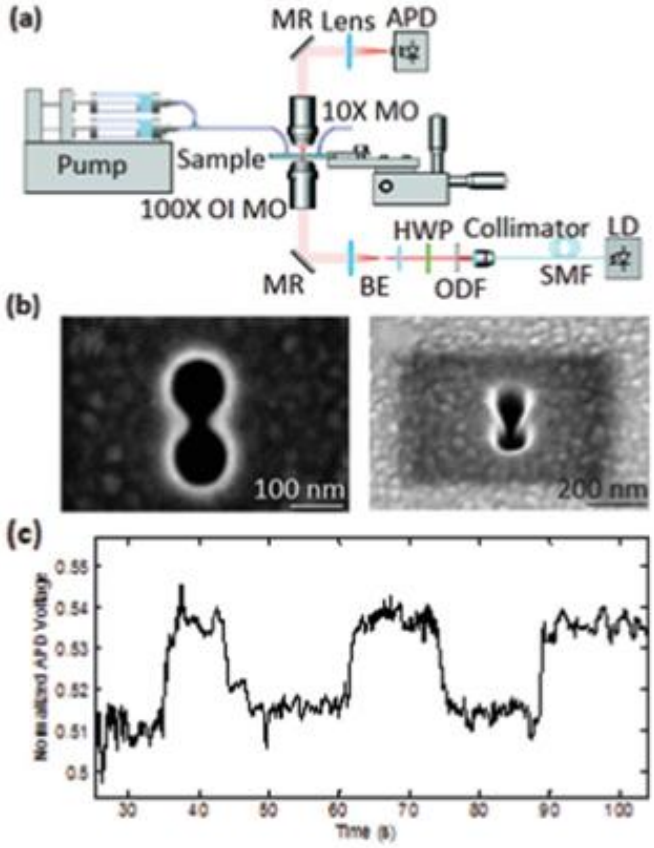

Figure F.1: (a) A Schematic of apparatus used to trap nanoparticles with dual microfluidic input. Abbreviations used: LD = laser diode; SMF = single-mode fiber; ODF = optical density filter; HWP = half-wave plate; BE = beam expander; MR = mirror; MO = microscope objective; OI MO = oil immersion objective; APD = avalanche photodetector. (b) A scanning electron microscope image of the double nanohole. (c) Optical trapping of quantum dots seen as sudden discrete jumps in APD signal.

dot (Q21031MP, Life Technologies), where the trapping events appear as discrete steps of the same size. A SavitzkyGolay algorithm for noise reduction is used here and in subsequent time series figures, but not in the power spectra analyses. This quantum dot, used for in vivo imaging, is not targeted but it does contain surface functionalization to prevent non-specific binding. The overall diameter of the quantum dot is 1020 nm, as specified by the manufacturer. The ability to trap quantum dots, and similar nanoparticles, is interesting from the point of view of translating

the nanoparticle to a different location; for example, introducing a light emitter into a photonic crystal or an optical antenna. It is also of interest to study isolated nanoparticles within a heterogeneous mixture.

In particular, we are interested in studying the fluorescence of trapped nanoparticles within the trap, but have not yet achieved this goal. For the quantum dot samples, further modifications of the setup are required to add an excitation source and appropriate filters to excite and detect the fluorescence. Recently, however, we trapped up-converting nanoparticles of 18 nm in diameter (not shown) using a 980 nm laser. This configuration is interesting because the trapping laser can simultaneously be used as the pump source, due to the up-conversion process. We were able to observe the fluorescence of the up-converting nanoparticles in solution; however, we have not yet been able to observe a fluorescence spectrum from the nanoparticle while it is trapped. We suspect that this may be due to plasmonic quenching of the nanoparticles, which is particularly detrimental to studies of up-converting nanoparticles because of their long lifetimes. This quenching may be an issue for nanoaperture optical trapping in general, and we aim to investigate the effect further in the future; however, this will require a separate study beyond the scope of this work.

F.4 Dynamics of the double nanohole trap

F.4.1 Roll-off frequency

Fig. F.2(a) shows the time domain response for a 20 nm polystyrene particle trapped using a DNH. It is clear that the noise increases substantially when the particle is trapped. This noise corresponds to the thermally driven motion of the nanoparticle in the trap, and so it contains information about the position of the particle in the trap.

Fig. F.2(b) shows the power spectrum of this noise. As is common with trapping systems in the low-Reynolds number regime, we fitted this response to a Lorentzian and found a roll-off frequency of 11 Hz. We repeated this analysis 18 trapping events using laser powers between 10 and 15 mW, with an average roll-off frequency of 10 $\pm$ 3 Hz, where the uncertainty is taken from the standard deviation. The roll-off frequency increased from 8 Hz at 10 mW to 12.5 Hz at 15 mW. Considering the small size of the particle and using the usual statistical analysis, this is an unusually low roll-off frequency, by about 4 orders of magnitude, as will be discussed further below.

F.4.2 Skewness distribution

Fig. F.2(c) shows a histogram of the avalanche photodetector (APD) voltage for the trapping event in Fig. F.2(a). Histograms are commonly used in the trapping literature to monitor the position of a particle and also deduce the trapping potential. For the aperture traps, the transmission intensity can be used to study the trap dynamics. Unlike previous works, however, the trapping events analysed here showed a clearly negative skewness of -0.4 $\pm$ 0.2 V over all the 18 events analysed.

F.5 Cotrapping of protein-antibody

Fig. F.3 shows a schematic of the protein/antibody trapping co-trapping experiments, where a,b,c,d,e,f show flowing in of ultra-pure BSA (AM2616, Life Technologies), trapping of BSA, flowing in polyclonal anti-BSA (A11133, Life Technologies), trapping of anti-BSA, flowing in of anti-BSA while BSA is trapped, and co-trapping of BSA with anti-BSA. Previously, we have reported on the trapping and unfolding of BSA, so those results are not repeated here. As with our previous work on trapping a protein, a thiolated PEG layer was attached to the gold film to help prevent adhesion of the

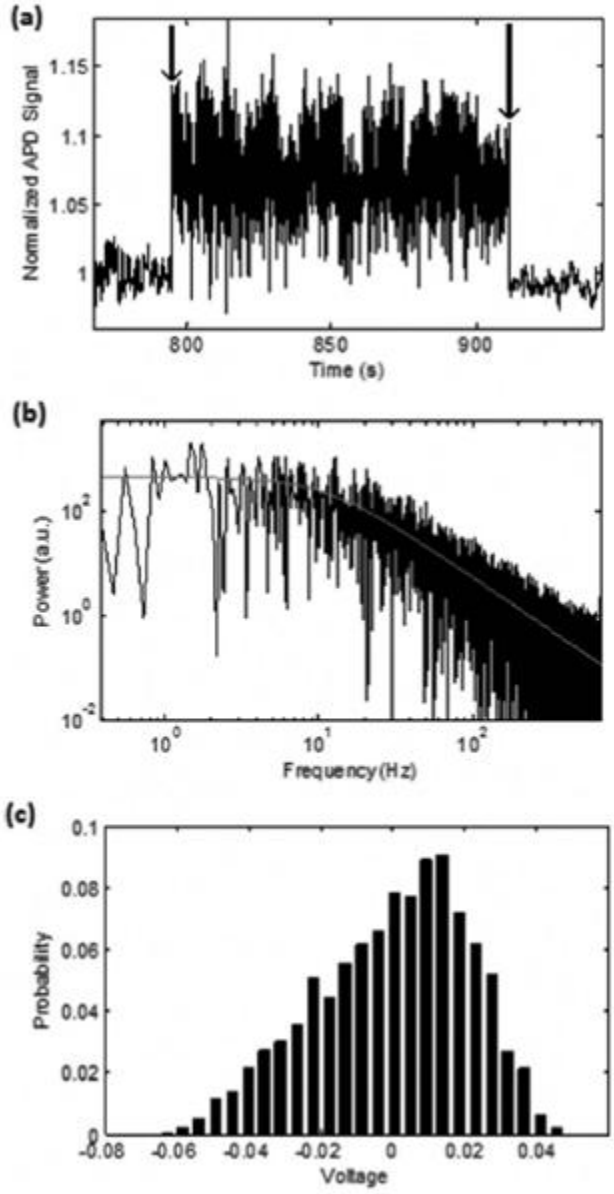

Figure F.2: (a) Time domain trapping event of a 20 nm diameter polystyrene sphere. Trapping and releasing are discrete steps shown with arrows. (b) Power spectrum of the trapping event in (a). The 3-dB roll-off occurs at a frequency of 11 Hz. (c) Voltage distribution from the trapping event in (a). The plot is offset so that mean is around zero. The skewness is 20.41, which is close to the average found over 18 trapping events.

proteins. The concentrations used were 0.1% w/v for the BSA in phosphate buffered saline solution 0.01% w/v for the anti-BSA in phosphate buffered saline solution.

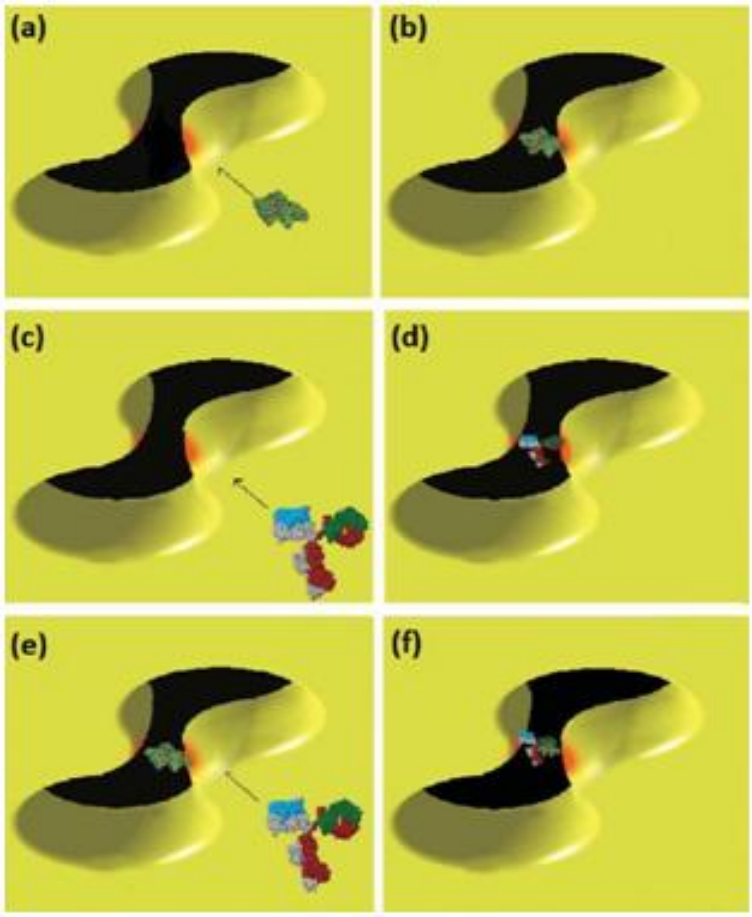

Figure F.3: (a) The approach of a single BSA particle to the double nanohole is shown. (b) A single BSA particle is trapped between the tips of the double nanohole. (c) An anti-BSA particle is shown approaching the vacant trap. (d) An anti-BSA particle is trapped between the tips of the double nanohole. (e) An anti-BSA particle is introduced into a system with a BSA particle already trapped. (f) Both an anti-BSA and a BSA particle are co-trapped between the cusps of the double nanohole.

Fig. F.4 shows the trapping of anti-BSA as seen by a jump in the transmission through the aperture measured with an APD. While the step-size depends on the aperture used, it was found that the step-size for trapping anti-BSA alone was typically ~ 2 times larger than BSA alone in these experiments, which is reasonable since anti-BSA is three times larger than BSA. Note that there is not a direct correlation

between the particle size and the trapping signal because of the different shapes of the BSA and anti-BSA particles; however, the expected trend is that larger particles will show a larger signal. Fig. 5 shows the trapping and subsequent co-trapping of BSA and anti-BSA, where the anti-BSA is flowed into the micro-channel once trapping of BSA is achieved. We found empirically that the BSA was not released from the trap when a moderate flow rate of 5 ml min^{-1} was used. We have investigated in detail the relation between flow rate and trapping for 20 nm polystyrene particles previously and the chosen flow rate is consistent with that experiment; however, we have not carried out such an extensive investigation for BSA or anti-BSA. Two repeated measurements are shown in the supplemental information, including one where anti-BSA is trapped first, and BSA is subsequently co-trapped.

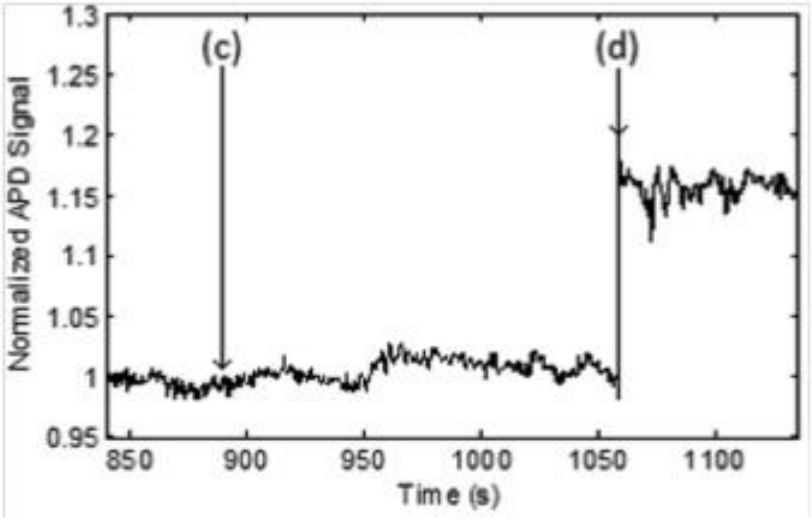

Figure F.4: Typical trapping signal of an anti-BSA particle is shown. The letters (c) and (d) refer to schematic Fig. F3.

F.6 Numerical simulations of DNH optical trap

We performed comprehensive finite-difference time-domain electromagnetic calculations of the DNH structure combined with Maxwell stress tensor analysis to give a

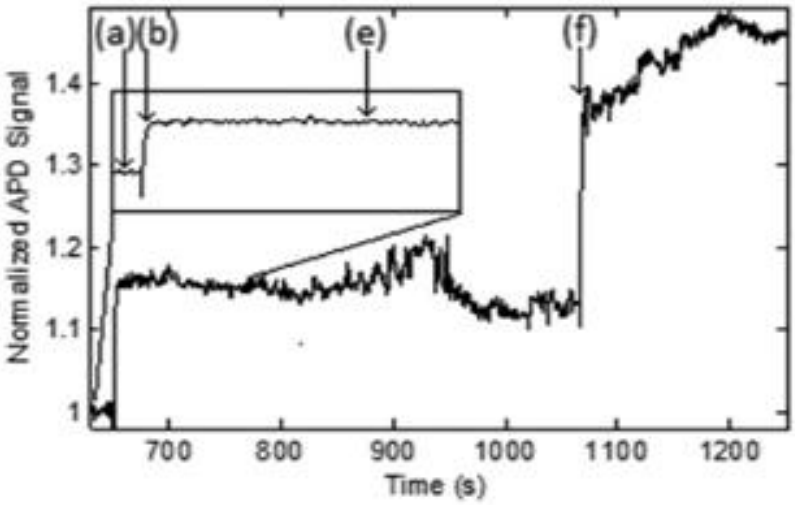

Figure F.5: Co-trapping of BSA with anti-BSA. After flowing in BSA (a), BSA trapping occurs (b), followed by flowing in anti-BSA (e), and anti-BSA co-trapping (f). The letters (a), (b), (e) and (f) refer to schematic Fig. F3.

better physical understanding of the trapping behaviour. The approach is similar to our past work,9 except here we consider the DNH shown schematically in Fig. F.4. The grid size was chosen to be 1 nm to accurately account for the electromagnetic near-field, the centre wavelength was chosen to be 815 nm, the refractive index values for the polystyrene, glass substrate and water were chosen to be 1.575, 1.52 and 1.33, and the permittivity of the gold was chosen to be 215.2 + 1.5i. We found that the Ti layer has negligible effect and so it was ignored in these simulations. The gap-size at the overlapping point of the DNH was taken to be 30 nm and the particle size was taken to be 20 nm. The source was chosen to be a Gaussian with a spot-size of 500 nm. The laser power was taken to be 10 mW.

Fig. F.6(a,b) shows the electric field intensity distribution without and with the nanoparticle on a dB-scale. It is clear that the presence of the nanoparticle creates a strong and non-uniform redistribution of the local field that cannot alone be accounted for by a simple dipolar model. Fig. F.6(c) shows the trapping potential energy when moving the particle between the two cusps. There is a potential barrier of 0.18 kT in

the trapping potential between the two trapping potential minima (leaving a 1 nm gap on each side to facilitate Maxwell stress tensor analysis), where k is the Boltzmann constant and T is the temperature (assumed to be 300 K). The range of motion for the particle is restricted by the hard boundaries of the DNH aperture. The total depth of the trapping potential at this power was found to be 6.52 kT.

In our past experiment, we found that a trapped particle was released when the power was reduced to 2 mW. It is reasonable then that 2 mW corresponds to a potential well depth of approximately kT; that is, around the transition between having a free particle and stable trapping for a measurable time. Therefore, there is reasonable agreement with our simulations that give a potential well depth of 6.52 kT for 10 mW of power, where approximately 5 kT is expected from linear scaling.

F.7 Discussion

F.7.1 Kramers hopping explanation of low frequency roll-off

While the DNH clearly does not have a harmonic potential, we consider the analysis associated with a harmonic potential as a starting point to get an order-of-magnitude estimate of the expected roll-off frequency. The roll-off frequency is given by: $f_0 = \alpha/(2\pi\beta)$, where α is the trap stiffness and is the drag coefficient. We can estimate the trapping stiffness from the equipartition principle $\alpha < x^2 > = \text{kT}$, using, $< x^2 > =$ 100 nm^2 by assuming that the trapping dimension is comparable to lateral dimension of the aperture and/or the particle size. For the Stokes drag on a sphere of 20 nm diameter in water, we find $f_0 = 310^4$ Hz. Even if the Stokes drag is made three times larger due to Faxens law at the boundary, this is still significantly larger than ~ 10 Hz observed in the experiments. A possible explanation for the low frequency noise roll-off in the power spectrum is Kramers hopping. Kramers hopping has been observed

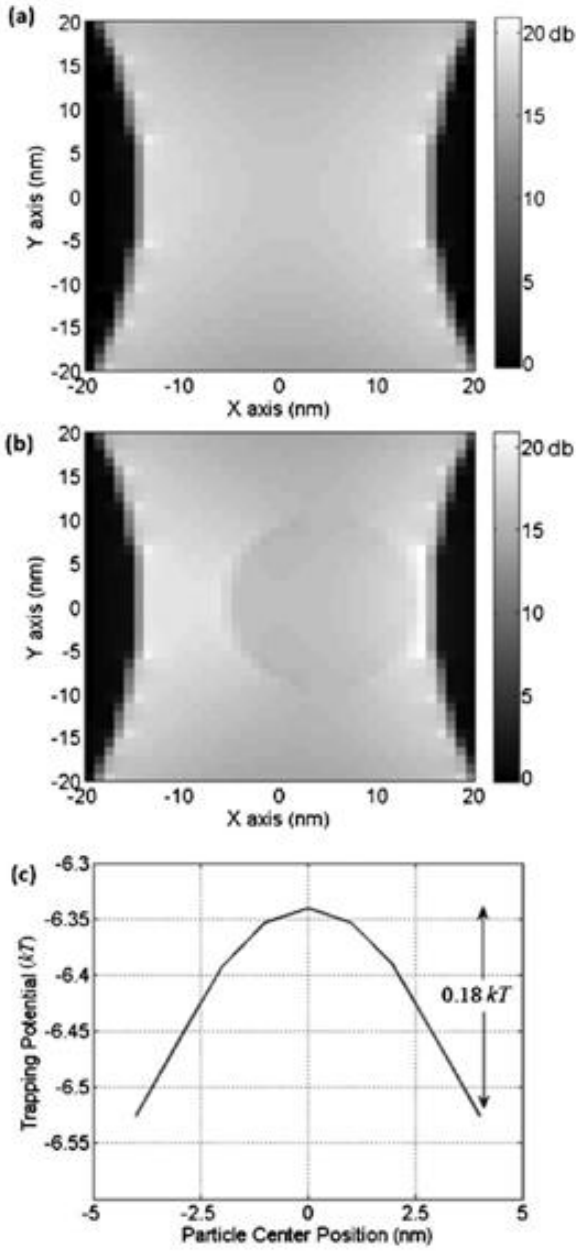

Figure F.6: FDTD simulation results of the double nanohole trap. The electric field intensity enhancement profile (dB-scale) of the double nanohole (a) without nanoparticle and (b) with nanoparticle. (c) The calculated trapping potential across the two cusps of the double nanohole showing two stable minima for 10 mW input power.

in double-well optical traps separated by 350 nm and having a barrier height from a fraction of kT up to several kT, resulting in three decade variation in the transition rates between the two potential wells. That work considered 600 nm diameter silica spheres. For the DNH, there are also two stable trapping points at the two cusps. The dimensions are reduced by approximately a factor of 30, however, to 10 nm separation between the stable points and a 20 nm diameter polystyrene sphere.

The skewed position distribution also supports the Kramers hopping hypothesis. In particular, the extended tail towards lower intensity can be interpreted as the time spent transitioning over the barrier between the two stable points. While there are few examples of aperture trapping in the literature, recent works on rectangular apertures did not appear to show a skewed distribution. In that work, the separation between the stable trapping points at each edge of the trap was significantly greater than the particle size. That work did find trap-release-trap events with a 71% probability, where it is possible that the second trapping event occurs at the other side of the rectangle.

It is difficult to quantitatively estimate the transition rate due to surface hydrodynamics and the complicated 3D geometry of the system. It should be noted though that thermal effects are expected to be small since BSA does not denature in the trap, and its denaturing temperature is around 50 °C. The good thermal conductivity of the gold film helps reduce heating effects in aperture trapping, as compared to isolated resonant structures, like in plasmonic particle trapping and photonic-crystal trapping. Indeed, recent works on plasmonic nanopillars have used an adjacent metal film as a natural heat sink. It is possible to imagine future experiments to explore stochastic resonance effects by dithering the position of the trapping beam at a rate comparable to the Kramers hopping frequency; however, we have not attempted these so far.

F.7.2 Co-trapping towards protein-protein interaction

Our motivation for studying co-trapping has been to investigate protein-protein interactions at the single/few particle level. First, we note that others have reported co-trapping of nanospheres in rectangular aperture traps, and indeed it is the preferred state in that configuration where the width of the rectangle is comparable to twice the diameter of the nano-spheres. For the DNH trap, however, the situation is very different. We have found that steric hindrance prevents larger particles from being trapped in a gap that is narrower than the particle itself. It stands to reason that for a 30 nm gap then, the co-trapping of two 20 nm particles is also subject to steric hindrance, and indeed we have not observed such co-trapping behaviour for the samples investigated in this work or in past works. Furthermore, we have not observed co-trapping for BSA with BSA, or for anti-BSA with anti-BSA, as studied in this work. Again, we suspect that this is because of steric hindrance. Therefore, it is interesting that we have observed co-trapping events for BSA with anti-BSA. This strongly suggests that there is binding occurring between the BSA and anti-BSA. This is consistent with the fact that anti-BSA has a naturally high binding affinity for BSA. We plan to attempt further studies to show definitively that the binding occurs for the case of co-trapping. Should this prove to be the case, then the DNH trap would make an excellent test-bed for studying protein binding at the single particle level. It is noted in Fig. F.5 that there is a bump in the APD voltage around 900 s prior to stable co-trapping. Due to the timing of this event (i.e., when the antibody solution enters into the trapping region), we believe that this may be the result of an unsuccessful co-trapping event, where the antibody flows away before it can be stably co-trapped.

F.8 Conclusions

In conclusion, using the DNH optical trap, we have studied trapping, trapping dynamics and co-trapping of different nanoparticles, ranging from quantum dots to proteins. The power spectrum of optical trapping for the DNH showed a surprisingly low frequency roll-off of ∼10 Hz. We believe that Kramers hopping between the two stable points of the DNH trap leads to this observed roll-off, which is further supported by negative skewness in the intensity distribution and numerical simulations of the trapping potential. This nanos-cale version of Kramers hopping is an interesting system to explore other phenomena, such as stochastic resonance, and we believe that this would be achievable within our current setup by oscillating the trapping beam position.

Of particular interest to lab-on-chip studies of protein systems, here we demonstrated co-trapping of a protein with its antibody. Such co-trapping was not found for other particles that do not have a strong binding affinity, which suggests that the protein-antibody system was jointly bound in the trap. These findings are interesting to further studies of trapped nanoparticles, particularly protein-protein interactions at the single particle level.